ESTIMATION OF A CORONARY VESSEL WALL DEFORMATION WITH HIGH-FREQUENCY ULTRASOUND ELASTOGRAPHY

A Thesis
Presented to
The Academic Faculty

by

Ismail H. Kasimoglu

In Partial Fulfillment
of the Requirements for the Degree
Doctor of Philosophy in the
School of Electrical and Computer Engineering

Georgia Institute of Technology
December 2007

ESTIMATION OF A CORONARY VESSEL WALL DEFORMATION WITH HIGH-FREQUENCY ULTRASOUND ELASTOGRAPHY

Approved by:

Professor Paul J. Benkeser, Advisor
School of Electrical and Computer Engineering & Department of Biomedical Engineering
Georgia Institute of Technology

Professor Arthur Koblasz
School of Electrical and Computer Engineering
Georgia Institute of Technology

Professor Anthony J. Yezzi
School of Electrical and Computer Engineering
Georgia Institute of Technology

Professor Brani Vidakovic
Department of Biomedical Engineering & School of Industrial and Systems Engineering
Georgia Institute of Technology

Professor Oskar Skrinjar
School of Electrical and Computer Engineering & Department of Biomedical Engineering
Georgia Institute of Technology

Date Approved: 6 November 2007

To my beautiful angel,

Ipek.

ACKNOWLEDGEMENTS

I would like to express my gratitude to all those who gave me the possibility to complete this thesis. It will be tough to thank them enough, but I will nonetheless try.

First of all, I would like to thank my advisor, Dr. Paul J. Benkeser for his continuing support and guidance throughout my study. I also want to extend my appreciation for his patience, great understanding and very nice personality.

I am deeply indebted to Dr. Anthony J. Yezzi for his guidance since the beginning of my research. Having taken his PDE class was a cornerstone of my doctoral study, where I learnt about active contours. This thesis would not have been possible without his direction and help.

I also wish to express my sincere thanks to Dr. Oskar Skrinjar for his detailed and constructive comments throughout this work. His Medical Image Processing course was one of the best courses I had ever taken in my life, which also helped me improve my programming skills in MATLAB a lot.

I would like to cordially thank Dr. Arthur Koblasz, Dr. Brani Vidakovic, Dr. Oskar Skrinjar and Dr. Anthony J. Yezzi for being on my dissertation defense committee, and thank Dr. Jennifer E. Michaels for being on my proposal committee.

I also thank Dr. Raymond Vito and his students for allowing me to use their lab tools. My warm thanks also extend to my former lab mate Veerdhaval V. Mahajan for his invaluable efforts in designing our experimental setup and his tutoring me on how to take coronary arteries out of the heart. I also thank Mr. Hollifield and Hollifield Farms for letting me use the porcine hearts, an integral part of my research.

I cannot finish without saying how grateful I am with my family. I sincerely thank my parents, Serpil and Levent Kasimoglu, and my brother, Talat, for their love, encouragement and support, and my grandparents for their blessings. My parents have always put education as a first priority in my life, and raised me to set high goals for myself. They have supported and encouraged me to do my best in all matters of life all the time, and have always been there for me as an unfaltering support.

Finally, I've come to address my appreciation to my wife, Ipek Z. Kasimoglu, who has been my "other half" for more than ten years since high school. During this period, of course we had some difficult times, but we always managed to get them over. Although we were physically far away from each other for most of my Ph.D. study, I felt that she was always near me whenever I needed her. Without her love and support, I couldn't have made it. Once again, I would like to thank her for all of her sacrifices, encouragement, support, friendship and love. This thesis is as much hers, as it is mine.

As for my last words, I would like to thank My God for making this happen.

TABLE OF CONTENTS

LIST OF TABLES

LIST OF FIGURES

SUMMARY

Elastography, which is based on applying pressure and estimating the resulting deformation, involves the forward problem to obtain the strain distributions and the inverse problem to construct the elastic distributions consistent with obtained strains on observation points. The proposed research focuses on the former problem whose solution is used as an input to the latter problem. The aim of this thesis is then to provide the inverse problem community with accurate strain estimates of a coronary artery vessel wall. In doing so, a new ultrasonic image-based elastography approach is developed. Because the accuracy and quality of the estimated strain fields, first of all, depends on the resolution level of the ultrasound image and to date best resolution levels obtained in the literature are not enough to clearly see all boundaries of the artery, one of the main objectives is to acquire high-resolution coronary vessel wall ultrasound images at different pressures. For this purpose, first an experimental setup is designed to collect radio frequency (RF) signals, and then image formation algorithm is developed to obtain ultrasound images from the collected signals. To segment the noisy ultrasound images formed, a geodesic active contour-based segmentation algorithm with a novel stopping function that includes local phase of the image is developed. Then, a region-based information is added to make the segmentation more robust to noise. Finally, elliptical deformable template is applied so that a priori information regarding the shape of the arteries could be taken into account, resulting in more stable and accurate results. The use of this template also implicitly provides boundary point correspondences from which high-resolution, size-independent, non-rigid and local strain fields of the coronary vessel wall are obtained.

CHAPTER I

INTRODUCTION

1.1 Research Objectives

Ultrasound, primarily due to being inexpensive, portable and safe, has been one of the leading medical diagnostic imaging modalities since the late 1940s. Despite today's sophisticated high-tech systems, ultrasound remains a science built upon the simple sound wave without the use of ionizing radiation. Acoustic waves with a frequency above 20 kHz are launched, using a transducer, into the medium where a portion of them is reflected from the interfaces/boundaries between tissues with different acoustic properties. From those reflected waves (i.e., echoes), an image that provides information about the location and strength of the boundaries within the medium is formed. This ultrasound image, however, lacks information related to tissue morphology and architecture. Therefore, a new imaging technique called *elastography* that displays the mechanical properties of tissues, such as strain and elastic modulus (i.e., stiffness), has been developed. In applying pressure and estimating the resulting deformation, elastography quantifies one of the oldest methods of medical diagnosis, that is, palpation, which is based on the qualitative assessment of the stiffness of tissues.

The complete tissue elasticity imaging involves the forward problem to obtain the strain distributions and the inverse problem to construct the elastic distributions consistent with obtained strains on observation points. The proposed research focuses on the former problem whose solution is used as an input to the latter problem. Actually, the inverse problem is an ill-posed non-linear problem whose solution does not necessarily satisfy conditions of existence, uniqueness and stability [87]. It requires the

computation of the local stress that depends upon the geometry and structure of the tissue and cannot be directly measured from within the soft tissue. In the literature, this difficult inverse problem is generally being solved using regularization methods [39], non-linear optimization techniques [36] and/or iterative parameter reconstruction algorithms utilizing finite element model (FEM) [31, 5, 6]. At this point, however, it should not be disregarded that the accuracy and quality of the reconstructed elasticity distributions, first of all, depend on the solution of the forward problem, i.e., the estimated deformation fields, because nothing but those deformation estimates are the inputs to the inverse problem. Given the significance of the forward problem, the aim of this thesis is then to provide the inverse problem community with accurate strain estimates of the coronary artery vessel wall[1].

The layers of the coronary artery vessel wall, namely, *intima*, *media* and *adventitia* (from inside to outside) may respond differently to alterations in internal pressure. So, for the same pressure changes the strain patterns of intima, media and adventitia may not be identical due to either stress decay or different elastic properties of each layer or both. Also, diseases such as atherosclerosis where fatty and/or fibrous deposits (i.e., plaques) accumulate within the vessel wall are expected to have an impact on the strain distributions within the wall since the mechanical properties of the plaque are not the same as those of the vessel wall (e.g., generally fibrous plaques are stiffer and fatty plaques are softer than the layers of the vessel wall). From all above, it is apparent that estimation of strain fields within the coronary artery vessel wall is a first but very crucial step in determining the mechanical properties and composition of the artery.

The accuracy and quality of the estimated strain fields, first of all, depends on how much detail is present in the ultrasound images. Specifically, the better the

[1]Coronary arteries are located between the epicardial and myocardial layers of the heart, often embedded in fat. Their role is to supply oxygenated blood to the heart.

resolution is, the more precise deformation estimation can be done. Hence, one of the main goals of this research is *to acquire high-resolution coronary artery ultrasound images at different intraluminal pressures*. There is, however, also a need *to develop a technique for the comparison of those ultrasound images* so that *the deformation of the coronary vessel wall can be estimated accurately*. Since the heterogeneous nature of the vascular tissue and of the plaque induce complex tissue deformations that may not be uniform throughout the wall, the developed technique needs to help estimate *non-rigid and local deformation fields* within the coronary artery vessel wall. Also, to remove the restrictions related to the size of the deformations the estimated deformation fields need to be *size-independent* (i.e., valid for both small and large deformations).

In comparing ultrasound images to estimate the deformation fields within the vessel wall, the use of *image segmentation* is beneficial, because deformation estimation based on tracking inner and outer boundaries of intima, media and adventitia would be much more reliable while providing fairly sufficient information about the characteristics of the vessel wall. Basically, there are five circular/elliptical boundaries, namely, inner & outer intima, inner & outer adventitia and fat from inside to outside within the coronary artery vessel wall. The segmentation algorithm to be developed needs to be tailored to this special architecture of a coronary vessel wall. Also, another challenge is the low signal-to-noise ratio (SNR) of high-resolution ultrasound images. Therefore, the segmentation algorithm to be developed also needs to be robust (i.e., noise-insensitive). Finally, the segmentation process should also provide boundary point correspondences (among the corresponding boundaries at different pressures), which are required to know to be able to obtain high-resolution, size-independent, non-rigid and local strain fields within the coronary artery vessel wall.

As a result, the main objectives of this thesis are to obtain the "best" resolution levels ever for the coronary artery vessel wall, to explore the associated challenges and

develop an approach to deal with them, and finally to provide the inverse problem community with high-resolution, size-independent, non-rigid and local strain fields within the coronary artery vessel wall.

1.2 Organization of the Thesis

The thesis is organized as follows:

In Chapter 2, the previous work pertinent to this thesis is examined. First, a brief overview of the ultrasound elastography literature is presented. Three main groups of techniques, namely, coherent, incoherent and image-based are discussed in depth. Their advantages and disadvantages relative to each other are detailed. Second, existing studies that have used high-frequency ultrasound imaging are stated. The importance of using high-frequency ultrasonic system in getting high-resolution images is emphasized. Third, some research efforts on image segmentation are explained. In particular, the technique of active contours, which is based upon the utilization of deformable contours that conform to various object shapes and motions, is outlined. Some active contour models that have been developed particularly to segment the intravascular ultrasound images are discussed. On the other hand, the problems associated with classical active contour models are also detailed along with a geodesic active contour model developed to solve those problems.

In Chapter 3, the experimental setup designed for radio frequency (RF) data acquisition is described. Capturing high-frequency ultrasonic signals backscattered from a tissue is still mostly performed by using single element transducers. To be able to scan a 2-D cross-section of a tissue while using a single element high-frequency transducer, there is a need for a custom-made experimental system. The characteristics of the designed system including the facilities and equipments used are detailed here. Then, the way data acquisition has been performed to collect RF signals from a 2-D cross-section of the artery vessel wall is outlined. Finally, how to form ultrasound

images using the collected RF signals is explored.

In Chapter 4, a segmentation algorithm to formally detect all five boundaries of the formed ultrasound images, namely, lumen-intima (i.e., inner intima), intima-media (i.e., outer intima), media-adventitia (i.e., inner adventitia), adventitia-fat (i.e., outer adventitia) and outer fat, is developed step-by-step. The main challenge regarding the segmentation of the ultrasound images is the inherent noise present in the high-resolution ultrasound images formed. To deal with that high amount of noise, there is a need to develop robust segmentation algorithm. For this purpose, in this chapter first a new stopping function that includes not only image gradient but also local phase of the image is developed and incorporated into the edge-based geodesic active contour model. Then, to further increase the robustness of the algorithm region-based information is also added. Finally, to improve the stability of the developed segmentation algorithm a novel elliptical deformable template is applied. In doing so, the previous two steps, that is, edge-based and region-based segmentation approaches are used along with an elliptical shape constraint. The main motivation here is to incorporate into the model a priori information regarding the shape of the coronary vessel wall. Basically, the evolving contours are first restricted to be an ellipse, and the aim is to optimize the ellipse parameters so that the contours fit image edges as closely as possible. Then, in the refinement step that follows the shape constraint of being an ellipse is relaxed to make the contours even better fit the edges. The beauty of this developed segmentation algorithm is that it implicitly provides boundary point correspondences between images obtained at different pressures.

In Chapter 5, how to estimate strain fields within the vessel wall by using the matched points between boundaries is discussed. In particular, the radial strain map corresponding to the case where intraluminal pressure is increased from 30 to 60 mmHg is shown. The characteristics of the estimated deformation field, namely, being size-independent, local, non-rigid and high-resolution, are discussed.

Finally, Chapter 6 concludes the thesis by summarizing its contributions as well as the future work.

CHAPTER II

BACKGROUND

2.1 Elastography

For more than a decade, elastography, introduced by Ophir et al. [63], has received a lot of attention for its ability to estimate and image soft tissue strain profiles. In conventional elastographic imaging, the tissue under inspection is externally compressed with a small quasistatic force, and then pre- and post-compression digitized radiofrequency (RF) echo signals are acquired using an ultrasound (US) equipment. Congruent echo lines are subdivided into partially overlapped small temporal windows that are compared pairwise using cross-correlation techniques. For each window, the local tissue displacement is computed as the location of the maximum of the cross-correlation function. The local strain is then determined by applying the finite difference to the displacement estimates of the adjacent windows [75, 62, 64]. De Korte et al. incorporated this time-domain cross-correlation technique in intravascular applications using vessel-mimicking phantoms [26] as well as human femoral and coronary arteries [27, 30, 29, 79]. This technique, however, is only accurate for strain values smaller than 2% and fails rapidly with increasing strains, because it ignores the signal shape variation induced by the physical compression of the medium. To enhance the correlation between pre- and post-compression signals under large deformations, global stretching of the compressed temporal signal was employed in [1]. However, this method assumes a constant strain magnitude over the signal, which may not be true due to the heterogenous nature of tissues. For this reason, techniques that adaptively estimate a localized stretch factor have also been developed. In [2], the signal after compression was considered as a locally delayed and scaled replica of

the signal before deformation. To estimate the strain value for each window segment, an iterative algorithm that adaptively maximizes the correlation between pre- and post-compression signals by appropriately stretching the latter was used. In [12], the local scaling factor for each window segment was estimated by iterative variation until reaching zero mean phase difference between the complex pre- and post-compression signals. In both studies, strain values up to 7% could be estimated accurately. Moreover, in [84] was shown that the use of a local adaptive stretching approach improves the elastographic contrast-to-noise ratio (CNR). However, due to the iterative procedure one of the limitations of this adaptive stretching method is the computational complexity. Another difficulty arises in choosing the proper correlation window size. Small windows result in better resolutions while reducing SNR. On the other hand, large window means that there will be significant variations in the strain within the window, degrading the performance of the method since it assumes constant strain within each window. Finally, in these techniques (i.e., the classical elastography technique and its variants) tissue deformation can be accurately estimated only in the radial direction (i.e., parallel to the ultrasound beam direction), because circumferential (i.e., perpendicular to the ultrasound beam direction) decorrelation introduces errors in estimating strain patterns in the circumferential direction (especially for large strain values).

In addition to the time-domain cross-correlation techniques mentioned above, another coherent estimation technique, namely, correlation-based phase-sensitive speckle tracking, has also been developed in the literature. This technique estimates the rectangular region in the target image that best matches a corresponding region in the initial image (i.e., kernel region), where both images are complex baseband images. For the correlation processing, linear phase evolution property of ultrasonic propagation (i.e., the region containing a scatterer has a constant phase proportional to the time delay of the received echo) is exploited [22, 23]. On the other hand, there are

some limitations to this technique as well. First, the performance of the correlation search is highly dependent on the size of the kernel and the search region. For the small kernel region, the speckle characteristics will not be adequately captured, while for the large one the deformation between two images will cause decorrelation. Also, the search region must be large to find the correct region; however, excessive computations will result if the search region is too large [61]. Second, this technique breaks down for large strain values due to the change in speckle character. To avoid the latter problem, in [83], cross-correlation was calculated in several intermediate steps of intraluminal pressure. Then, displacement values estimated by correlation-based phase-sensitive speckle tracking were accumulated over a series of pressures to get the total displacement values whose spatial derivatives give the strain values (up to 4%). In [19], an integrated compliant silicone balloon catheter was developed to allow much greater deformations using the same phase-sensitive correlation technique. The drawback of both [83] and [19] is that calculating cross-correlation in several intermediate steps is a time-consuming process. Another drawback, which is valid for all correlation-based phase-sensitive techniques stated above, is that only radial strain values can be measured accurately (as in time-domain cross-correlation techniques), because they can be directly calculated using the phase of the ultrasound signal. However, phase knowledge cannot be exploited in the circumferential direction, causing the estimation of the circumferential strain patterns to be unreliable.

Although coherent estimation techniques (i.e., time-domain cross-correlation and correlation-based phase sensitive speckle tracking) generally have the advantage of being highly precise, they are not very robust in the presence of even a moderate amount of decorrelation between the pre-compression and post-compression signals[1]. Therefore, alternatively to the coherent estimation techniques that require the use of

[1] As stated in the text, some coherent techniques have tried to solve this problem by compromising the computational complexity and length of the whole estimation process.

phase information to estimate tissue deformation, a number of incoherent estimators where the phase information within RF signals is not used have also been developed in the literature. For example, in [44], strain was directly estimated from the relative frequency shift in the power spectrum. This estimator, namely, centroid-shift estimator, measures the shift by calculating the relative centroid shift resulting from the applied compression. It was shown that strain estimates as high as 10% could be obtained at a reasonably high SNR. Actually, this technique provides higher SNRs for large strains than for small strains. To increase the sensitivity to small shifts in the power spectrum and provide better estimation for small strains, in [89], instead of centroid-shift, a strain estimator that uses spectral cross-correlation of the pre- and post-compression power spectrum was developed. Due to the computation of the shift over the entire spectrum, this technique provides better strain estimation at small strains with higher SNRs. However, its performance is still worse than the coherent cross-correlation techniques at small strains. Since spectral cross-correlation based methods are very sensitive to decorrelation effects, in [3], spectral scaling factor was adaptively estimated by iteratively scaling the post-compression power spectra until a maximum correlation is achieved between the pre-compression and scaled post-compression power spectra. The corresponding scaling factor is then used as a measure of tissue strain. Despite being very accurate, this adaptive spectral elastographic approach is computationally intensive owing to the iterative search structure. Therefore, in [38], a hybrid spectral strain estimation technique that locally compresses the post-compression power spectra by an approximated scaling factor and then estimates any residual strain (owing to improper scaling factor selection) using spectral cross-correlation method was developed. This way, the computational simplicity was preserved, while reducing decorrelation effects.

In addition to the incoherent techniques stated above where deformation estimation was done using RF signals, in the literature other incoherent estimators that use

envelope data to overcome the decorrelation of the RF signal have also been developed. For example, in [86], based on envelope B-mode data, the spectral shift of the post-compression power spectrum was determined by estimating the change in the mean scatterer spacing with the applied strain. The ratio of the difference in the mean scatterer spacing before and after tissue compression to the mean scatterer spacing before compression was used to estimate strain. Envelope signals were also used in [77] to estimate the displacement and strain values of vessel-mimicking phantoms. Specifically, correlation speckle tracking algorithm was acted on video echo images obtained at different static pressures to measure differential intrawall displacement of phantoms. Strain values can be calculated from these displacements estimates. For large deformations, envelope-based methods provide less noise-sensitivity than RF-based methods due to the fact that envelope-based correlation function is smoother than the RF-based correlation function [28]. On the other hand, when the deformation is small, the performance of RF signals is better than that of envelope signals due to small jitter errors [90].

In almost[2] all of these incoherent techniques, as in the coherent techniques stated before, only the radial strain component was quantified, with the circumferential component discarded. To compute lateral (i.e., circumferential) displacements, in [50], axial (i.e., radial) displacements were used by making the assumption of isotropic incompressibility in the tissue. Due to the limitation of this assumption, in [43], a new method was developed to estimate the circumferential displacement and strain. Actually, as in other correlation-based methods, in this study the cross-correlation of RF signals were used. However, the novelty is that a weighted interpolation was performed between adjacent RF signals, and the pre-compressed signal was cross-correlated with the post-compressed interpolated signals, resulting in the preservation

[2]Only in [77] both radial and circumferential strain components were estimated, however, it was assumed that an artery is an isotropic, homogeneous and cylindrical tube.

of the radial phase information in the circumferential direction and providing high-precision circumferential displacement estimates.

In all of the coherent and incoherent techniques mentioned, either RF signal or envelope signal is used to find the displacement and strain fields (generally only in the radial direction). Alternatively, B-mode[3] ultrasound images can also be used to measure 2-D tissue deformation. To date, most approaches using B-mode images to estimate tissue deformation are based on optical flow, which is a method that extracts a velocity field from an image sequence assuming that image intensity is conserved during deformation. This assumption of the pixel invariance over time is well known as the optical flow brightness change constraint [37]. In [53], the Lagrangian Speckle Model Estimator (LSME) was formulated for investigations in vascular elastography. The method was implemented through an adapted version of the Levenberg-Marquardt minimization algorithm, using the optical flow equations to compute the Jacobian matrix. Although this minimization algorithm requires a time-consuming iterative process and does not assess non-rigid motions, it was shown that LSME allows computing the full 2-D strain tensor of the artery. On the other hand, in [93] the displacement and strain distributions of non-rigid vessel walls were estimated using the intravascular ultrasound (IVUS) video images and genetic-algorithm-based optical flow method. Another method used frequently in the literature is the block matching whose purpose is to locate the best match for a 2-D block in the first image somewhere in the second image given numerous blocks of exactly the same dimensions. Fixed size block matching (FSBM) is a common method in computer vision to match moving objects from one image to the next minimizing or maximizing various measured criteria [72]. There are various matching criteria all of which assume intensity is constant over images. In [10], to acquire displacements in real-time for

[3]A two-dimensional ultrasound image, where the axes of the image correspond to the physical coordinates of the tissue, and each pixel on the image is intensity-modulated proportional to the intensity of the reflection.

in vitro datasets, the sum of absolute differences (SAD), and in [32], to determine carotid artery wall motion from B-scans, normalized cross-correlation (NCC) were used as the matching criteria. The advantage of using NCC over SAD is that NCC compensates for local variations in the mean and standard deviation (SD) of the signals. In both [10] and [32], however, FSBM was implemented where determining the size of the block is difficult in that it should be large enough to estimate large displacements, but also small enough so that the displacement remains constant within the region. To avoid this trade-off, in [73], variable size block matching (VSBM) was implemented. Additionally, automatically selected matching measures were incorporated to improve displacement accuracy, that is, NCC was used for regions of strong signal and CD_2 [21] was applied in regions of low SNR. Another optical flow-based technique called warping was implemented in [92]. Specifically, this technique uses pointwise differences in image pixel intensities between template and target image datasets to generate a distributed body force that deforms a finite element (FE) model of the template so that it registers with the target image. The drawback of [92] is that mechanical constitutive characteristics of the artery were assumed.

To eliminate these constitutive assumptions, in [17] and [58] segmentation-based optical flow techniques were developed. In the former study, the boundary of the vessel wall was detected using a non-linear variational segmentation energy [82], which is related to the technique of *curve evolution*. Then, a motion region-of-interest (i.e., a small window) was derived from the boundary, and the optical flow estimation procedure [37] was constrained to that window immediately adjacent to the vessel wall. It was shown that incorporating the boundary information in the optical flow technique has improved the displacement estimation. On the other hand, in the latter study, segmentation was performed using "B-snakes" method [55]. Unlike [17] where only the outer boundary of the vessel wall (i.e., media-adventitia interface) was determined, in [58] both the inner boundary (i.e., lumen-intima interface) and

the outer boundary were detected. Once the boundaries were detected, the centroid of the vessel was found, from which the minimum and maximum contour radii (i.e., minimum lumen radius and maximum media-adventitia radius, respectively) defining a ring-shaped region-of-interest (ROI) were determined. This way, ROI was defined as an area between the lumen-intima and media-adventitia borders. Then, the ROI in one image was registered to its counterpart in the other image in polar coordinates. The registration was performed by minimizing an energy function of the 2-D motion field based on a spline-based deformable model [85]. The energy function involves the sum of the squared difference in intensity as well as the sum of the squared difference in radial gradient at each pixel in the ROI.

2.2 High-Frequency Ultrasound

One of the most critical factors that has an impact on the preciseness of the deformation estimation is the amount of detail present in the ultrasound image. In other words, the higher the resolution of the image, the more local and reliable deformation estimation can be done. The resolution of an ultrasound imaging system is defined by the lateral extent of the ultrasound beam (i.e., circumferential resolution) and the temporal length of the pulse (i.e., radial resolution) [47]. Resolution mainly depends on the frequency and geometry of the ultrasound transducer as well as the sampling rate of RF signals and the way they are processed to form images. For example, the higher the frequency and sampling rate, the better the radial and circumferential resolutions. Circumferential resolution can also be improved by using a transducer with large diameter. In [75], using simulation the relationship between the frequency and radial resolution was explored. As expected, it was shown that there is an inverse[4] relationship between the frequency and resolution, e.g., the computed resolution was 0.5 mm, 50 μm, 20μm at 5, 50 and 100 MHz, respectively.

[4]As the numeric value of frequency increases, the numeric value of resolution decreases. Smaller numeric value of resolution means better/higher resolution.

Medical ultrasound typically uses a frequency between 1 MHz and 20 MHz, only a portion of the whole ultrasound spectrum, due to the trade-off between frequency and depth of penetration; that is, attenuation of the signal is higher at elevated frequencies, limiting the maximum exploration depth. Most commercial ultrasound systems have frequencies lower than 20 MHz due to the fact that the penetration of ultrasound waves is limited at high frequencies. As a result of this situation, few studies exist in the literature where high-frequency transducers are used[5]. In [79], in vivo detection of vulnerable plaques within coronary arteries were studied using a 20 MHz IVUS catheter to acquire IVUS frames at 80 and 100 mm Hg intravascular pressures from which incremental strain patterns of the tissue could be obtained[6]. It was shown that the resolution of the strain patterns in the radial direction was 200 μm.

On the other hand, due to the high cost and limited applicability, the use of a catheter is not always efficient and desirable. Generally, existing high frequency imaging systems rely upon mechanical scanning with a single transducer and subsequent reconstruction of image planes from the reflected ultrasonic signals [11]. For example, in [93], 30 MHz interventional single-element mechanically rotated transducer was used, and the acquired radial and circumferential resolutions were shown to be 50 and 220 μm, respectively. Similarly, in [23], 50 MHz single-element transducer, which was stepped laterally across the desired region, was used. At each position, the transducer was fired, and an RF signal was recorded. The SNR was improved by averaging multiple RF signals. The averaged signal was digitized at 250 MHz, and then the transducer was moved to the next, where another RF signal was acquired. This procedure was repeated for other lateral positions. In the end, the image was

[5]In most of the techniques stated in Section 2.1 ultrasound systems with frequencies lower than 20 MHz were used. In this section, among the techniques stated in Section 2.1 are the few ones in which high-frequency ultrasound systems were used discussed.

[6]The same group also used 30 MHz catheter in [29] and [28].

constructed from RF signals. A small deformation was then applied to the specimen as it was held in place. The imaging was repeated between several incremental deformations. The measured radial and circumferential resolution values were 52 and 71 μm, respectively.

Although recent progress has resulted in commercial arrays operating at 20 MHz [46, 80], and several groups are working to produce transducer array elements suitable for frequencies beyond 20 MHz [56, 35, 76], capturing high-frequency RF signals (e.g., 50 MHz) backscattered from a tissue is still mostly performed by using single element transducers. Since single-element transducers lack electronically steered and focused ultrasound beams, to scan a 2-D cross-section of the tissue there is a need for an experimental setup where either the transducer or tissue can be moved (e.g., see [23]). Moreover, using a high-frequency ultrasound transducer is necessary, but not sufficient to get high-resolution ultrasound images. The digitizer (e.g., oscilloscope) with high bandwidth and sampling rate is also required to improve the resolution of ultrasound images. As far as coronary arteries are concerned, high-resolution images would be able to get both inner and outer boundaries of intima, media and adventitia detected, improving the resolution and locality of estimated strain patterns.

2.3 Segmentation

Segmentation, the partitioning of the original set of image points into subsets corresponding to the structures, can be used as an intermediate step in the estimation of tissue deformation. For example, as stated in Chapter 1, detection of the boundaries of intima, media and adventitia in coronary artery ultrasound images makes the comparison of those images easy and reliable, resulting in much more accurate strain estimation. Among various segmentation techniques [69], active contours (also called snakes) are well known to provide good detection of object boundaries. The technique of active contours is based upon the utilization of deformable contours that conform

to various object shapes and motions [54]. In the classical theory of active contours, an arbitrary curve is first initialized in an image. This curve is then designed to move under the influence of internal and external image dependent forces while minimizing an energy term including some well adapted internal and external forces [41]. The internal forces control the contour elasticity and its resistance to bending, thereby imposing smoothness on the curve. On the other hand, the external forces defined by the image features (e.g., image intensity) push the contour toward boundaries. However, there may be a number of problems associated with this classical approach such as difficulty in conforming to the image concavities and in segmenting objects that have sharp corners, existence of multiple minima and dependence on the parametrization.

Due to the limitations of the classical active contour model, much research has been done on improving the basic snake framework. In [8], the snake-growing algorithm that allows snake to grow along features and also break by using local features was developed. In [34], a dual active contour model where two curves approach boundaries both from inside the object and from the background was introduced, while in [98] a split-and-merge technique was implemented to make the snake track the concave boundaries. Moreover, in [25], inertial force, which modifies itself depending on the previous position of the contour and pushes the snake to the object edges, was added to the internal force terms. This way, the spline motion was controlled through the concavities as well as against the weak edge forces. For the computation of the energy minimizing spline, the greedy algorithm [94] was used as opposed to the variational calculus widely used to solve the snake model [41].

There are also some active contour models developed to segment the intravascular ultrasound images. For example, in [45], an active contour algorithm was used to identify the lumen and media-adventitia borders. A balloon force was added to the classical framework to force the contour to inflate or deflate, and prevent it from shrinking to a point. In [13], statistical information was incorporated to the active

contour model to detect the luminal border in an intracoronary ultrasound image. In this automatic method, it was assumed that B-mode image brightness can be modeled by Rayleigh distribution, according to which a contour evolves until it detects the lumen boundary. Also, in [99], active contours were implemented to segment the coronary artery vessel wall; however, to detect the edges, the edge contrast, which is defined as the gray level gradient of boundary normalized by the intensity of the inner side background along it, was used rather than the gray level gradient used in the classical active contour model. Moreover, in this study dynamic programming [4] was adapted to solve the contour evolution problem. Finally, in [70], instead of dynamic programming, Hopfield neural network [100] was used to implement the active contour algorithm for the detection of lumen-intima and media-adventitia borders.

The active contour approaches stated above are non-intrinsic, since the energy functions depend on the parameterizations of the contours. This is an undesirable situation, because parameterizations are not related to the geometry of the contours (or object boundaries), but only related to the velocity they are traveled [16]. Those approaches also cannot directly deal with changes in topology. Another problem of those approaches where an energy function is minimized to locate the contour is the need to select three parameters that control the trade-off between contour elasticity, rigidity and proximity to the object. To solve the latter problem, in [16], [96] and [42] the problem of minimizing the energy function was transformed into a problem of geodesic computation in a Riemannian space. This scheme, known as the *geodesic active contour*, efficiently attracts the given curves to the features of interest. The geodesic active contour model employs ideas from Euclidean curve shortening evolution that defines the gradient direction in which the Euclidean perimeter is shrinking as fast as possible [96]. Furthermore, when implemented using level-sets [65], the geodesic active contour model overcomes the other problems of classical energy methods mentioned above. Another advantage of geodesic active contours is

that they provide extra power to attract the evolving contour as it approaches an edge, and to push the contour back out if it passes the edge.

CHAPTER III

IMAGE ACQUISITION

In Section 2.2, one of the key elements of ultrasound imaging, i.e., resolution, which mainly depends on the frequency of the transducer, sampling rate of RF signals and image formation & processing techniques used, was discussed. To date, the best resolution values obtained in the literature are around 50 μm, which is not enough to see clearly all boundaries of the coronary artery vessel wall, namely, lumen-intima, intima-media, media-adventitia, adventitia-fat and very outer fat[1]. With that level of resolution, as can be seen in Figure 1 [99] where an example of a typical coronary vessel wall image acquired in the literature is shown, only lumen-intima and media-adventitia boundaries are able to be detected, which would significantly limit the resolution and locality of the estimated strain fields.

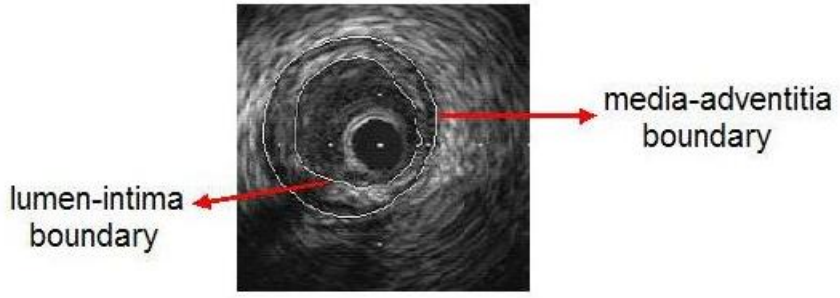

Figure 1: Coronary vessel wall image acquired using 40 MHz intravascular catheter

Therefore, one of the main objectives of this thesis, as mentioned in Section 1.1, is to acquire high-resolution coronary vessel wall ultrasound images. In the following sections, the steps followed to acquire those high-resolution images are explicitly

[1]Throughout the text, for the sake of simplicity, instead of "lumen-intima", "intima-media", "media-adventitia", "adventitia-fat" and "very outer fat" terms, "inner intima", "outer intima", "inner adventitia", "outer adventitia" and "fat" terms are used, respectively.

discussed. First of all, an experimental setup that involves ultrasound data acquisition and organ culture systems is designed. The details of this experimental setup is discussed in Section 3.1. Then, in Sections 3.2 and 3.3, how RF data are acquired from the experimental setup and how B-mode high-resolution ultrasound images are formed from the RF data are explained, respectively.

3.1 Experimental Setup

Since an ultrasound machine that is capable of providing high-resolution coronary vessel wall images has not been developed yet, a system whose schematic diagram is shown in Figure 2 was designed to capture and display ultrasonic signals reflected back from the vessel wall. The specifications of the equipments used can be found in Appendix A.

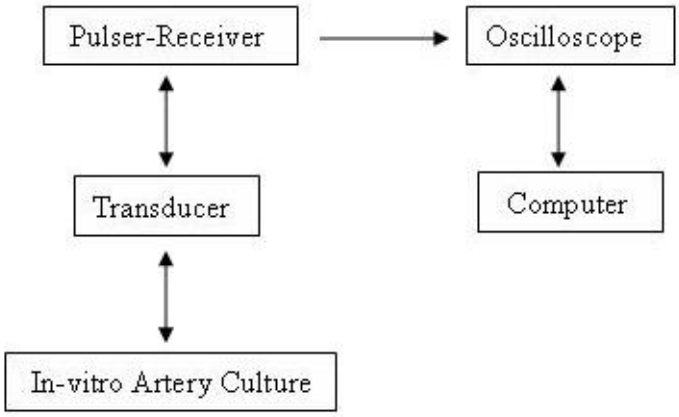

Figure 2: Ultrasound data acquisition system

The pulser-receiver generates a short, high voltage (less than 20 ns in duration and 100-500 V in amplitude) electrical pulse to be transmitted to the transducer. The transducer converts this electrical excitation pulse to an ultrasonic pulse, which

then propagates into the coronary vessel wall inside the in-vitro culture. A portion of this ultrasonic pulse is reflected from the interfaces between the layers (with different acoustic properties) of the vessel wall. The transducer also receives those reflected pulses and converts them back into electrical signals to be sent back to the pulser-receiver where they are amplified. These amplified RF signals are sent to the oscilloscope to be digitized and displayed. Also, to store the sampled signals oscilloscope is connected to the computer using the GPIB (IEEE 488) interface. In this developed setup, in-vitro artery culture was designed in such a way that the artery placed inside the culture could be rotated about its axis as well as be pressurized from inside (see Figure 3a). The artery was mounted on the cannulae inside the plexiglas chamber filled with Phosphate Buffered Saline (PBS) (Sigma P3813 Phosphate Buffered Saline, pH 7.4). The cannulae that have grooves on them to enable fastening of the arteries to prevent any leakage during the pressurization (see Figure 3b) were placed on a gear system, which provides the rotation of the artery and is electronically controlled using USB based data acquisition device. Peristaltic pump was used to pump Phosphate Buffered Saline into the coronary artery vessel wall and so develop pressure inside the wall, while the pressure was monitored using an electronic pressure transducer.

Another challenge in this experiment was specimen acquisition. Since porcine hearts could be acquired more easily than human hearts, and their physiology and anatomy are very similar to those of humans [71, 40, 91], porcine hearths obtained from a local farm were used in this study (see Figure 4a). After approximately 3-4 hour sacrifice, the right coronary artery (RCA) was excised from the intact heart (see Figure 4b). Right coronary artery was preferred over left coronary artery due to having fewer number of branches, minimizing the probability of leakage occurrence during the pressurization of the artery [51].

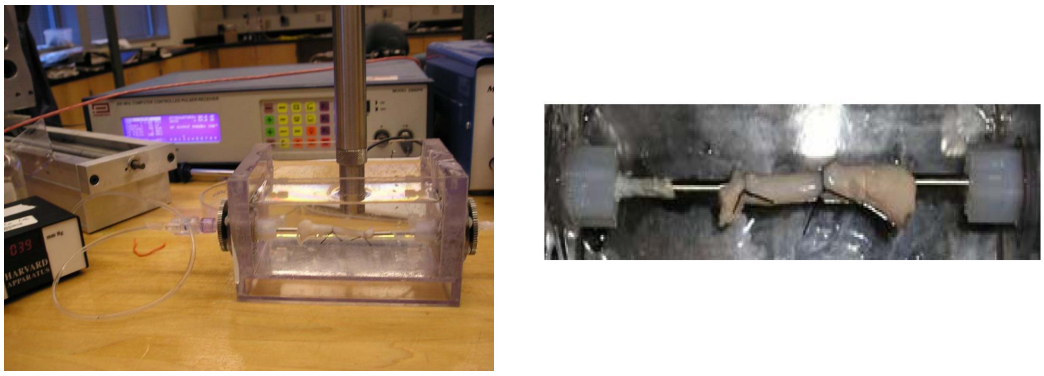

(a) (b)

Figure 3: (a) In-vitro artery culture setup, and (b) Artery tied onto the cannulae inside the culture setup

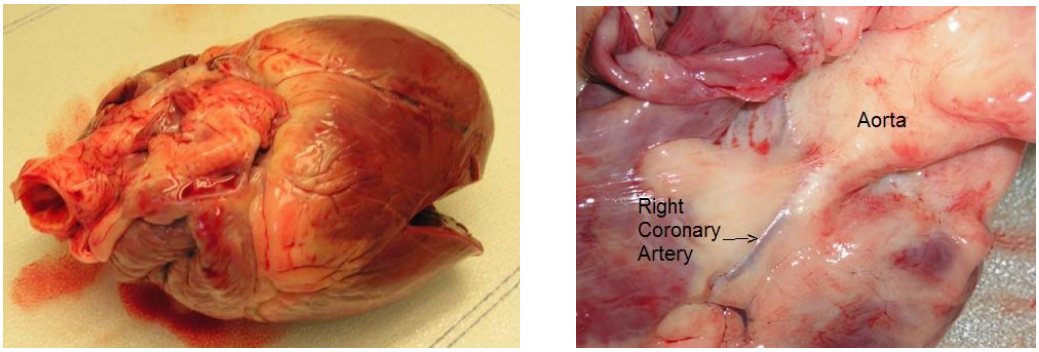

(a) (b)

Figure 4: (a) Porcine heart, and (b) RCA and aorta of the porcine heart

3.2 Data Collection

The experimental setup described in Section 3.1 allowed the rotation of the artery about its axis while the transducer was fixed above it. LabVIEW software and Minilab 1008, which is a USB based data acquisition device and connected to the gear system, were used to control the movements of the artery. To get good signals, at the beginning of the experiment the distance between the face of the transducer and the

artery was kept approximately 12.7 mm, which is the focal length of the transducer[2].

Since the aim was to collect RF signals corresponding to a 2-D cross-section of the artery under different pressures, there were two options as far as the way data acquisition could be performed: i) fix the pressure, rotate the artery in regular increments until scanning the desired sector of the artery and get RF signals at each rotation, then increase pressure, and repeat the process, or ii) first get RF signals for a particular 1-D cross-section[3] of the artery at desired pressures, then rotate the artery some degree and acquire RF signals at the same pressure values for this new 1-D cross-section, and so on. Although the former option could be done in an automated way (i.e., while artery is being rotated at fixed pressure, signals are acquired automatically at each rotation) using LabVIEW, because of the following reasons the latter option was followed in this experiment. First, images formed using the first option might be significantly uncorrelated, since artery might not be rotated exactly about its center. This is an image registration problem and may be challenging to solve in this situation. The problem is even worse, because during the rotation of the artery, the wheels might get stuck or a bubble formation might take place on the face of the transducer due to its spherical concave lens. In such an automated measurement, detecting and resolving these problems would be significantly difficult, causing the acquisition of inaccurate and uncorrelated signals that would result in the formation of incomparable images. Second, to get high-resolution images the sampling rate needs to be high, requiring the use of small time scales on the oscilloscope screen. Here, the drawback is that during the rotation or pressurization of the artery a portion of the RF signals coming from the vessel wall may leave the screen due to

[2]As artery was being pressurized, this distance changed; but, it was observed in the experiment that the signal quality did not reduce significantly.

[3]Although the diameter (or width) of a sound beam is not zero, for the sake of explanation each sound beam is considered moving along the 1-D trajectory. Then, by rotating the artery and emitting beams along the corresponding 1-D trajectories at each rotation, 2-D cross-section of the artery can be scanned (See Appendix B for the related figure).

the small time range used. In that situation, the X-shift of the oscilloscope needs to be adjusted, which would be another challenge for an automated method.

Therefore, in this experiment, first for a particular 1-D cross-section of the artery RF signals at all of the desired pressures were acquired. Then, the artery was rotated by some degree, and the signals at those same pressure values were collected for this new 1-D cross-section. This process was repeated until the desired sector of the corresponding 2-D cross-section of the artery was scanned. The drawback of this method is that it cannot be done in an automated way. However, it's worth doing since it can resolve all of the problems stated above for the other option, resulting in accurate, correlated and high-resolution RF signals and ultrasound images. To be able to observe and analyze the behavior of the artery under low, medium and high stresses, data were acquired at three pressure values, that is, 30, 60 and 90 mmHg. As a low pressure, 30 mmHg was selected instead of 0 mmHg, because the artery shrinks when harvested from the heart due to its release from in vivo stretch. From the beam diameter of the transducer and the radius of the artery, rotation angle was calculated. For the purposes of this study, 40°- 45° sector of the artery was scanned to show the applicability of the proposed research. The computational details of the data acquisition process are given in Appendix B.

One of the main advantages of the developed experimental system is the high-sampling rate. Specifically, very small time scale, 0.2 μs/division or 2 μs/signal (for 10 divisions), was used while digitizing an RF signal and acquiring 2000 sampled points (maximum possible number). This would make the sampling rate $\frac{2000sa}{2\mu s} = 1$ G$sa/s = 1$ GHz, which is significantly higher than the average rate (200 MHz) used in the previous studies.

In Figure 5a is shown an example of an RF signal (corresponding to a 1-D cross-section of the artery at 30 mmHg) constructed from 2000 sampled data points. However, due to the presence of background noise this signal indeed does not correspond

to the actual ultrasound waves reflected from the boundaries of the artery. Using high-frequency transducers that have buffering to alleviate internal reflections causes this random background artifact mixing with the actual signal from the target [20]. Therefore, there is a need to acquire a blank RF signal (i.e., noise signal with no target) like the one shown in Figure 5b.

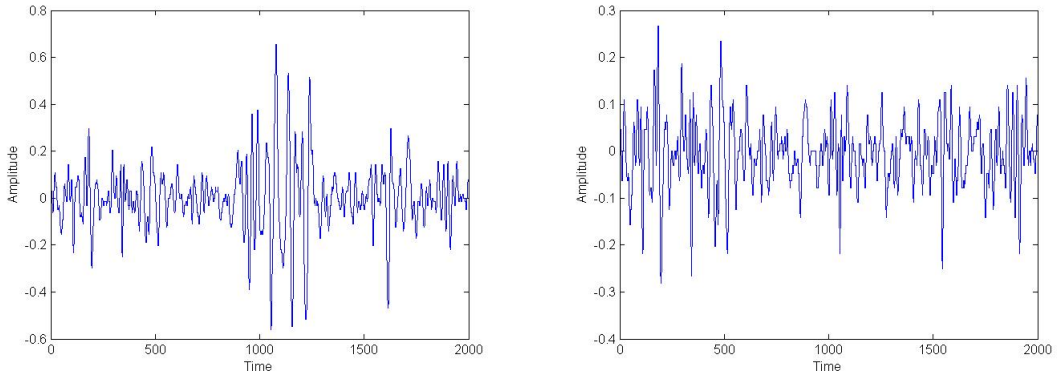

(a) (b)

Figure 5: (a) Unfiltered RF signal, and (b) RF signal with no target

Subtracting this noise signal from the acquired signal shown in Figure 5a provides the actual signal corresponding to the proximal wall[4] of the artery at 30 mmHg (see Figure 6a). Similarly, the actual signals corresponding to the same 1-D cross-section of the proximal wall can be recorded for 60 and 90 mmHg as shown in Figures 6b and 6c.

In all figures, the vertical axis corresponds to the amplitude of the signal (in volt), which is proportional with the strength of the boundary (i.e., how much the acoustic properties of the tissues making up the boundary are different). On the other hand, the horizontal axis corresponds to the indices of the sampled data points and is proportional with the time values at which the sampled signals have reached the

[4]Proximal wall is the part of the wall that is closer to the transducer than the other part, which is called distal wall. In other words, from the location of the transducer proximal wall is placed ahead of the lumen, while distal wall is beyond the lumen.

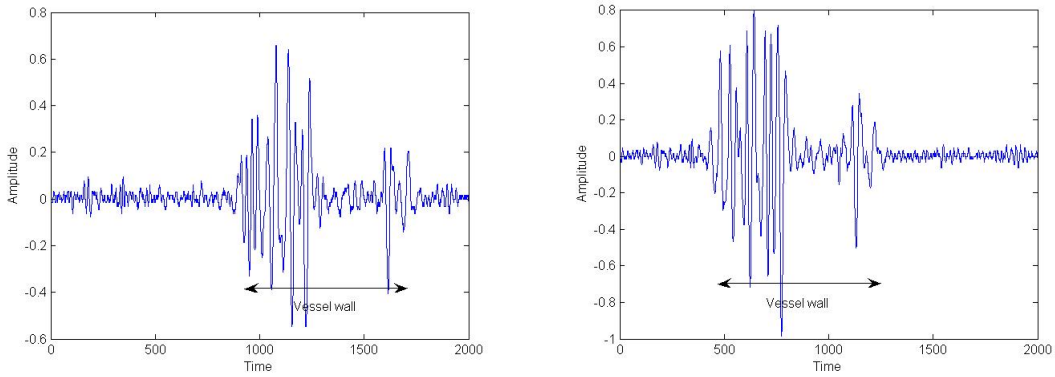

(a) (b)

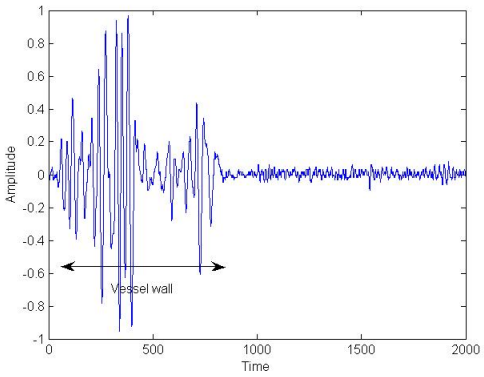

(c)

Figure 6: Filtered RF signals at (a) 30 mmHg, (b) 60 mmHg, and (c) 90 mmHg

transducer. For example, the part of the signal with label 0 reaches the transducer 2 μs earlier than that with label 2000. Actually, this time difference is proportional with the distance between the locations where those parts of the signal have been reflected. The exact relationship between time and distance is given in Eq. 1:

$$t = \frac{2d}{c} \tag{1}$$

where c is the velocity of the sound in the soft tissue, which is 1540 m/s, d is the one-way distance, and t is the observed round-trip time. For the plots in Figure 6, as pressure increases, the part of the RF signal corresponding to the vessel wall moves

to the left, meaning that the distance between the transducer and the vessel wall decreases, as expected. Another observation from these plots is that on average the amplitude values of the part of the signal corresponding to the vessel wall are slightly larger at high pressures than at low pressures. This situation occurs due to the fact that ultrasound waves exponentially attenuate while traveling through the medium. Since at high pressures waves travel less distance, the amplitude decay of the signal becomes also less than that at low pressures.

3.3 Image Formation

After RF lines[5] acquired at same pressure values were put together and attenuation losses stated in Section 3.2 were compensated by multiplying their amplitude values by attenuation coefficients (see Appendix C for details), the first step in the image formation process was to perform scan conversion and represent data on a standard gray-scale display. This conversion was done in such a way that a pixel of the image to be formed would represent 10 sampled data points. In other words, 2000 points sampled from RF signals would correspond to 200 pixels. This 10 : 1 ratio was chosen after some trials to balance the SNR and resolution of the image to be formed. Then, the next step was to perform two-dimensional interpolation among RF lines[6]. This way, there would be smaller rotation angle differences between consecutive RF lines, resulting in higher circumferential resolution.

Having finished the interpolation process, three matrices, each of which involves the collection of RF lines at particular pressure, were formed in the polar coordinate system. For the sake of display, polar coordinate system was converted to cartesian coordinate system; however, to accomplish this, first, every element of each matrix was relatively located by being assigned radial and angle values. Basically, radial

[5]The terms "RF line", "RF acquisition" and "RF signal" are used interchangeably to denote a signal (which consists of 2000 sampled data points) acquired for a particular 1-D cross-section of the artery at a certain pressure.

[6]The details of the interpolation performed are given in Appendix C.

values provide the relative distances of the elements from the origin (i.e., center of the artery axis), while angle values show which RF lines the elements belong to (see Appendix D for details).

After the coordinate system conversion, the next step was to amplitude modulate the RF signals so that images would not contain any high frequency "carrier" signals. To accomplish this goal, the Hilbert transform, which is a relative of the Fourier Transform, was used. The Hilbert Transform has the property that all cosines are transformed to negative sines and all sine components are transformed into cosines. It also determines the analytical signal, $a = a_r - i \times a_i$ that has a real part, a_r, which is the original data, and an imaginary part, a_i, which contains the Hilbert transform. The imaginary part is a version of the original real sequence with a 90° phase shift. The absolute value of the analytical signal provides the envelope of the RF waveform. After the envelope detection of RF signals was performed, the last step was to apply non-linear compression to the image data, helping to use the dynamic range of the display by showing weak echoes on the same scale with strong signals. This image formation process was implemented using MATLAB.

The formed ultrasound images of the proximal wall of a coronary artery at 30 mmHg, 60 mmHg and 90 mmHg are shown in Figures 7, 8 and 9, respectively. Each image has a size of 400×400, and its right bottom corner corresponds to the center of the artery.

Since each RF line corresponds to 2000 data points with total duration $2\mu s$, time difference between two consecutive data points would be 1 ns, making the time difference between two consecutive pixels in the radial direction 10 ns. Then, using Eq. 1 the real distance between adjacent pixels in the radial direction can be computed as follows: $d = \frac{c \times t}{2} = \frac{(1540m/s) \times (10 \times 10^{-}9s)}{2} = 7.7\ \mu m$, which can be called a "resolution" in terms of *μm per pixel*. In other words, the formed images shown in Figures 7, 8 and 9 have the *radial resolution* value of 7.7 μm, which is much better than the literature

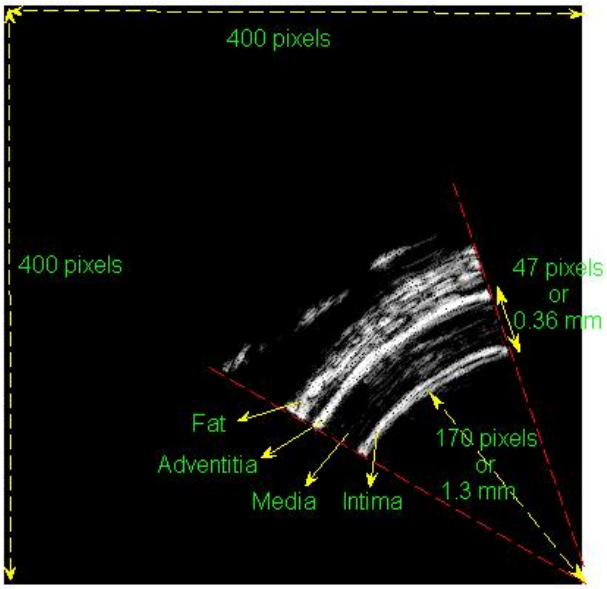

Figure 7: Ultrasound image of the coronary vessel wall at 30 mmHg

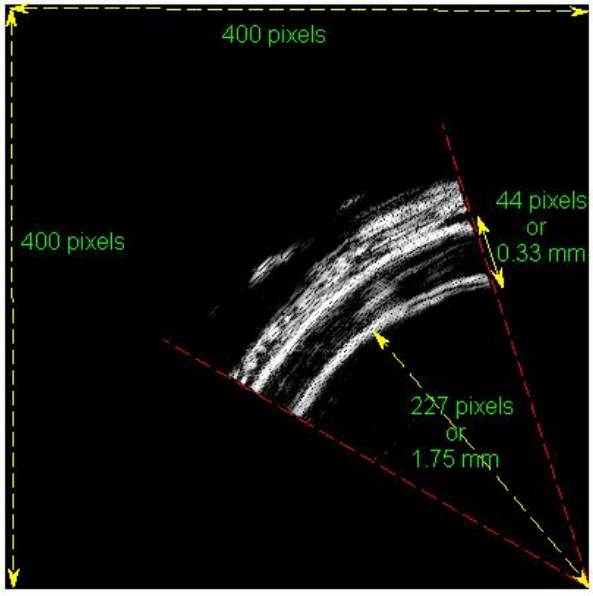

Figure 8: Ultrasound image of the coronary vessel wall at 60 mmHg

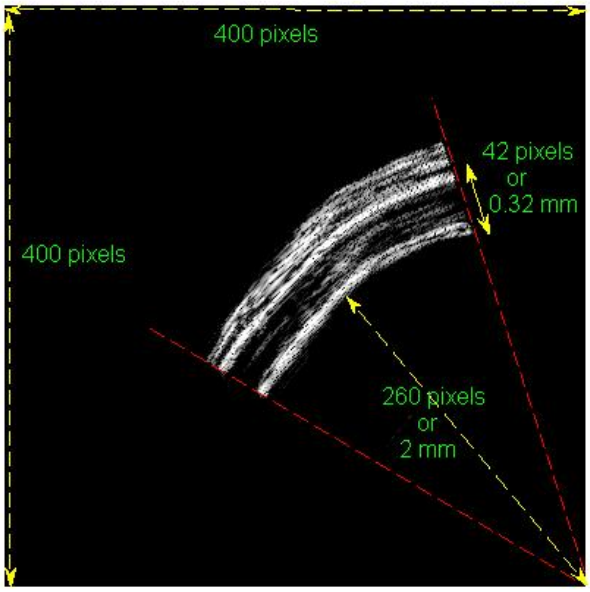

Figure 9: Ultrasound image of the coronary vessel wall at 90 mmHg

findings where the best radial resolution value obtained has been around 50 μm.

As far as the circumferential resolution is concerned, there is a need to estimate the real circumferential distance between adjacent RF lines, all of which are located in the image radially. As explained in Appendix C, the angle between two consecutive RF lines is 0.28°. Also, since the distance between adjacent RF lines increases as the radius (i.e., the distance from the center of the artery) increases, here the worst case, which is the adventitia boundary in Figure 9 having the largest radius (2.32 mm) among all boundary points in three images, would be considered. Then, the *circumferential resolution* would be: $2\pi r \times \frac{0.28^\circ}{360^\circ} = 2\pi(2.32mm) \times (7.7 \times 10^{-}4) = 11.3\ \mu m$[7], which is also much better than the literature findings where the best circumferential resolution value obtained has been around 70 μm.

[7]Using interpolation among RF lines has helped to obtain this significantly good circumferential resolution value.

Computation of mean circumferential wall tension using Laplace's Law: The forces acting on the artery during the pressurization are shown in Figure 10 [57], where T is circumferential wall tension, P is internal pressure and R is internal radius.

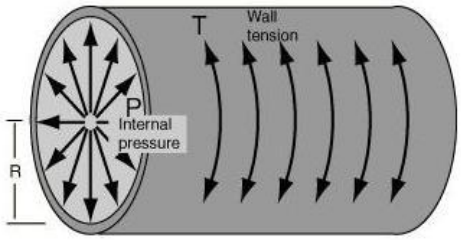

Figure 10: Force balance in a coronary artery wall

Laplace's Law [81] states that the larger the vessel radius, the larger the wall tension required to withstand a given internal pressure. In other words, the equation of Laplace's Law is:

$$T = PR \tag{2}$$

Non-linear behavior of coronary artery vessel walls: By using pressure and average radius values given in Figures 7, 8 and 9 along with Eq. 2, a plot of "T vs R" can be drawn as shown in Figure 11[8].

Onto this plot are placed straight lines, each of which represents the Laplace relationship at a different pressure. The pressure value that each line represents is equal to the slope of that line (after the unit conversion). As can be seen, each straight line has only one point of intersection with the artery curve, representing the equilibrium mean radius for the artery at that pressure. For example, when pressure is increased from 30 mmHg to 60 mmHg, the lumen radius increases from 1.3 mm to

[8]For this plot, the unit of pressure values was changed from $mmHg$ to g/mm^2 by multiplying them by $1.3595 \times 10^{-}2$. The unit of radius values was still taken as mm, which makes the unit of tension values g/mm. Also, the curve on the plot was drawn using spline interpolation.

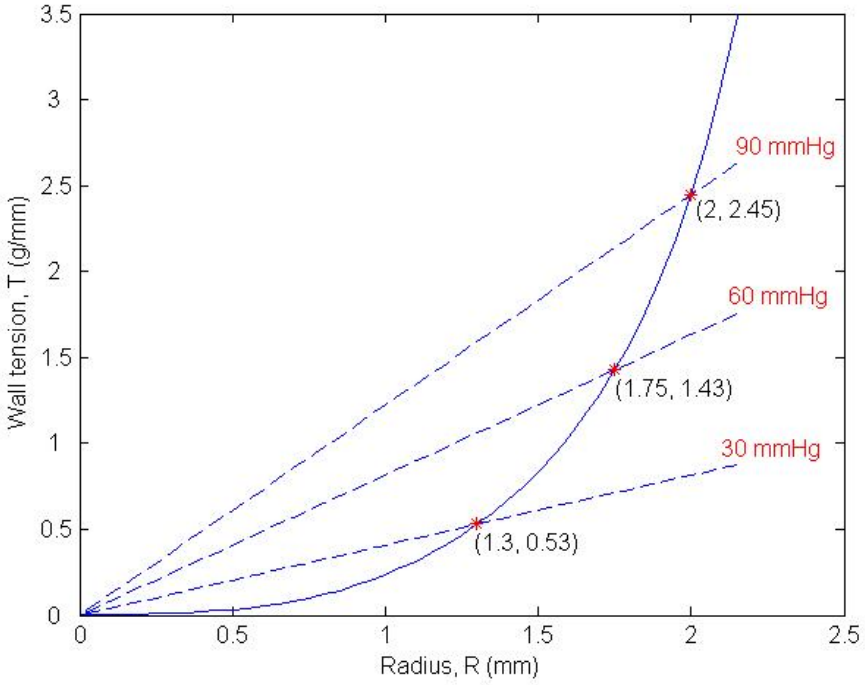

Figure 11: A J-shaped wall tension-artery radius curve

1.75 mm, while tension inside the intima also rises from 0.53 g/mm to 1.43 g/mm. Same behavior occurs while moving from 60 mmHg to 90 mmHg except that the increase in radius is smaller now. Actually, this can be clearly seen from the fact that the J-shaped tension-radius curve in Figure 11 has a continuously increasing slope. This behavior is nothing but the non-linear behavior of vessel walls when distended. This way, elastic stiffness increases with the degree of loading, making the vessel wall stable under increasing pressure and protecting it against aneurysms and "blowout" [15, 33, 9].

Another observation from Figures 7, 8 and 9 is that there is a decreasing trend in wall thickness as pressure increases (i.e., on average 0.36 mm, 0.33 mm, 0.32 mm at 30, 60 and 90 mmHg, respectively). Thus, the artery becomes wider but thinner with increasing pressure. This kind of behavior of the artery (i.e., while being stretched in one direction, it is being compressed in the perpendicular direction) would make its

Poisson's ratio positive. The positive Poisson's ratio is one of the common properties of soft tissues, showing the resistance to a change in volume. Also, in [14], it is shown that the volume distensibility is inversely proportional with $\frac{Eh}{R} - P \geq 0$, where E is the elastic modulus (i.e., stiffness), h is the wall thickness, R is radius and P is pressure. As P increases, R will increase and h will decrease. If E were always constant (i.e., linear elasticity), then with increasing pressure $\frac{Eh}{R} - P$ would become smaller and smaller approaching 0 and eventually cause rupture of the vessel wall. But, in reality, non-linear elastic properties of the vessel wall make E increase, protecting the wall against aneurysms as well as minimizing its volume change under increasing pressure.

Computation of mean circumferential wall stress: From the mean wall thickness and circumferential wall tension, another important element, namely, mean circumferential wall stress (σ_θ) can also be calculated as follows:

$$\sigma_\theta = \frac{P \times R}{h} = \frac{T}{h} \tag{3}$$

.

As can be seen in Eq. 3 [95], coronary artery circumferential stress increases with increasing arterial pressure. However, there is no linear relationship between these two terms, because an increase in pressure also results in an increase in the radius and a decrease in the wall thickness. In other words, as pressure increases, the rate of increase of the wall stress is also expected to increase. In Figure 12, "mean circumferential stress vs pressure" curve is plotted using the obtained pressure, radius and wall thickness values. Indeed, there is a kind of quadratic relationship between pressure and circumferential stress, meaning that with increasing pressure the slope of the curve also increases. Computation of mean circumferential stress using its relationship with pressure is an important step in estimating the vulnerability of the vessel wall and plaque, because the circumferential wall stress is generally thought to

be an important determinant of plaque rupture [74, 48, 18].

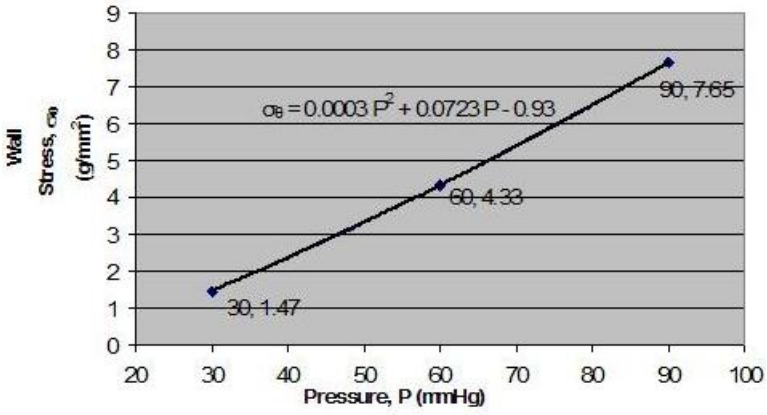

Figure 12: Quadratic circumferential wall stress-arterial pressure curve

CHAPTER IV

IMAGE SEGMENTATION

The coronary vessel wall ultrasound images shown in Figures 7, 8 and 9 have provided information about how lumen radius and wall thickness change with increasing pressure. Also, using Eqs. 2 and 3, the mean circumferential tension and stress have been calculated in Subsection 3.3. Although all of these are necessary to understand the behaviors of coronary arteries under pressure applied, these findings are global information and not sufficient to determine the composition and mechanical properties of coronary artery vessel walls, because they cannot provide any information about the deformation behavior of individual layers. To fully understand the characteristics of the vessel wall, therefore, there is a need to obtain local strain fields within each layer of the vessel wall. Without local strain fields, it would not be possible to determine whether or not strain patterns of the intima, media and adventitia are same for an applied pressure differential as well as within each layer the distribution of those strain patterns is uniform.

4.1 Edge-Based Segmentation

One of the best ways of estimating the strain fields within a layer is to track the deformations of its boundaries. This "boundary-based" approach indeed would exploit the high resolution level of the formed images where both inner and outer boundaries of each layer can be visualized as opposed to the other typical vessel wall images where either inner or outer boundary can be visualized (e.g., see Figure 1). This approach would also provide much more reliable and accurate strain estimations than any other approach could as long as the boundaries are able to be accurately detected in a technical way. Besides, as stated in Section 2.1, unlike correlation-based methods,

segmentation-based techniques developed in the literature have provided promising results to investigate complex strain patterns.

The main challenge, however, for the proposed "boundary-based" approach is that images formed in Figures 7, 8 and 9 involve considerable amount of noise[1]. In Section 2.3, active contour-based segmentation techniques, which have been used by many research groups for the segmentation of various kinds of medical images, were reviewed. Among active contour techniques are geometric active contour models called *geodesic active contours* very powerful in extracting features from images since they can eliminate the limitations of classical active contour models (snakes). However, their performance, like that of any other segmentation algorithm, is likely to be degraded by the noise present in the high-resolution ultrasound images formed. Thus, there is a need to develop robust, i.e., noise-insensitive, geodesic active contour-based segmentation algorithm to detect the boundaries of noisy coronary artery ultrasound images shown in Figures 7, 8 and 9.

4.1.1 Geodesic Active Contours

The energy and corresponding curve evolution equations of the geodesic active contour model [16, 96, 49, 52, 68] are given in Eqs. 4 and 5, respectively:

$$E = \int_{\overrightarrow{C}} \phi \, ds \tag{4}$$

$$\overrightarrow{C_t} = \phi\kappa\overrightarrow{N} - (\nabla\phi \cdot \overrightarrow{N})\overrightarrow{N} \tag{5}$$

where $\overrightarrow{C}$ is the curve to be evolved, s represents the arclength parameter of $\overrightarrow{C}$, κ is the curvature, ∇ is the gradient, $\overrightarrow{N}$ is the unit inward normal, and the function ϕ depends on the given image and is called "stopping term." Generally, ϕ is defined in

[1]Ultrasound images have already lower SNRs than any other medical images. When their resolution levels are also high, which is the case in this research, their SNRs become much lower.

such a way that it has a very small magnitude in the vicinity of an edge[2] and so acts to stop the evolution when the contour gets close to an edge. For example, in [67] and most of the other active contour studies, the stopping function shown in Eq. 6 is used. Here, I corresponds to the image (i.e., intensity values of gray-scale image), and since $\|\nabla I\|$ has large values around edges, ϕ goes to 0 on the edges.

$$\phi = \frac{1}{1 + \|\nabla I\|^2} \tag{6}$$

4.1.2 Level Set Methods

In the literature, curve evolution has been initially proposed using a parametric representation of the curve, which is difficult to implement. Another difficulty with curve evolution is the possibility of forming singularities and sharp corners, which are called shocks. To address these problems, *level set methods* [65] are used in the implementation of geodesic active contours. The idea behind level set methods is that instead of evolving a curve in a two dimensional (2D) plane, which requires parametrization of the curve, a 2D function is evolved in 3D, which is a much easier problem. The zero level set of this function is smartly arranged to correspond to the curve that is being evolved. Then, evolving the level set function and tracking the evolution of its zero level set automatically give the evolution of the curve. The level set equation of the curve evolution defined in Eq. 5 is given in Eq. 7:

$$\psi_t = \phi\|\nabla\psi\|\kappa + \nabla\phi\cdot\nabla\psi \tag{7}$$

where ψ is the level set function. The first part of Eq. 7 is called the *diffusion term*, while the second part is called the *transport term*. The diffusion term includes the stopping function (ϕ), while the transport term includes the gradient of the stopping

[2]Except edges where it becomes 0 or very close to 0, at other locations stopping function is always positive.

function ($\nabla\phi$). When the value of ϕ becomes zero, both terms vanish and the evolution of the curve stops. Here, the effect of $\nabla\phi$ is to attract the evolving contour as it approaches an edge, and to push the contour back out if it passes the edge [42].

4.1.3 Stopping Function Design

The challenge in the segmentation of the formed images given in Figures 7, 8 and 9 is the noise present in those images. Specifically, as can be seen from the images, it might be challenging to detect the boundaries between fat and adventitia, media and adventitia as well as media and intima because of the significant amount of artifact. Actually, the challenge is much severer when geodesic active contours, which generally have been applied effectively to images with high SNR, are used to detect the boundaries. As can be seen from Eq. 6, in classical geodesic active contour models the stopping function (ϕ) involves the gradient of an image. Moreover, as explained in Subsection 4.1.2, the transport term of Eq. 7 involves the gradient of the stopping function ($\nabla\phi$). This means that in classical active contour models the second derivative of the image affects the evolution of the level set function, making the segmentation very vulnerable to noise.

To make the segmentation more robust to noise, in this research a novel stopping function that involves both gray-scale amplitude[3] (I) and local phase of the image is proposed. Before investigating the details of the proposed stopping function, there is a need to explain how phase information can be used to detect the boundaries of an image. The Fourier Transform of a signal can be a complex signal. Thinking of the Fourier transform as a decomposition of the signal into sinusoids, the argument of the signal (i.e., phase) describes the spatial (or time) shift the sinusoid undergoes [59]. Signals that are evenly symmetric about the origin will have real Fourier transforms,

[3]From now on, to denote the gray-scale image values, instead of the term "intensity", the term "amplitude" will be used to make the terms used compatible with each other (i.e., "phase" and "amplitude").

while signals that have an odd symmetry will have imaginary Fourier transforms. Thus, the cosine has a real Fourier transform, meaning that its Fourier phase is 0 or π. Similarly, the sine has a purely imaginary Fourier transform, and its Fourier phase is $-\pi/2$ or $\pi/2$.

The local phase aims to mimic the behavior of the Fourier phase of a signal, localized by a spatial windowing function. While the Fourier phase describes spatial relations globally, the local phase gives a symmetry statement about the signal in a certain position. The local phase of a signal f(x) in 1-D is the argument of the analytic function $f_a(x) = f(x) - i \times f_{hi}(x)$, where $f_{hi}(x)$ denotes the Hilbert Transform of $f(x)$, as introduced before. The signal $f(x)$, e.g., the intensity along a row of pixels in an image, and its local phase are shown in Figures 13a and 13b, respectively [60].

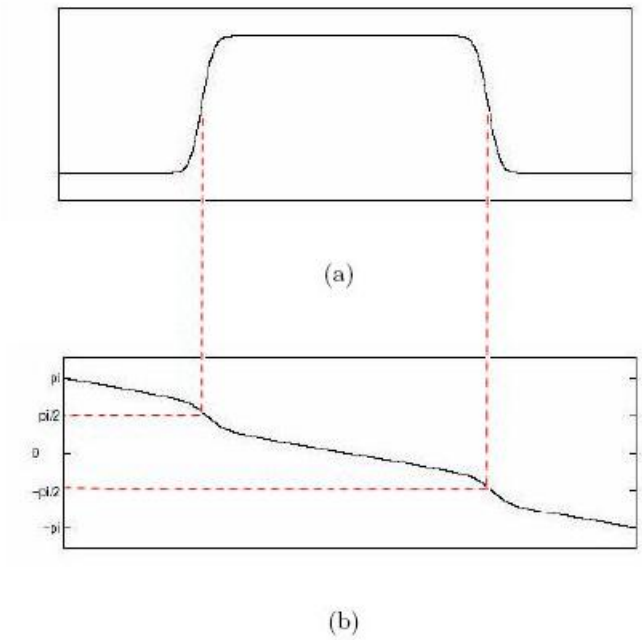

Figure 13: (a) A simple 1-D signal, and (b) its local phase

In Figure 13a, there are two edges or regions where the signal shape is locally odd, and the phase curve reacts to each, giving phase values of $\pi/2$ and $-\pi/2$. In 2-D, for each pixel there will be two phase values, namely, θ_x in the x direction and θ_y in the

y direction. Thus, edges are expected to have phase values (θ_x or θ_y or both) that are odd multiples of $\pi/2$.

The proposed stopping function exploits the usefulness of phase knowledge in the detection of boundaries. Actually, this novel stopping function involves two terms, one from gray-scale amplitude knowledge and one from phase knowledge. The amplitude-based term (so called $\phi_{amplitude}$) is the same as Eq. 6, while the phase-based term (so called ϕ_{phase}) is given in Eq. 8. In Eq. 8, the square cosines of the phase values are taken, because the stopping function must be vanished at the edges and be positive at other locations, as mentioned in Subsection 4.1.1, and also at the edges phase values are odd multiples of $\pi/2$ whose cosines are 0. Then, the novel stopping function is developed as given in Eq. 9, where $0 \leq \lambda \leq 1$ is a weighting factor between amplitude-based and phase-based terms.

$$\phi_{phase} = \cos^2(\theta_x)\cos^2(\theta_y) \tag{8}$$

$$\phi = \lambda\phi_{phase} + (1-\lambda)\phi_{amplitude} \tag{9}$$

Comparison of $\phi_{amplitude}$ and ϕ_{phase} shows that the latter one has eliminated the gradient operation and thus become more robust to noise. The superiority of ϕ_{phase} over $\phi_{amplitude}$ in terms of noise-insensitivity can be clearly seen in Figure 14. Using ϕ_{phase} as a stopping function gets the curve evolved under the effect of only one derivative (coming from the gradient of the stopping function in the level set equation) as opposed to two derivatives, which is the case when $\phi_{amplitude}$ is used. But as will be seen in Subsection 4.1.4 and discussed in Subsection 4.1.5, ϕ_{phase} has also a drawback (i.e., weakened stopping power), implying that there is a need to include both $\phi_{amplitude}$ and ϕ_{phase} in the stopping function.

The proposed geodesic active contour-based segmentation algorithm involving this

(a)

(b) (c)

Figure 14: (a) 30 mmHg coronary vessel wall image, and its (b) phase-based stopping function (ϕ_{phase}), and (c) amplitude-based stopping function ($\phi_{amplitude}$)

novel stopping function was implemented using level sets. Implementation was performed in MATLAB. The discussion of the implementation process can be found in Appendix E.

4.1.4 Results

When the proposed segmentation algorithm is implemented, each pixel will be assigned three values, namely, *amplitude (i.e., I or image intensity), phase in the x direction (θ_x)* and *phase in the y direction (θ_y).* As explained in Subsection 4.1.3, the stopping function term $\phi_{amplitude}$ involves the gradient of the amplitude values, while the other term, ϕ_{phase}, consists of the square cosines of both phase values. Also, the parameter λ weights those two terms of the stopping function. For example, when λ

is equal to 0, the stopping function will only consist of the amplitude-based term[4]. On the other hand, in the case of λ being equal to 1, the novel phase-based term totaly makes up the stopping function. As will be shown in the following, there may be some situations where neither "$\lambda = 0$" nor "$\lambda = 1$" works, in which cases any other value between 0 and 1 needs to be chosen for λ. Basically, there are five boundaries, namely, inner & outer adventitia, inner & outer intima and fat (very outer boundary) to be detected in three coronary vessel wall ultrasound images formed at 30 mmHg, 60 mmHg and 90 mmHg. Of five boundaries, in clinical research, inner & outer adventitia and inner & outer intima are of principal concern.

For the purposes of this study, to see whether or not the appropriate λ value is same for each of those five boundaries in a given image[5], the detection of each boundary was done separately. In each of the following figures that shows the contour evolution for one of the boundaries, the initial contour was selected to be quarter circle for the sake of simplicity. Since the images were formed by manually putting together the RF lines that align in the radial direction, the azimuth angles of the first (i.e., very left) and last (i.e., very right) RF lines placed in those images are already known. So, for the sake of display, in all of the following figures, the relevant part of the contour (i.e., inside the area bounded by the first and last RF lines) is shown. Also, in all figures, upper left image shows the initial situation. Then, in every 300 iterations the condition of the contour is shown in the next image. The contour evolution can be tracked by moving from left to right and then from up to down. The bottom right image or if it is not available the bottom left one shows the situation when the contour no longer moves. Images are evaluated visually to determine whether or not the contour is able to detect the boundary.

[4]This case corresponds to the classical geodesic active contour model, where Eq. 6 involving the gradient of image intensities is used as a stopping function.

[5]As will be seen, it has turned out that there is no common λ value working for all boundaries of an image.

4.1.4.1 Segmentation Results of the Coronary Vessel Wall Ultrasound Image at 30 mmHg:

As far as the inner adventitia of the 30 mmHg image is concerned, first λ was chosen to be 0. The evolution of the contour for this case is shown in Figure 15. As can be seen clearly, the contour was not able to detect the boundary accurately. Because of the noise present inside the media, some parts of the contour stopped before reaching the boundary. This situation is resulted from the fact that the curve evolves under the influence of two derivatives[6] when only $\phi_{amplitude}$ (the classical stopping function given in Eq. 6) is used.

Second, λ was set to 1 where only phase-based term is effective. The results given in Figure 16 show that the contour did not get stuck before reaching the boundary as did in "$\lambda = 0$" case. This is resulted from the fact that ϕ_{phase} given in Eq. 8 does not include any gradient term, providing the contour evolution to be influenced only by one derivative. In this case, however, some parts of the contour passed through the boundary and stopped somewhere between the outer adventitia and inner adventitia. This situation results from the weakening of the stopping power. For "$\lambda = 0$" case, $\nabla\phi$ in the transport term of Eq. 7 looks like a "doublet" near an edge due to involving two derivatives of the image. One of its main effects is to push the contour back if it passes through the edge; so, it functions as an extra stopping power [96]. Since in "$\lambda = 1$" case $\nabla\phi$ includes only one derivative, the extra stopping power of the model is weakened, causing the contour to pass the edge. In other words, that ϕ_{phase} does not involve any derivative provides the contour to reach the boundary while at the same time hindering its stop at the boundary.

[6] As explained in Subsection 4.1.3, level set equation involves the derivative of the stopping function that includes, in its classical form, the derivative of the image.

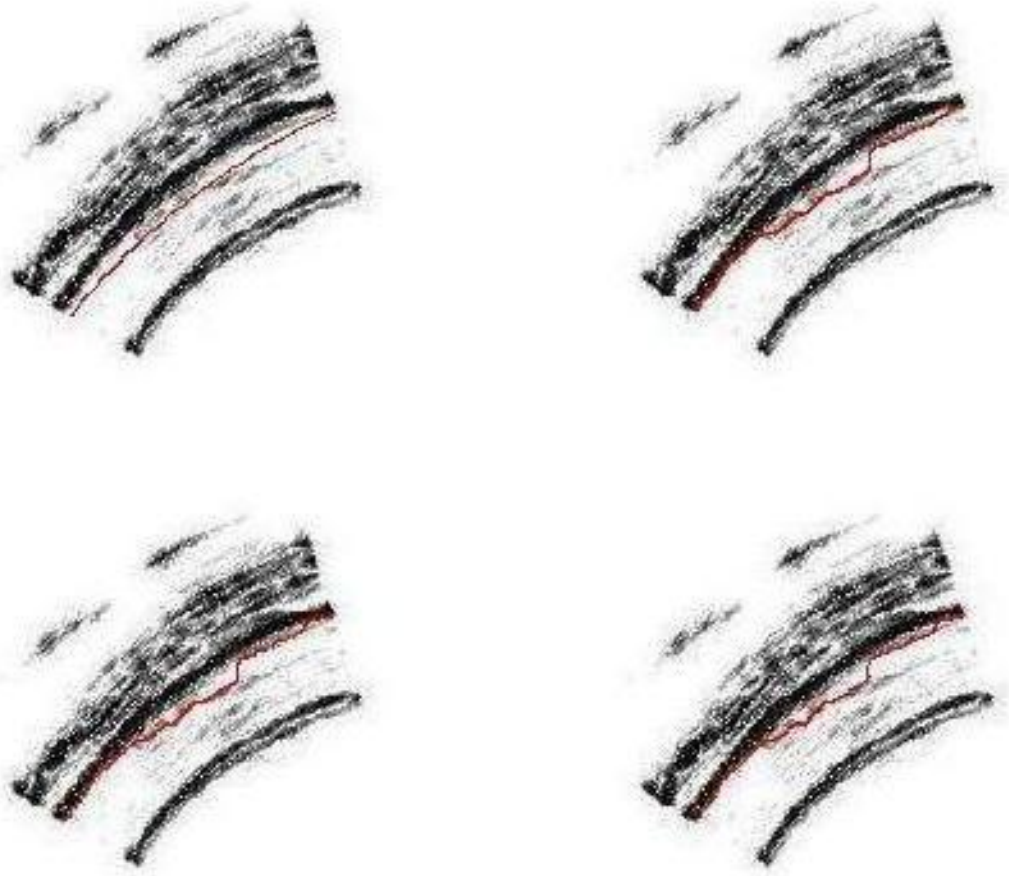

Figure 15: Detection of inner adventitia at 30 mmHg for $\lambda = 0$

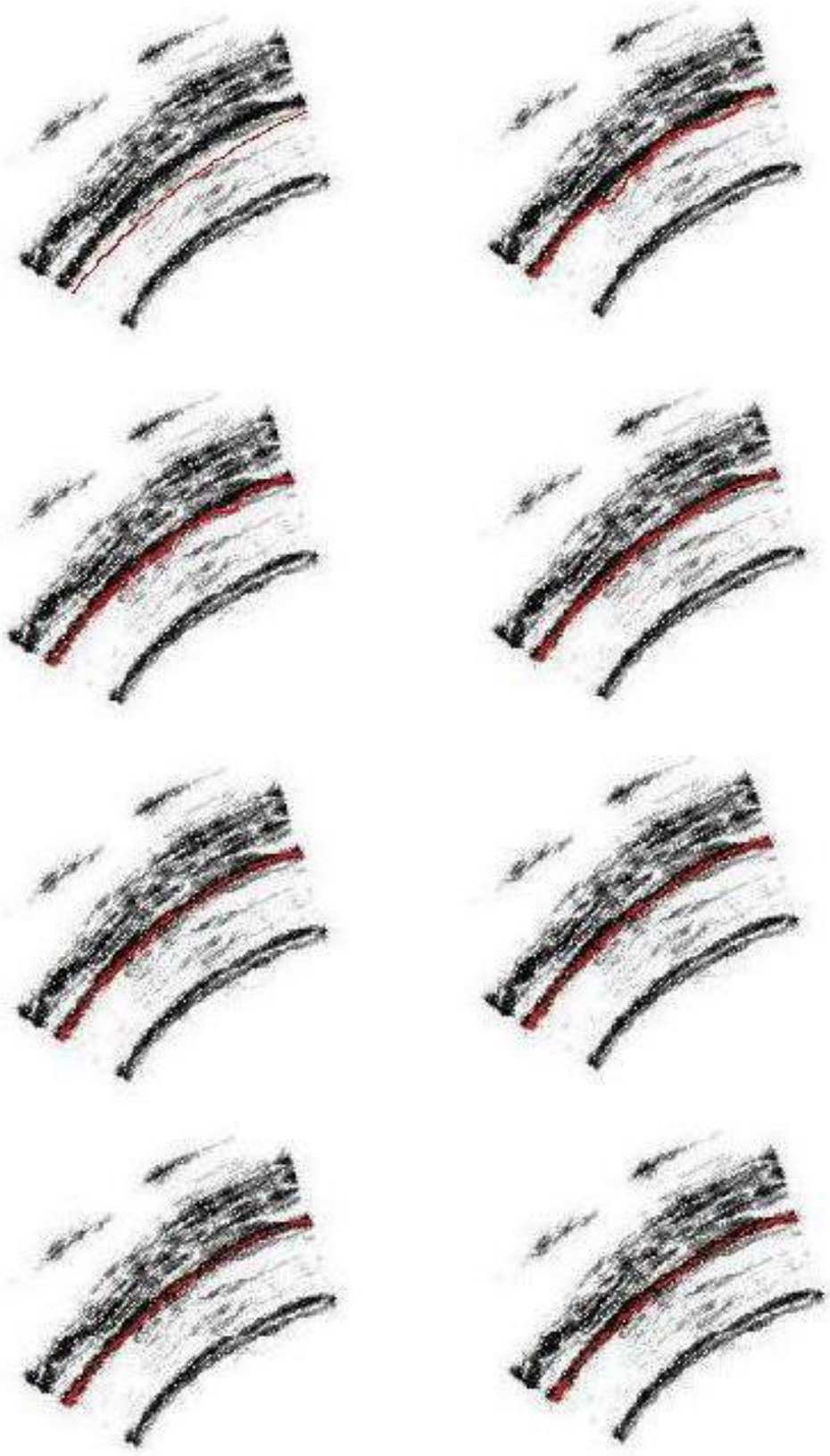

Figure 16: Detection of inner adventitia at 30 mmHg for $\lambda = 1$

Since neither "$\lambda = 1$" nor "$\lambda = 0$" case worked here, a value between 0 and 1, specifically, 0.5, where the weights of phase and amplitude terms are equal, was chosen next. The results in Figure 17 show that the contour was almost able to reach the boundary; however, there are still a few parts that got stuck inside the media. This implies that the weight of the phase-based stopping term needs to be increased. The results with $\lambda = 0.7$ are given in Figure 18. As can be seen visually, the inner adventitia was detected accurately with λ being equal to 0.7.

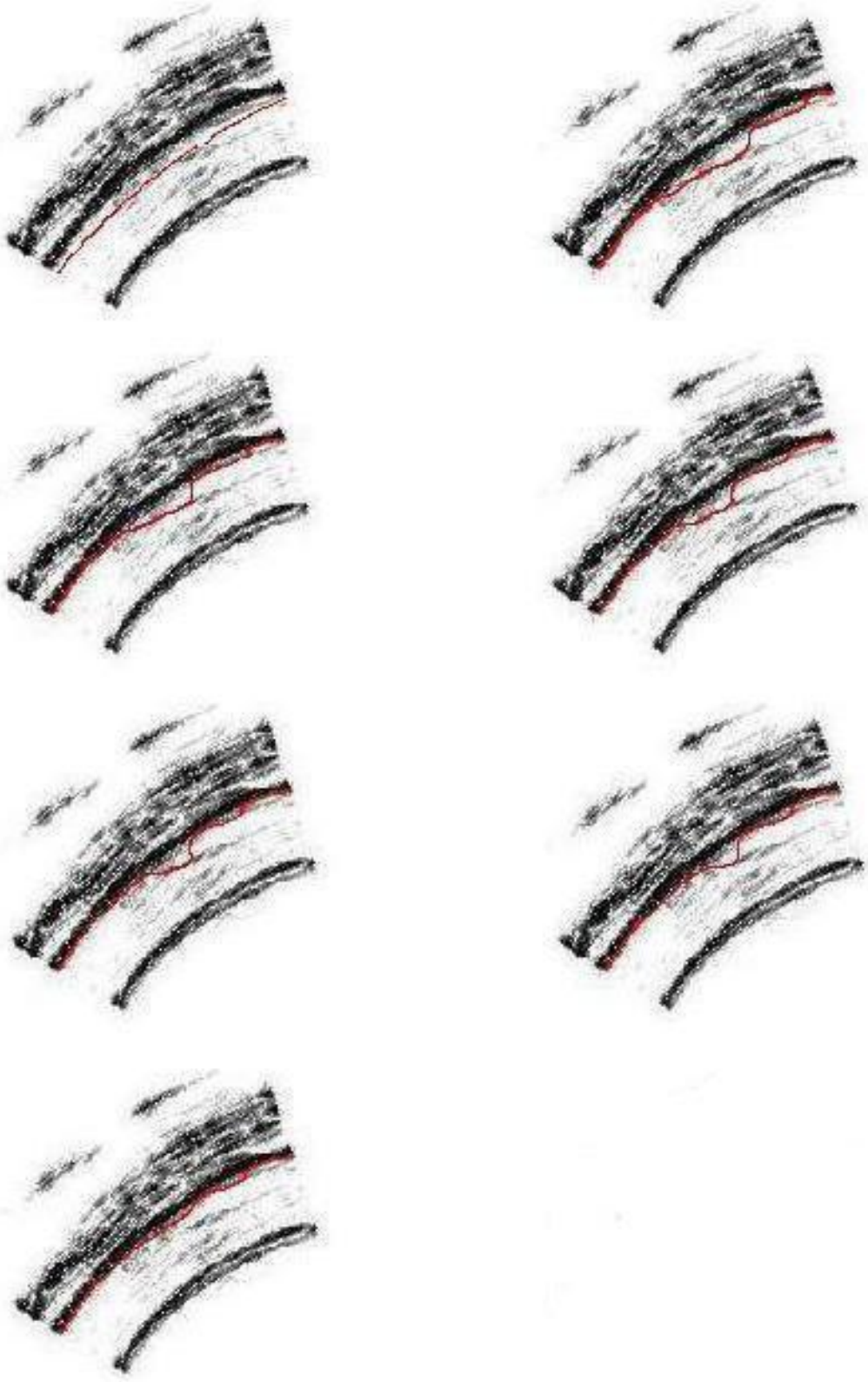

Figure 17: Detection of inner adventitia at 30 mmHg for $\lambda = 0.5$

Figure 18: Detection of inner adventitia at 30 mmHg for $\lambda = 0.7$

For the outer adventitia, first, λ was chosen to be 1. However, the contour passed through the boundary as can be seen in Figure 19. Then, λ was set to 0.5. From the results given in Figure 20, it can be visualized that the outer adventitia was able to be located.

As far as the detection of the outer intima is concerned, λ was initially chosen to be 0.7, because it was already known that the appropriate λ value for the inner adventitia was 0.7, and the noise characteristics of the upper and lower part of the media where contours were being evolved to detect the inner adventitia and outer intima, respectively, were fairly similar. The results given in Figure 21 shows that the contour was indeed able to find the boundary accurately.

To detect the inner intima, first of all, "$\lambda = 0$" case was examined, because the area between the center of the artery and the inner intima has less amount of noise than the other parts of the image have. The results of this case are given in Figure 22. It can be seen visually that the contour did not stop before reaching the boundary as did in the previous "$\lambda = 0$" cases, and so the inner intima was able to be detected. Finally, the detection of the very outer boundary (fat) was performed. Since there was a significant amount of artifact where the curve would evolve, only "$\lambda = 1$" case was implemented to roughly estimate the outer boundary of the fat (see Figure 23).

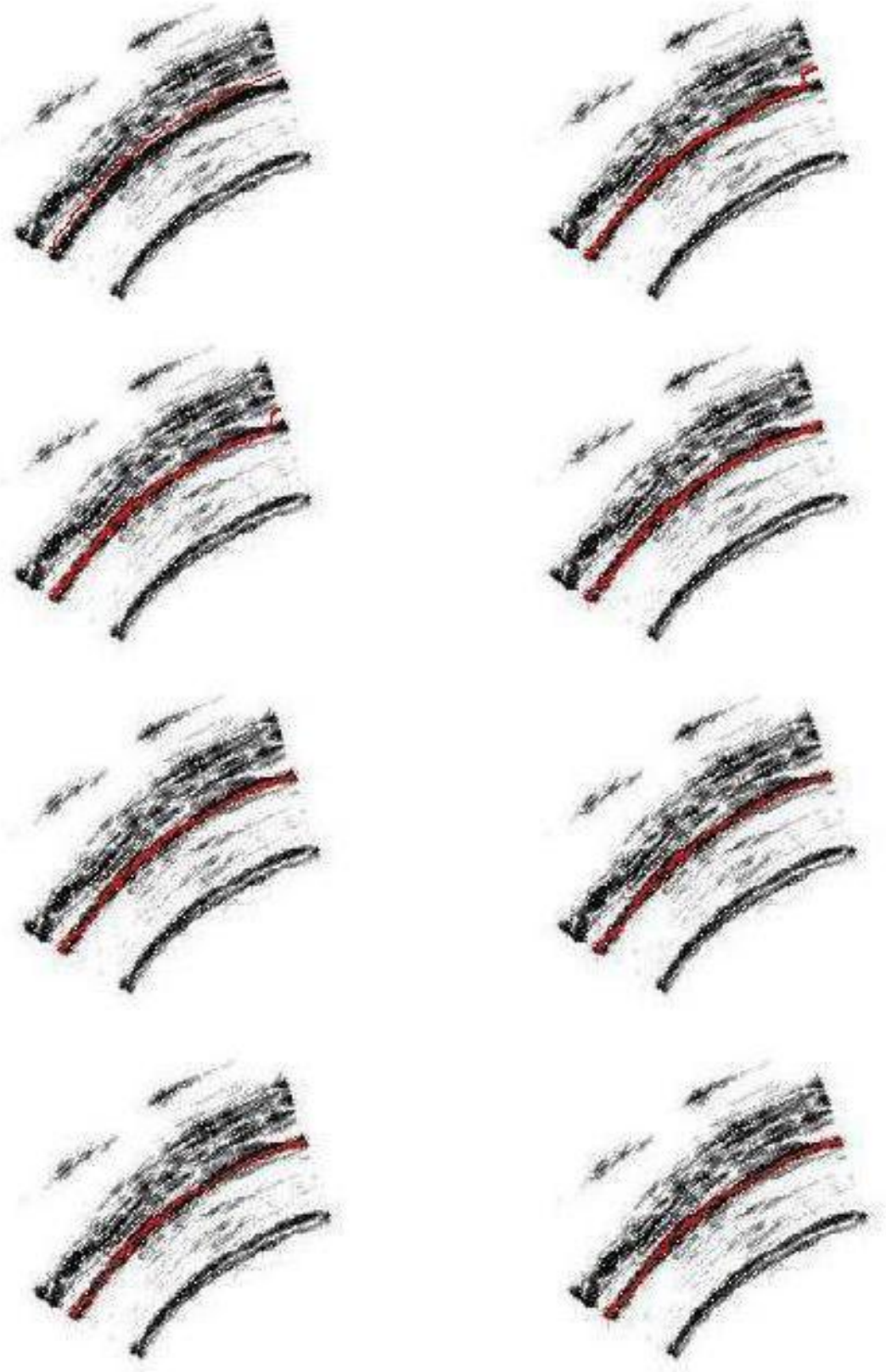

Figure 19: Detection of outer adventitia at 30 mmHg for $\lambda = 1$

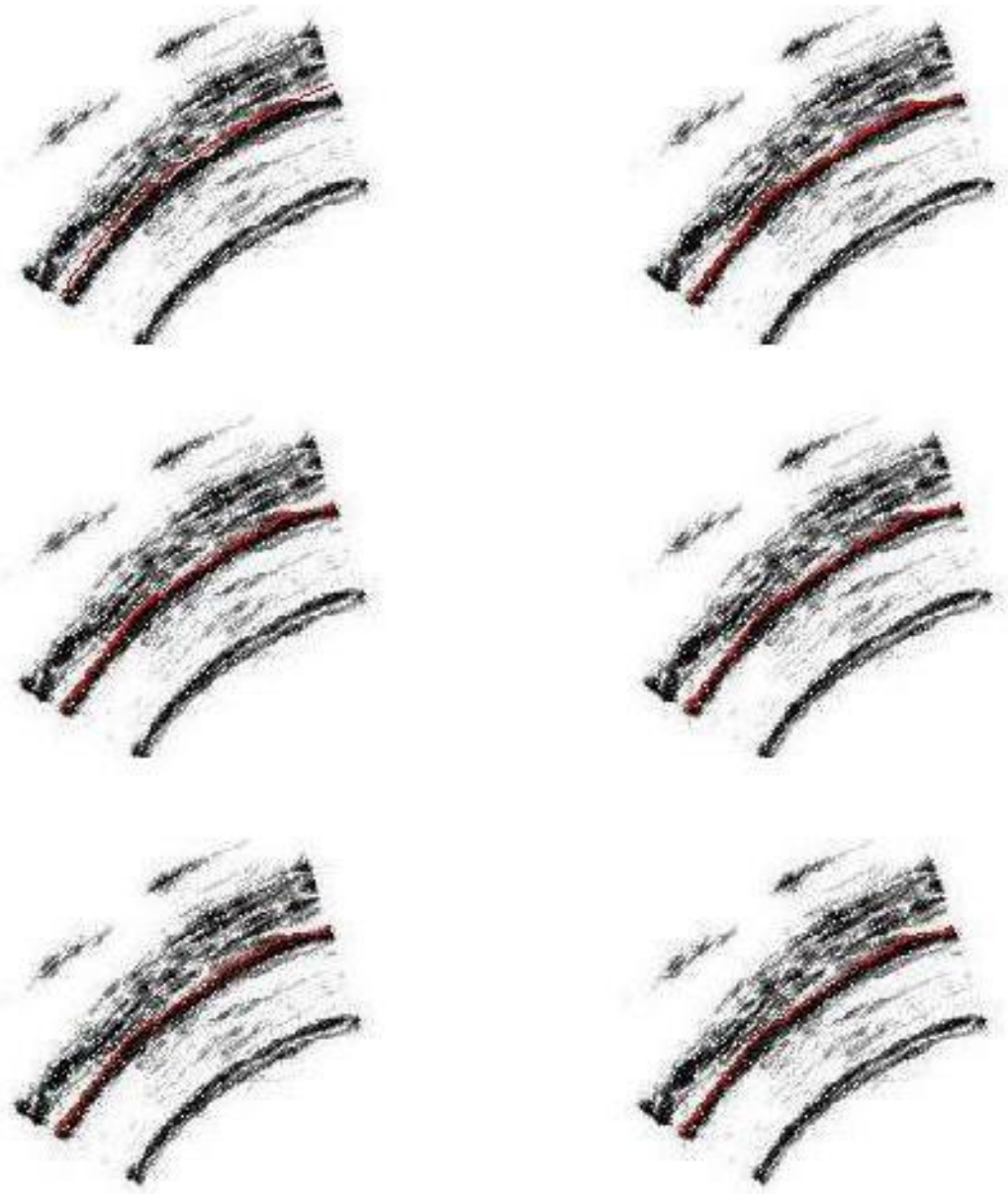

Figure 20: Detection of outer adventitia at 30 mmHg for $\lambda = 0.5$

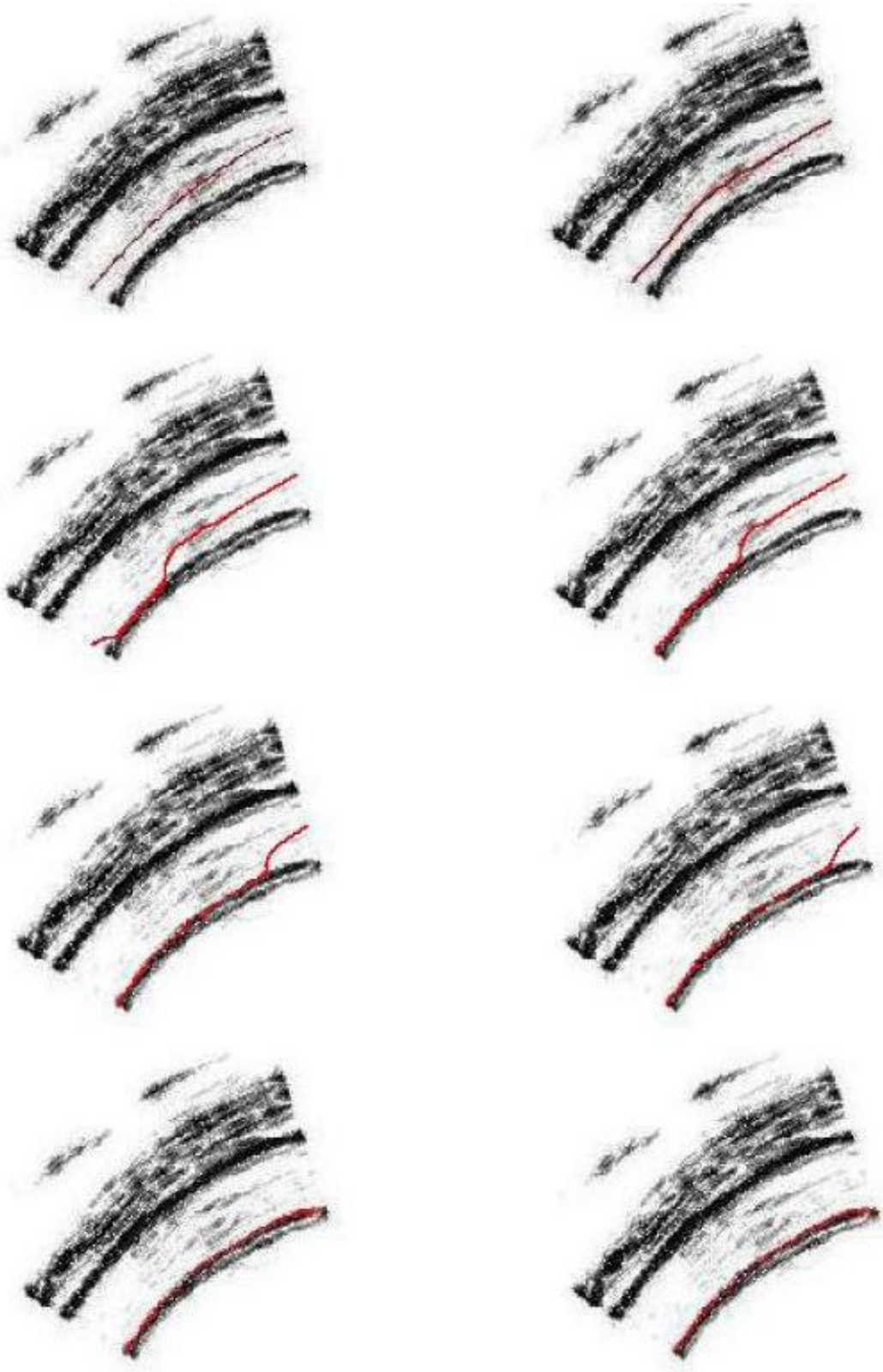

Figure 21: Detection of outer intima at 30 mmHg for $\lambda = 0.7$

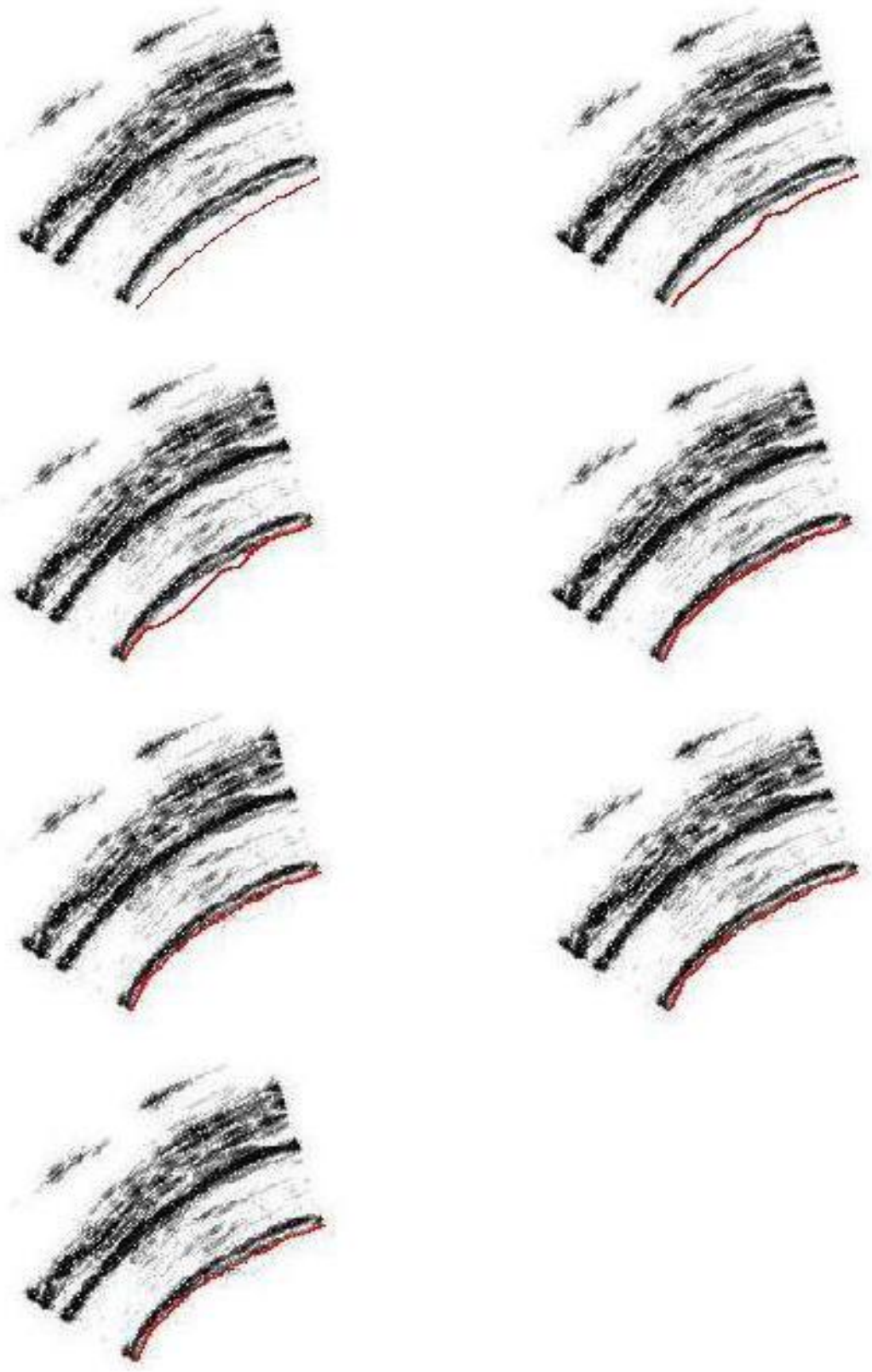

Figure 22: Detection of inner intima at 30 mmHg for $\lambda = 0$

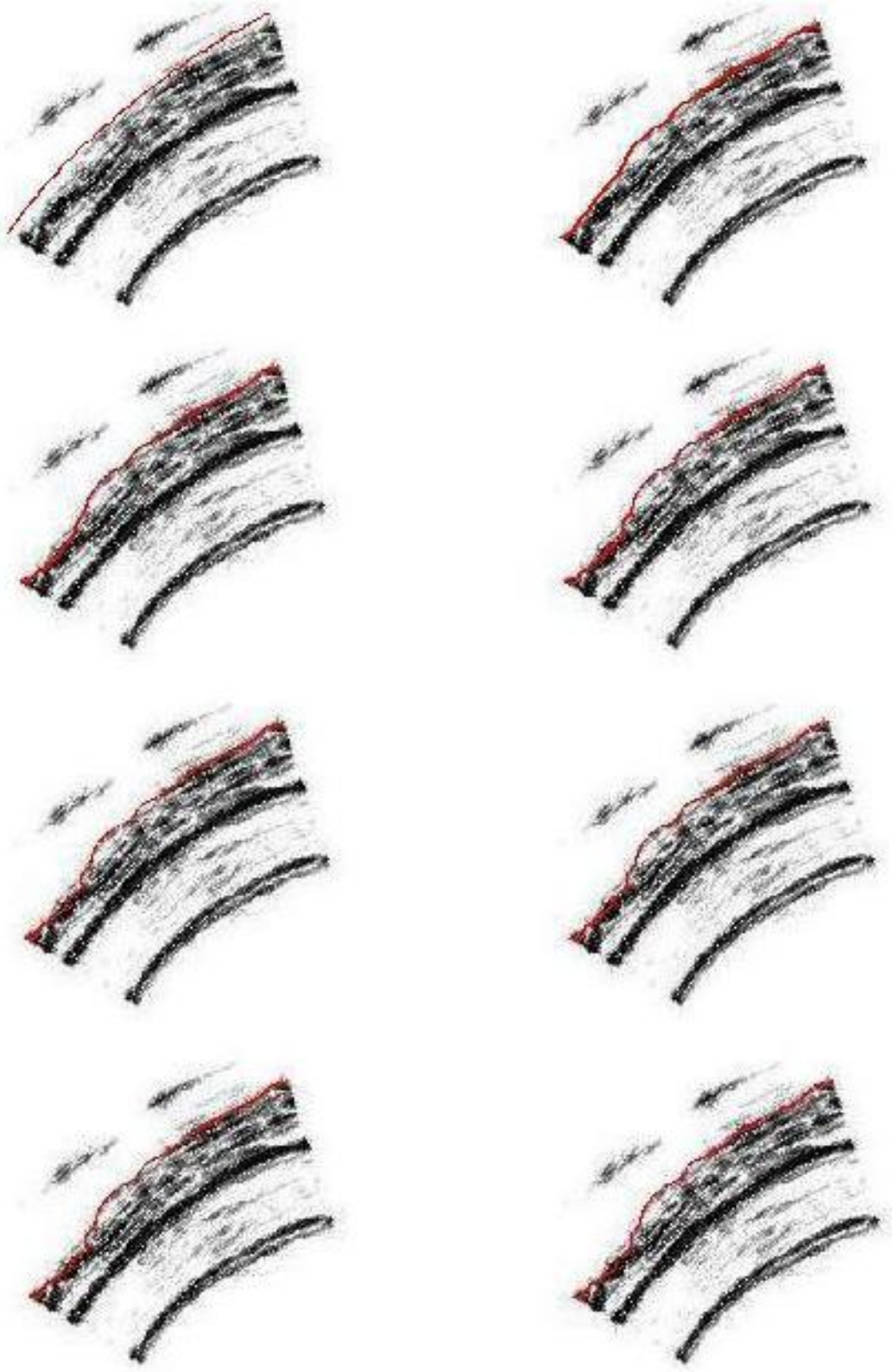

Figure 23: Detection of fat at 30 mmHg for $\lambda = 1$

4.1.4.2 Segmentation Results of the Coronary Vessel Wall Ultrasound Image at 60 mmHg:

After the boundaries of the 30 mmHg image were detected, the next step was to segment the 60 mmHg image. For the outer intima, first, λ was set to 0. As can be seen in Figure 24, some part of the contour stopped evolving before reaching the boundary. This happened, as explained before, due to the classical active contour technique's vulnerability to the noise (i.e., $\nabla\phi$ involves two derivatives of the image when $\phi = \phi_{amplitude}$). When the value of λ was increased to 0.5 so that ϕ_{phase} would have an impact on the evolution of the contour, the outer intima was able to be detected accurately (see Figure 25).

For the detection of the inner adventitia, the results of "$\lambda = 1$" case were given in Figure 26. Since the contour was not able to stop at the boundary but passed through it, "$\lambda = 0.6$" case was also examined. As can be observed in Figure 27, the boundary was accurately detected in this case. As far as the detection of the inner intima is concerned, λ was set to 0 as done in the 30 mmHg image. Since the area between the center of the artery and the inner intima is almost noise-free, the contour did not get stuck anywhere and was able to locate the boundary (see Figure 28). The segmentation result of the outer adventitia for λ being equal to 0.4 is given in Figure 29, which shows a success in detecting the boundary. Finally, in Figure 30, fat boundary is located. Since there is a significant amount of artifact in the upper part of the image, λ was set to 1 to detect this boundary.

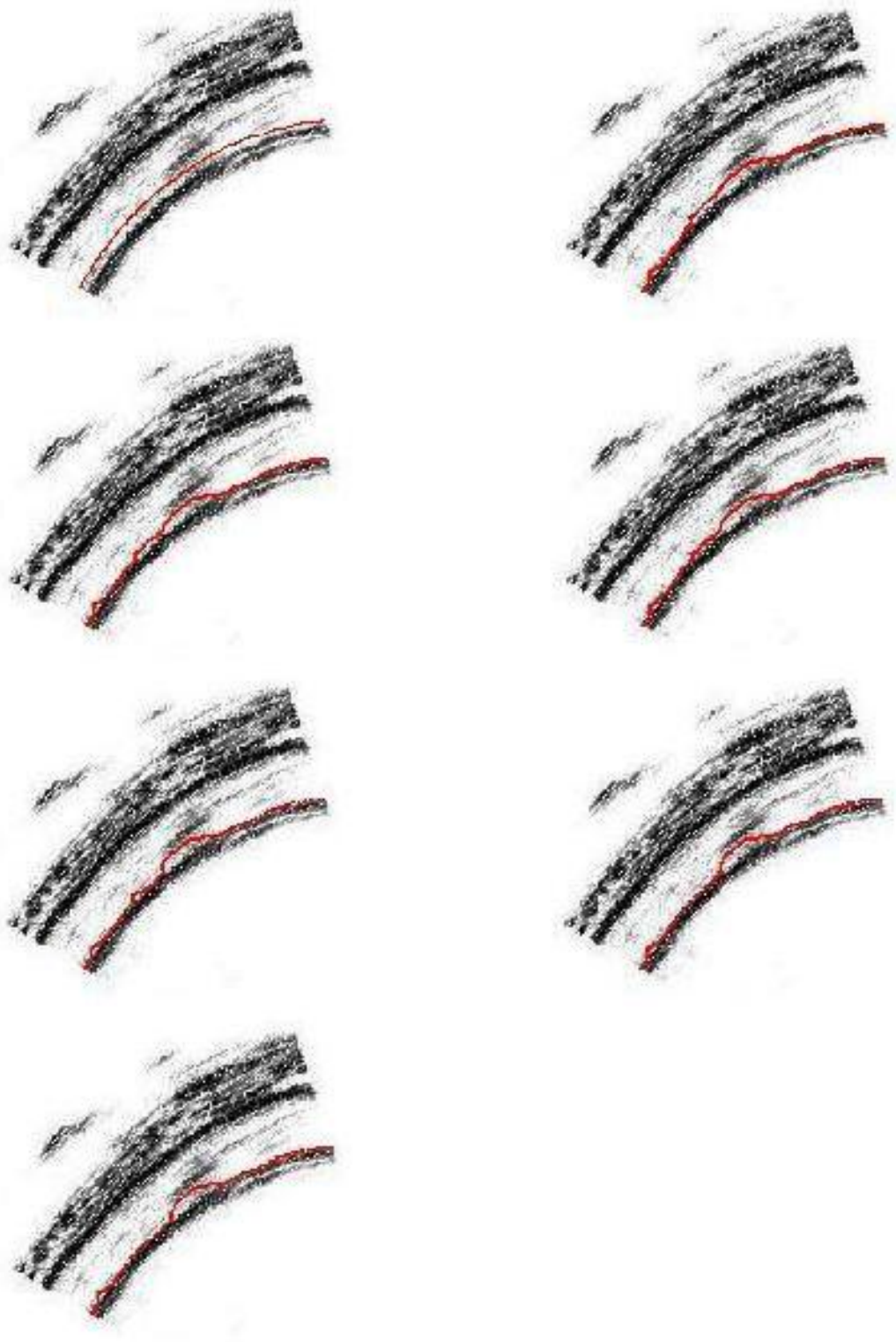

Figure 24: Detection of outer intima at 60 mmHg for $\lambda = 0$

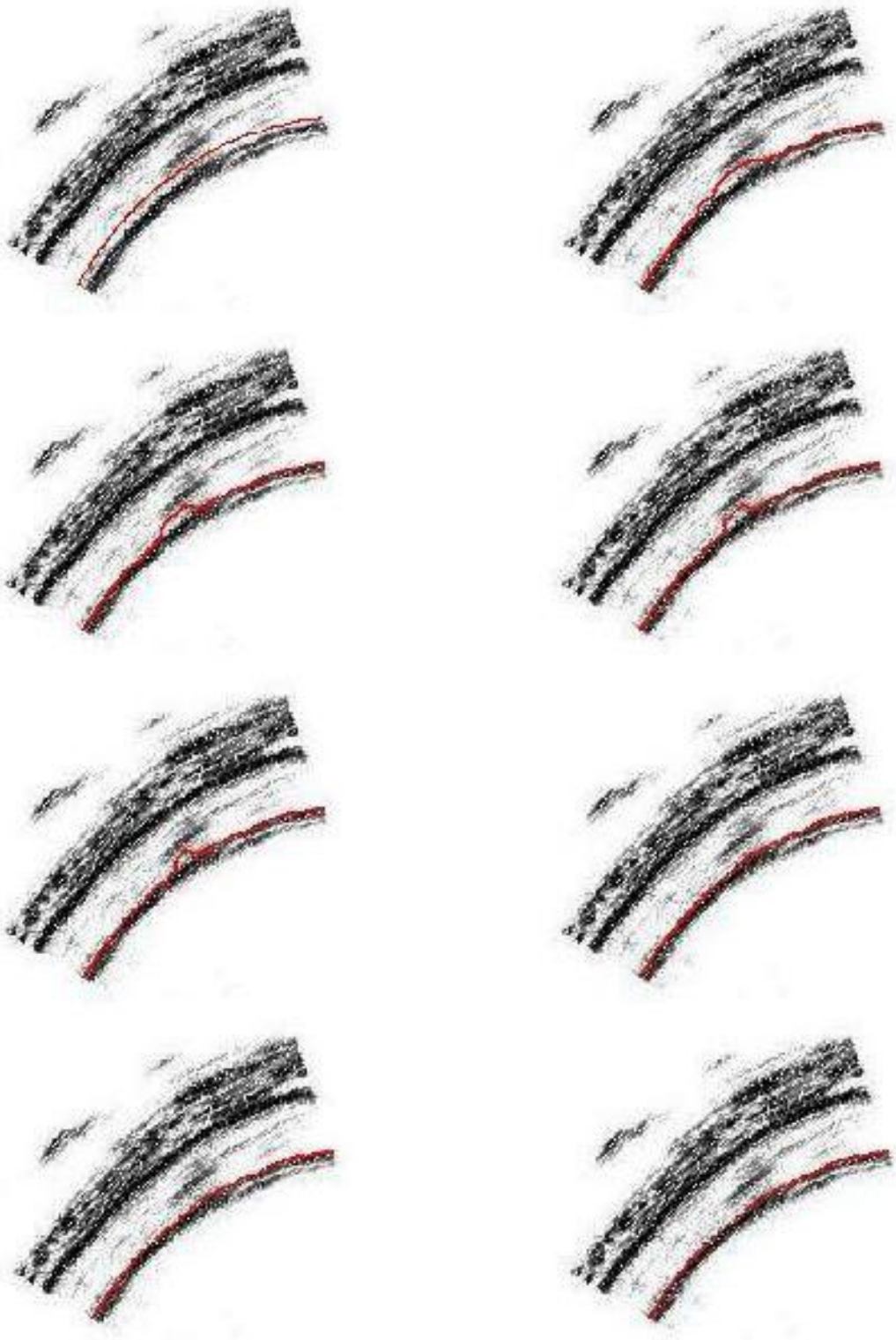

Figure 25: Detection of outer intima at 60 mmHg for $\lambda = 0.5$

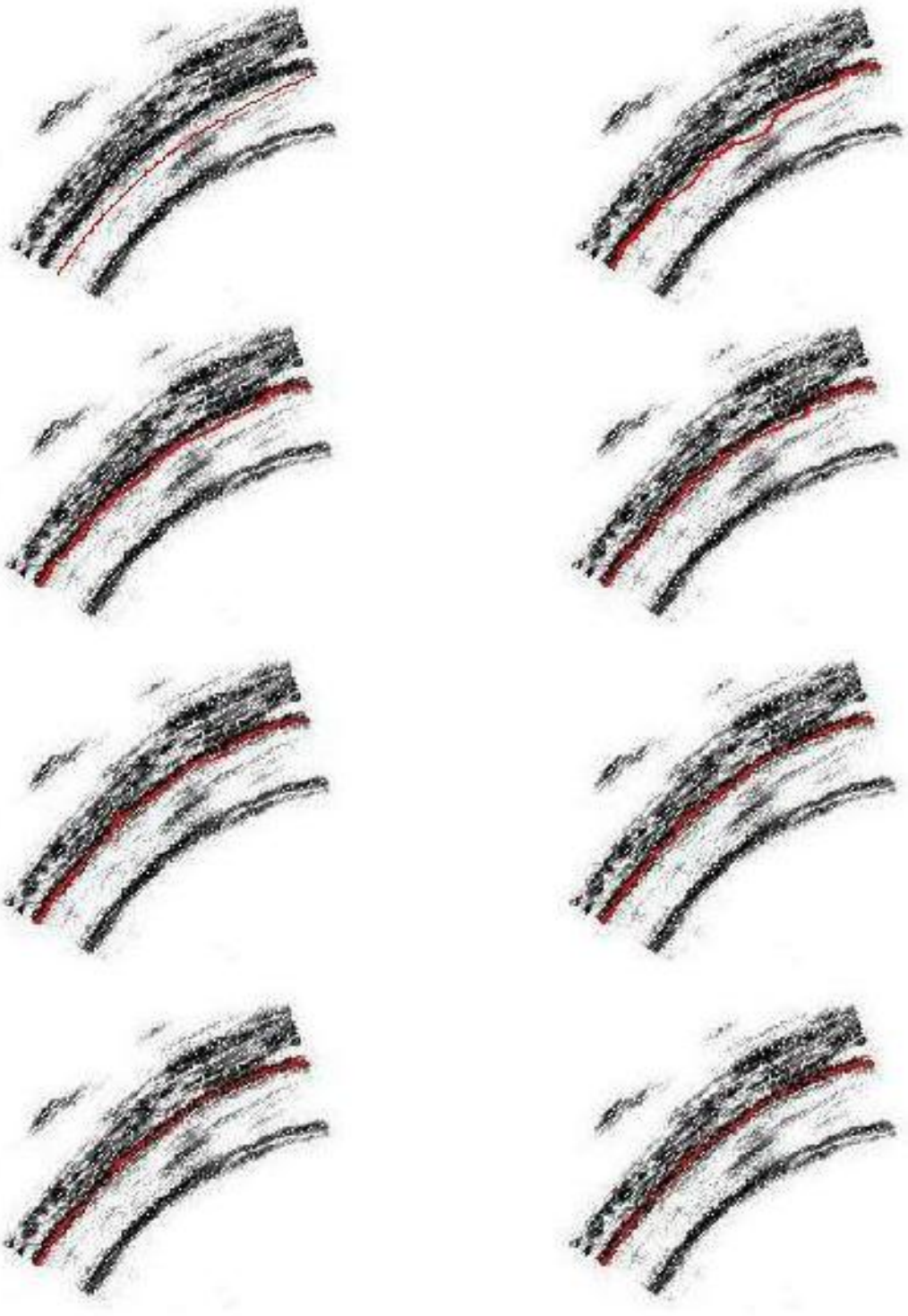

Figure 26: Detection of inner adventitia at 60 mmHg for $\lambda = 1$

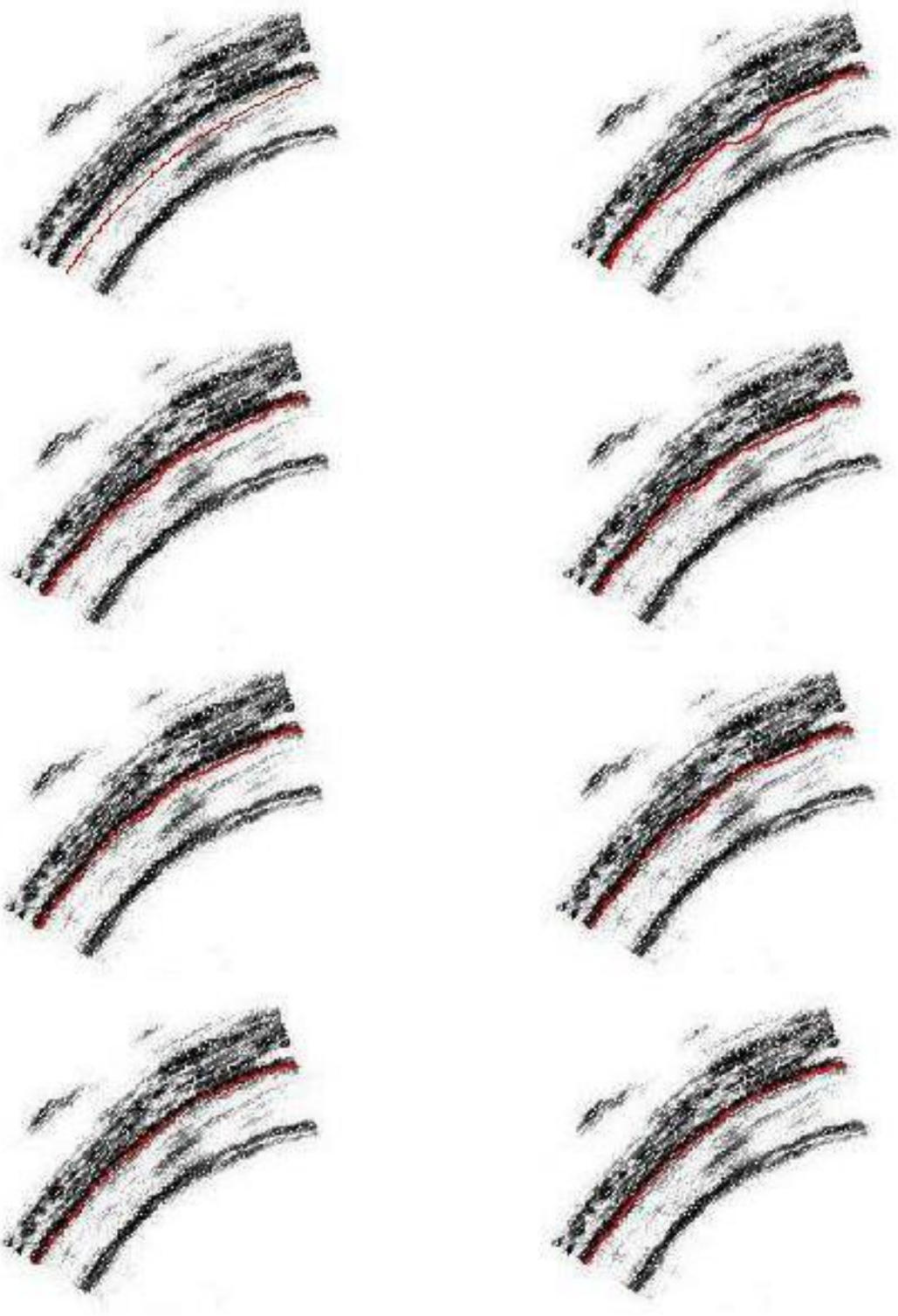

Figure 27: Detection of inner adventitia at 60 mmHg for $\lambda = 0.6$

Figure 28: Detection of inner intima at 60 mmHg for $\lambda = 0$

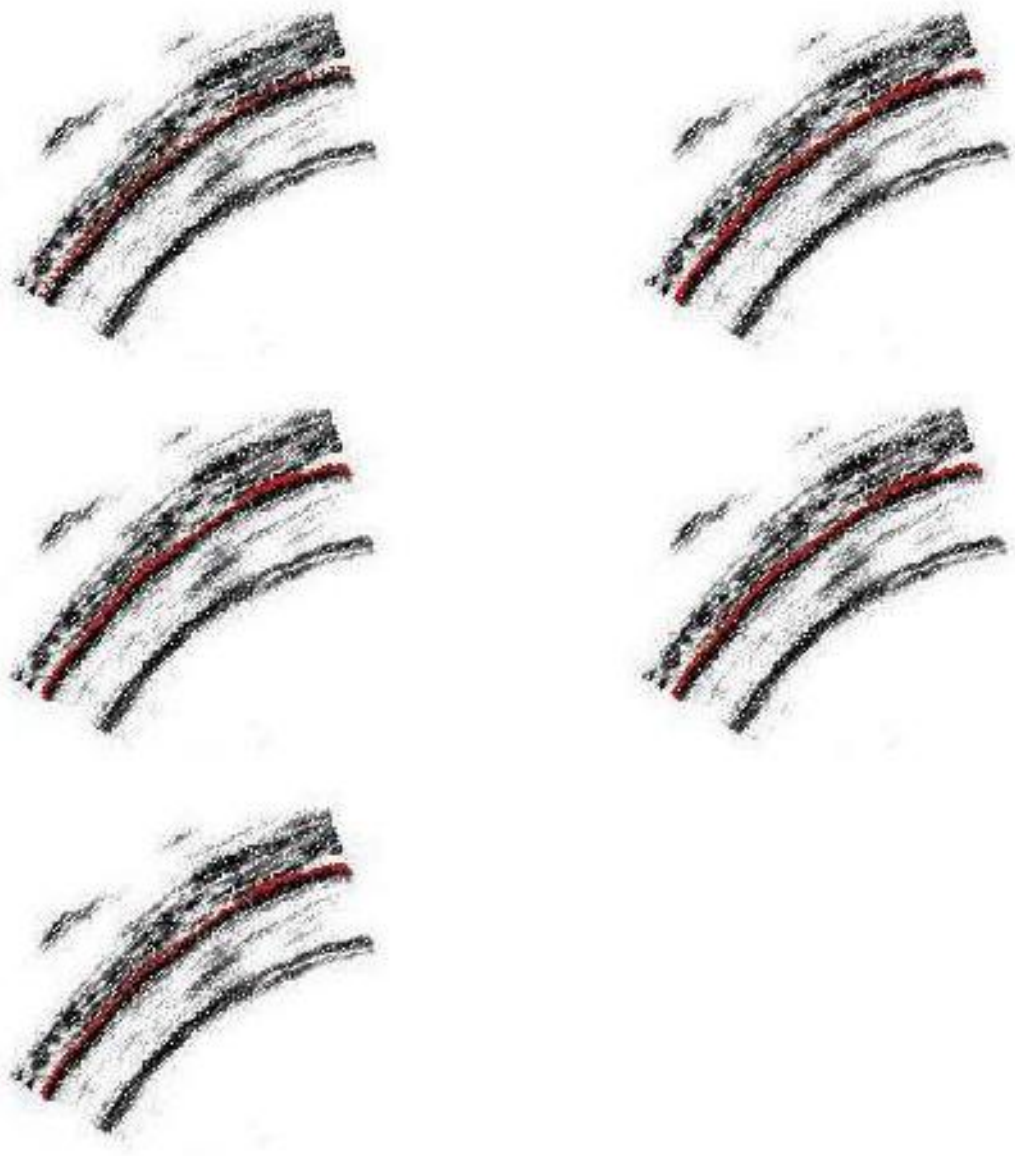

Figure 29: Detection of outer adventitia at 60 mmHg for $\lambda = 0.4$

Figure 30: Detection of fat at 60 mmHg for $\lambda = 1$

4.1.4.3 Segmentation Results of the Coronary Vessel Wall Ultrasound Image at 90 mmHg:

After the 30 mmHg and 60 mmHg images were segmented, the final step was to determine the boundaries of the 90 mmHg image. Having started with the detection of the inner adventitia, λ was first set to 0. Due to the noise present inside the media and the high noise-sensitivity of $\phi_{amplitude}$, contour wasn't able to completely reach the inner adventitia (see Figure 31). The results of the curve evolution with λ equal to 0.5 are given in Figure 32. It can be seen that the contour was able to locate the inner adventitia boundary in this case.

To detect the outer intima, λ was initially chosen to be 0.2 instead of 0, because it was known from the detection of the inner adventitia that the noise present inside the media had a negative impact on the curve evolution, implying that "$\lambda = 0$" case also would not work for the outer intima. Indeed, as can be seen in Figure 33, "$\lambda = 0.2$" case did not work, either. In other words, 20% weight given to ϕ_{phase} didn't turn out to be enough to make the contour reach the boundary completely. Thus, λ was increased to 0.7. The results given in Figure 34, however, show that the contour couldn't stop completely at the outer intima in this case. Since 70% weight turned out to be too high for ϕ_{phase}, λ was then chosen to be 0.4. As can be seen visually in Figure 35, the outer intima was able to be detected accurately with λ being equal to 0.4[7]. As far as the outer adventitia and inner intima are concerned, as can be seen in Figures 36 and 37, "$\lambda = 0.2$" and "$\lambda = 0$", respectively, have provided both boundaries to be detected accurately. Finally, the outer boundary of fat was able to be detected with λ being equal to 1 as can be visualized in Figure 38.

[7]It may seem that the contour couldn't locate the very left part of the boundary; however, actually this is not the case. As can be seen in the first (upper left) image, there is a boundary, though weak, where the contour stops.

Figure 31: Detection of inner adventitia at 90 mmHg for $\lambda = 0$

Figure 32: Detection of inner adventitia at 90 mmHg for $\lambda = 0.5$

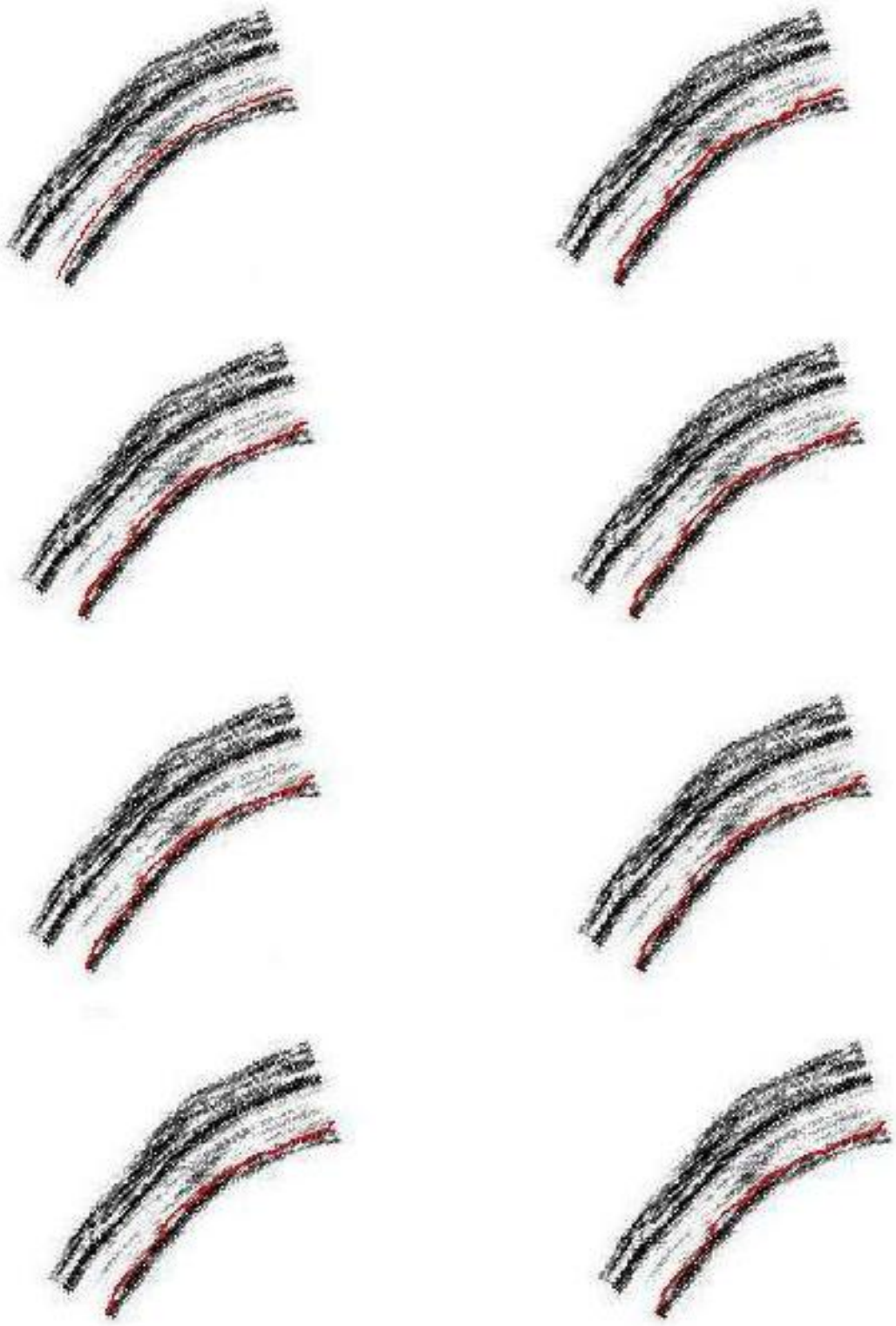

Figure 33: Detection of outer intima at 90 mmHg for $\lambda = 0.2$

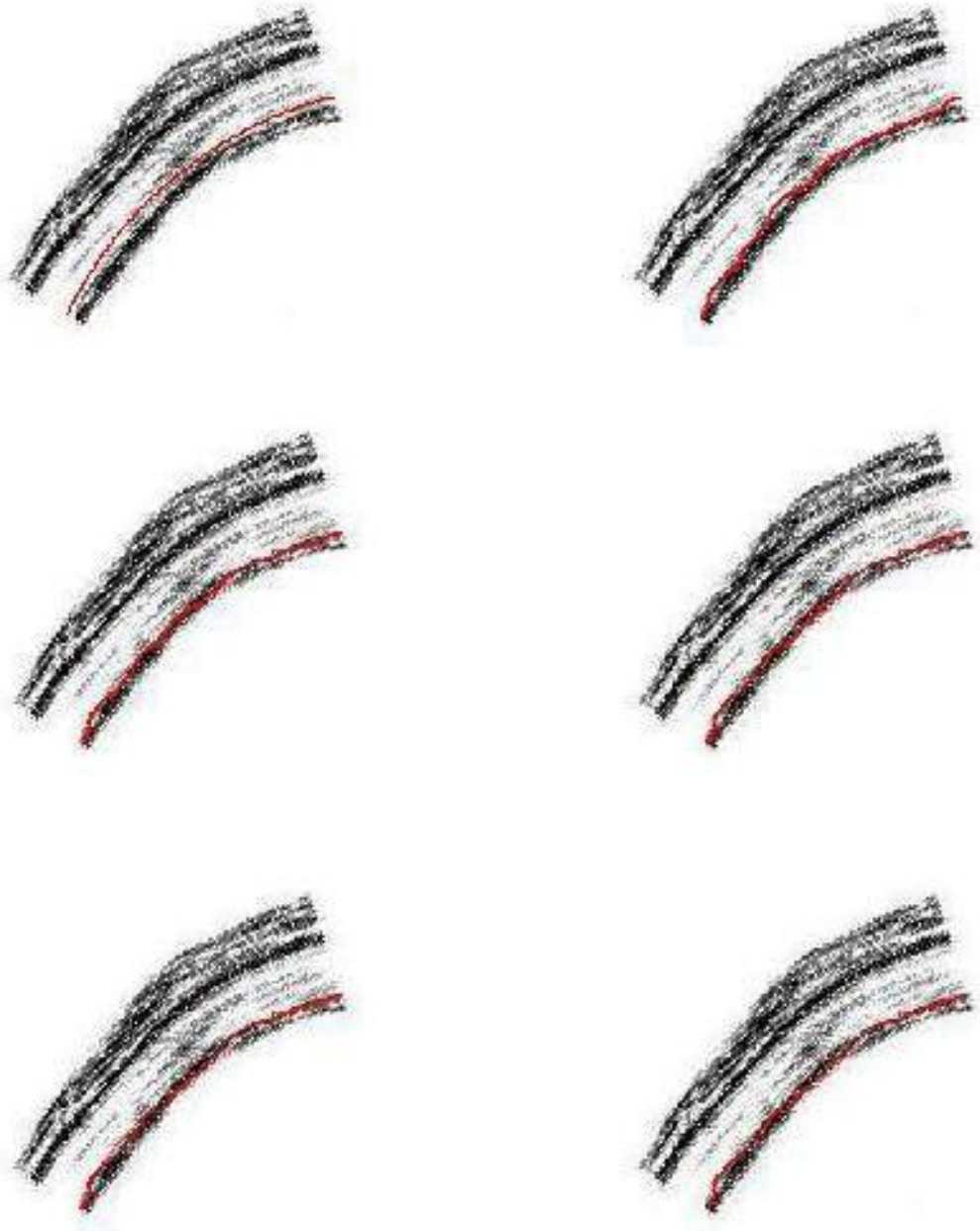

Figure 34: Detection of outer intima at 90 mmHg for $\lambda = 0.7$

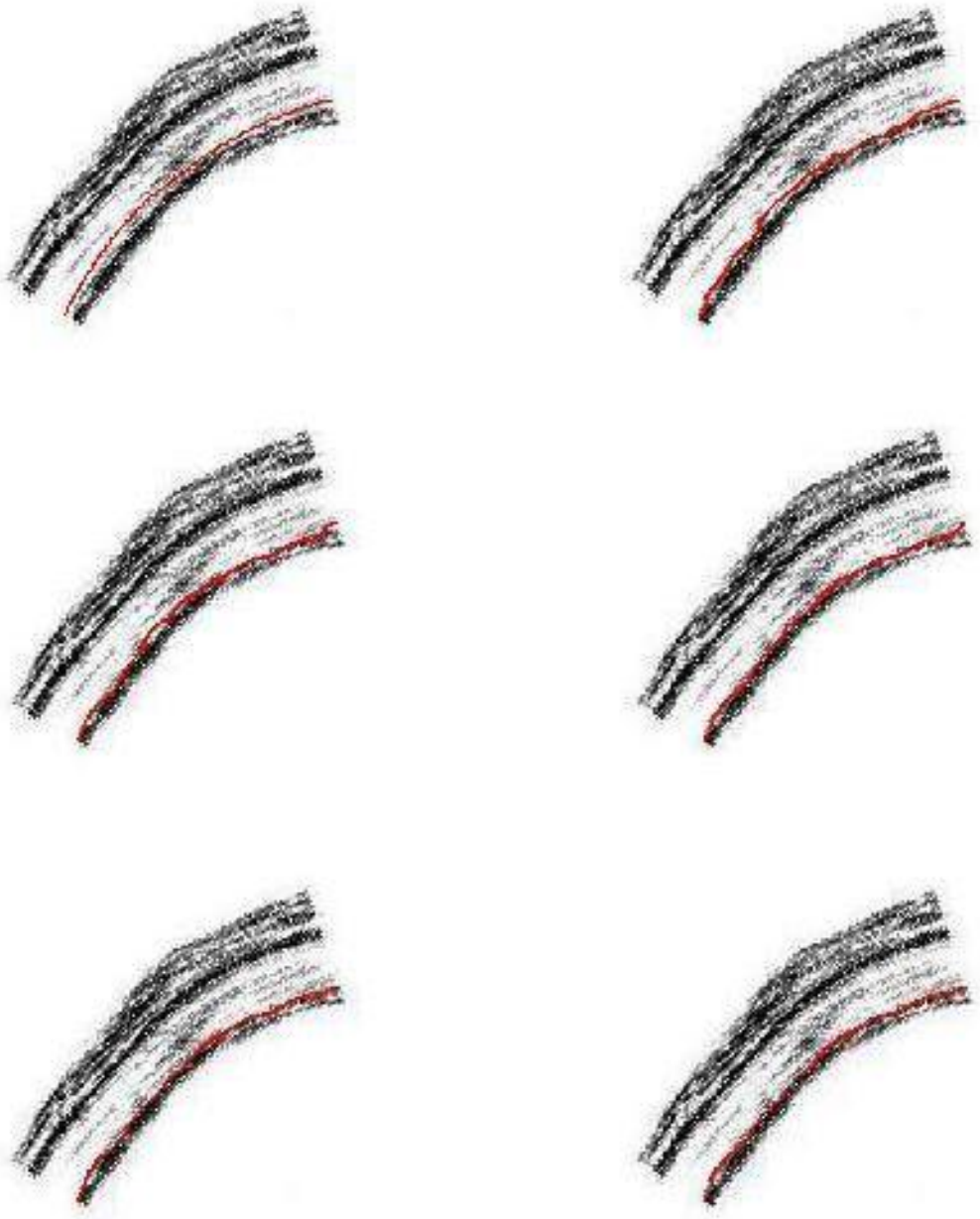

Figure 35: Detection of outer intima at 90 mmHg for $\lambda = 0.4$

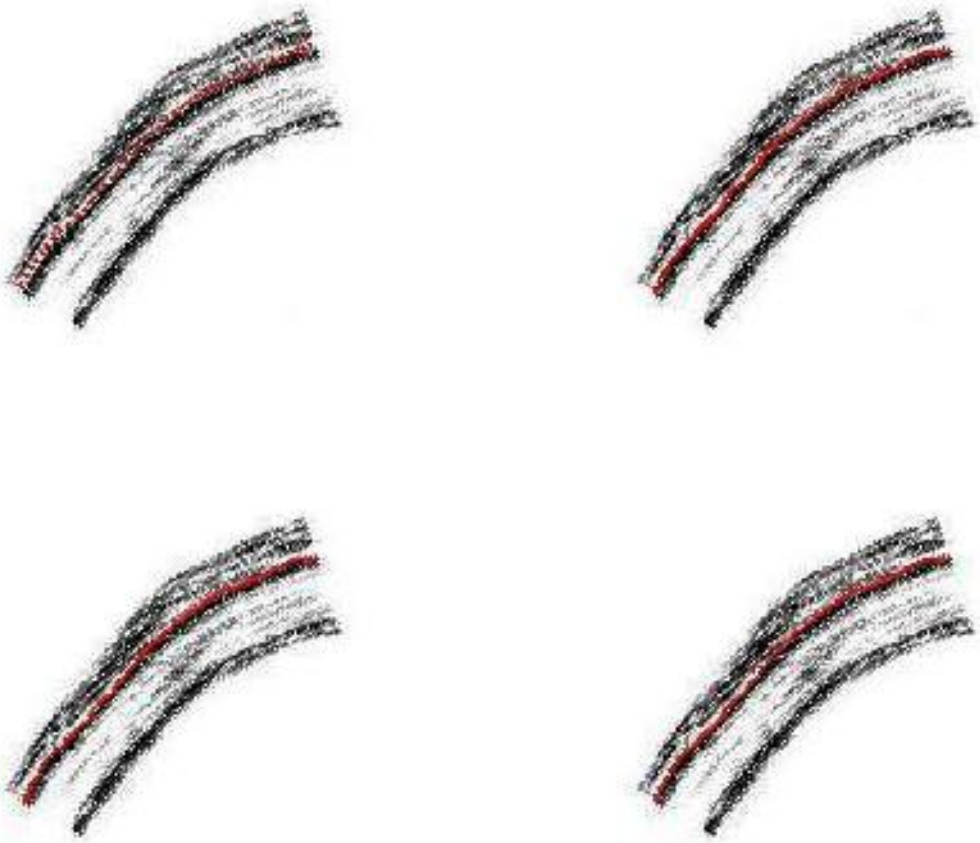

Figure 36: Detection of outer adventitia at 90 mmHg for $\lambda = 0.2$

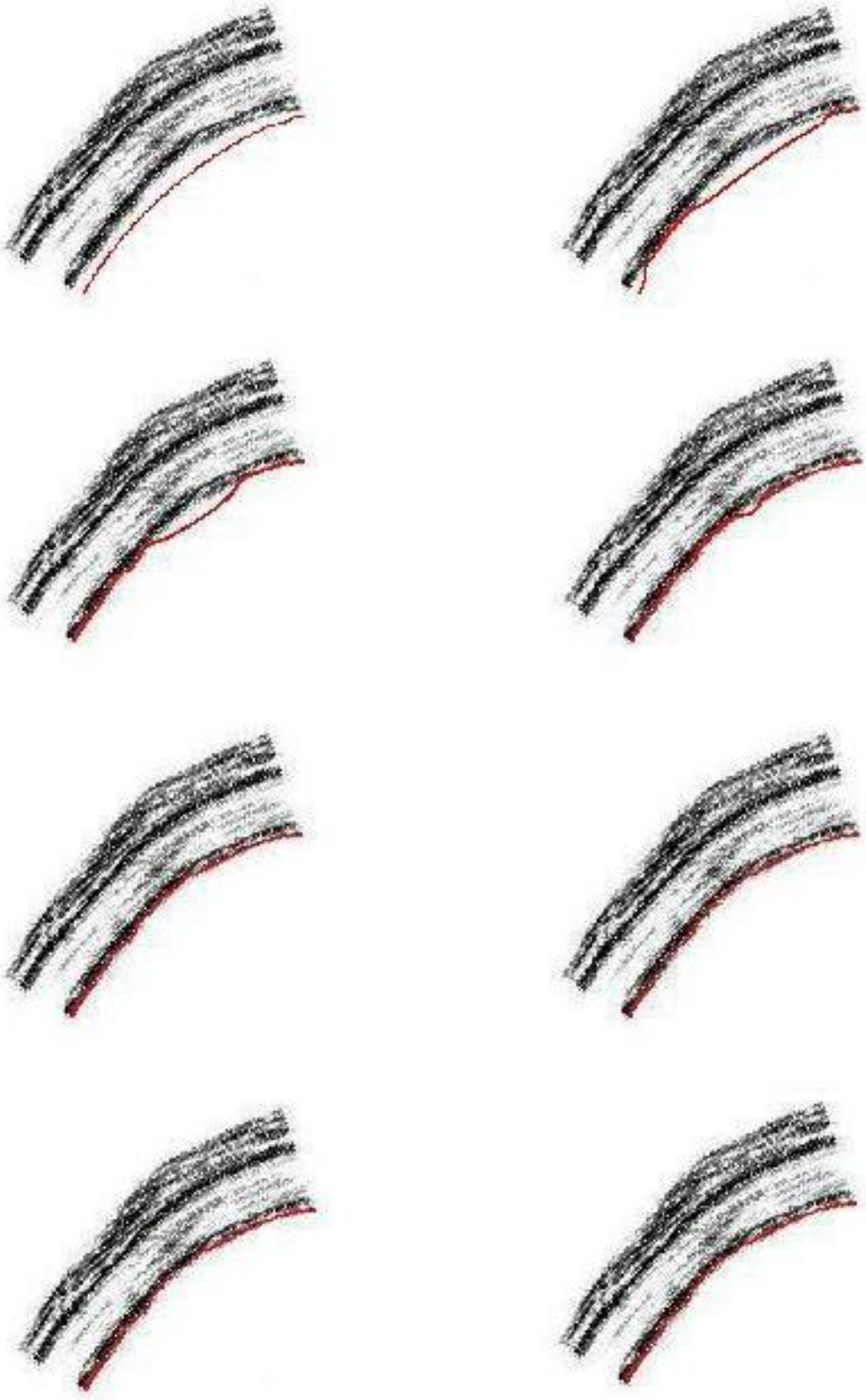

Figure 37: Detection of inner intima at 90 mmHg for $\lambda = 0$

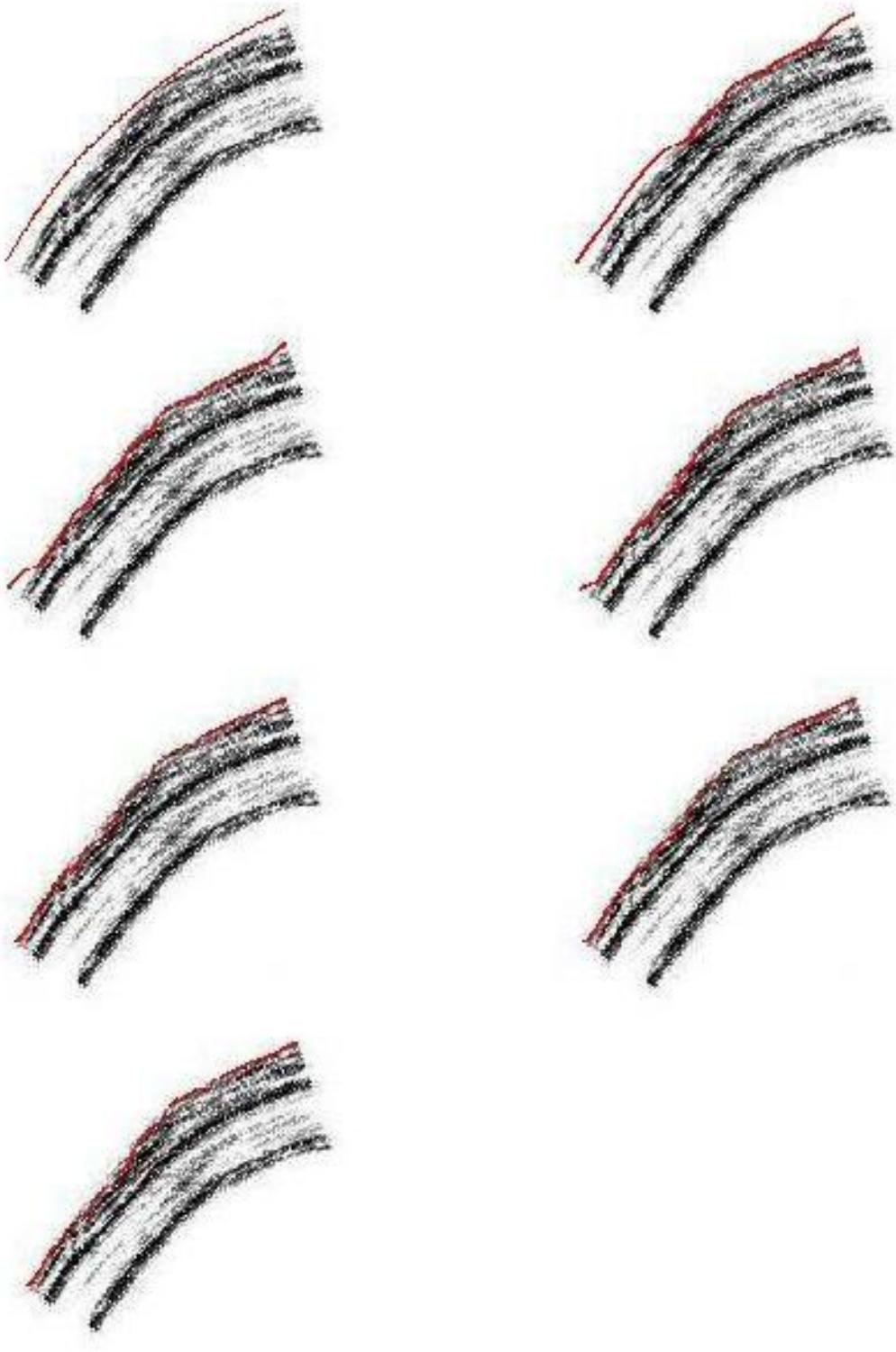

Figure 38: Detection of fat at 90 mmHg for $\lambda = 1$

4.1.5 Analysis

The obtained λ values that have provided accurate segmentation results in Subsection 4.1.4 are outlined in Table 1 for each boundary-pressure pair.

Table 1: Optimal λ values for the edge-based segmentation

	30 mmHg	60 mmHg	90 mmHg
Inner intima	0	0	0
Outer intima	0.7	0.5	0.4
Inner adventitia	0.7	0.6	0.5
Outer adventitia	0.5	0.4	0.2
Outer fat	1	1	1

Based on these results, the following arguments can be made:

- For a given high-resolution coronary vessel wall image, there is most likely no single λ value that provides all of the boundaries in the image to be detected accurately.

- The cases where ϕ_{phase} ($\lambda = 1$) or $\phi_{amplitude}$ ($\lambda = 0$) works by itself are rare. Specifically, in all three images $\phi_{amplitude}$ by itself has provided accurate results only for the inner intima (see Figures 22, 28, 37). This is resulted from the fact that the area between the center (i.e., right bottom corner) and inner intima involves the least amount of noise (almost noise-free). On the other hand, ϕ_{phase} by itself has provided fairly reliable results only in the detection of fat, which is a very thick layer (see Figures 23, 30, 38).

- For $\lambda = 0$, the curve is not able to completely reach the boundary unless the part of the image where it evolves is noise-free or has significantly low amount of noise (e.g., see Figures 15, 24, 31).

- For $\lambda = 1$, the curve never stops evolving before completely reaching the boundary; however, if the inner and outer boundaries of the corresponding layer are

close to each other (i.e., thickness of the layer is small as in intima and adventitia), the curve passes through the nearer boundary and stops somewhere inside the layer or even sometimes reaches the farther boundary and then stops its evolution (e.g., see Figures 16, 19, 26).

- In the detection of the outer intima, inner adventitia and outer adventitia (for all pressures), with λ equal to 0 the curves couldn't completely reach the corresponding boundaries since the areas where they have evolved are not noise-free. Besides, in those cases making λ equal to 1 couldn't work either, that is, curves couldn't stop at the boundaries but have passed through them since the thicknesses of intima and adventitia are fairly small. In other words, for these boundaries there is a need to select λ value between 0 and 1 for accurate segmentation.

- Although finding an optimal λ value (for outer intima, inner adventitia and outer adventitia) is not a straightforward task, the number of trials can be significantly reduced if the right analysis is made. Basically, as can be concluded from the results, there are two determinants that have an impact on the selection of λ, namely, *the amount of noise present in the area where the curve evolves* and *the distance between the inner and outer boundaries of the layer (i.e., thickness of the layer).* As far as the optimal λ values of the outer intima and inner adventitia are concerned, it can be seen in Table 1 that they are equal to each other at 30 mmHg and very close at 60 & 90 mmHg. These situations can be explained by the facts that the upper and lower parts of the media (where the curve evolves) have similar characteristics in terms of the noise and the thickness of both layers (intima & adventitia) are comparable. As for the outer adventitia, it should be noted that the comparison of its λ value with that of the other boundaries might not be so reliable. The reason is that in detecting the

outer adventitia initial contour was placed closer to the target boundary than placed in detecting the other boundaries due to significant amount of noise between the adventitia and fat.

To sum up, the obtained segmentation results have shown that using only $\phi_{amplitude}$ ($\lambda = 0$) as a stopping function makes the segmentation very vulnerable to noise and causes the evolving contours to get stuck somewhere before reaching the boundary. This result has already been expected, because when $\phi_{amplitude}$ is used on its own, the curve evolution would be affected by two derivatives of the image. The results have also revealed the weakening of the stopping power when only ϕ_{phase} ($\lambda = 1$) is used. Since, unlike $\phi_{amplitude}$, ϕ_{phase} does not involve a derivative, the feature of "extra stopping power" embedded in the classical geodesic active contour model cannot be leveraged when ϕ_{phase} is used on its own. The negative effect of this weakened stopping power would be elevated if inner and outer boundaries of the layer are close to each other. The reason is that in those cases the contour would be easily attracted by the next farther boundary, and since the power of the model "to push the curve back" is weakened, the contour passes through the target boundary and stops somewhere between the target and next farther boundary or maybe even reaches the next farther boundary and then stops its evolution. Also, it has been shown that for some boundaries there is a need to select λ value between 0 and 1. But because that is not a straightforward task, in the following section region-based information is also incorporated into the model to further increase its robustness with respect to noise and coefficient values.

4.2 Incorporation of Region-Based Information

In Section 4.1, to make the segmentation more robust to noise, a novel stopping function that involves both gray-scale amplitude and local phase of the image has been developed. To achieve extra element of robustness, region-based information

[97] is now incorporated into the edge-based segmentation. The region for each curve is bounded by its adjacent evolving curves, and the idea is to maximize the difference between the average intensities inside and outside the curve. Then, as an example, the new energy term for a contour that moves outwards (e.g., the one being evolved to detect the inner intima) and whose inside and outside average intensities are w_1 and w_2, respectively, will be as in Eq. 10:

$$E = (1-\alpha)\int_{\overrightarrow{C}} \phi \, ds - \alpha \, \frac{1}{2}(w_1 - w_2)^2 \tag{10}$$

where $0 \leq \alpha \leq 1$ is a weighting factor between the edge and region-based energy terms. The corresponding curve evolution equation will then be:

$$\overrightarrow{C_t} = -\nabla E = (1-\alpha)\,(\phi\kappa - \nabla\phi \cdot \overrightarrow{N})\overrightarrow{N} + \alpha\,(I(x,y) - \frac{(w_1+w_2)}{2})\overrightarrow{N} \tag{11}$$

where $\overrightarrow{N}$ is the outward unit normal and $I(x,y)$ is the image intensity at (x,y) on the curve $\overrightarrow{C}$.

To detect the five boundaries (i.e., inner & outer intima, inner & outer adventitia and fat), as opposed to Section 4.1 where the detection of each boundary was done completely in an independent way, now the curves are moved one at a time beginning from the innermost one up to the outer ones. The motivation here is to simulate the real deformation of the artery when pressurized from inside; that is, first, the innermost boundary is deformed and then deformation waves are conveyed towards outside. The curve evolution of each contour will be as given in Eq. 11. For the implementation, level sets are used and for each contour a particular level set function is defined. As an example, the level set equation of the curve evolution given in Eq. 11 will be like the following:

$$\psi_t = -\overrightarrow{C_t} \cdot \nabla\psi = \{(1-\alpha)\,(-\phi\kappa + \nabla\phi \cdot \overrightarrow{N}) - \alpha\,(I(x,y) - \frac{(w_1+w_2)}{2})\}\overrightarrow{N} \cdot \nabla\psi \tag{12}$$

where ψ is the level set function. Choosing ψ to be positive inside of $\overrightarrow{C}$ bounded by its inferior contour or the origin (in the case of inner intima detection) and negative

outside of $\overrightarrow{C}$ bounded by its superior contour allows writing $\overrightarrow{N} = -\nabla\psi/\|\nabla\psi\|$ and therefore

$$\psi_t = (1-\alpha)\ (\phi\|\nabla\psi\|\kappa + \nabla\phi\cdot\nabla\psi) + \alpha\ (I(x,y) - \frac{(w_1+w_2)}{2})\|\nabla\psi\| \qquad (13)$$

In Eq. 13, there are two parameters to be selected. One of them is α, which is a weighting factor between the edge- and region-based terms, and the other one is λ, which is included in the stopping function, ϕ and serves as a weighting factor between amplitude-based and phase-based terms (i.e., $\phi = \lambda\ \phi_{phase} + (1-\lambda)\ \phi_{amplitude}$). The α and λ values that provide good segmentation results are given in Table 2. As opposed to the Table 1 that involves the optimal λ values for the case only edge-based information being used, here λ values are not a concern. The main reason is that for the inner and outer intima using only region-based information turned out to provide accurate segmentation results. This is indeed an expected result because the main motivation behind incorporating the region-based information was to increase the robustness of the technique. Since the area around the intima includes relatively low amount of noise, the region-based segmentation worked on its own.

Table 2: Optimal α and λ values for the combined edge & region-based segmentation

	30 mmHg		60 mmHg		90 mmHg	
	α	λ	α	λ	α	λ
Inner intima	1	N/A	1	N/A	1	N/A
Outer intima	1	N/A	1	N/A	1	N/A
Inner adventitia	0.5	1	0.5	1	0.5	1
Outer adventitia	0.5	1	0.5	1	0.5	1
Fat	0.5	1	0.5	1	0.5	1

As for the adventitia and fat, it turned out that due to the high amount of noise there was a need to add phase-based edge information, which was proven in Section 4.1 to make the segmentation more robust to noise. For this purpose, as a first trial α was selected to be 0.5 for all pressures. Then, the obtained results showed that

the value of 0.5 for α provided fairly good detection of inner & outer adventitia and fat. As a result, incorporating region-based information has indeed increased the robustness of the segmentation algorithm (especially for the detection of the inner and outer intima) and made it easier to deal with the weighting coefficients.

The segmentation results obtained using the parameter values given in Table 2 of the coronary artery vessel wall images at 30, 60 and 90 mmHg are given in Figures 39, 40 and 41, respectively.

Figure 39: Segmentation of the coronary artery vessel wall for 30 mmHg

Figure 40: Segmentation of the coronary artery vessel wall for 60 mmHg

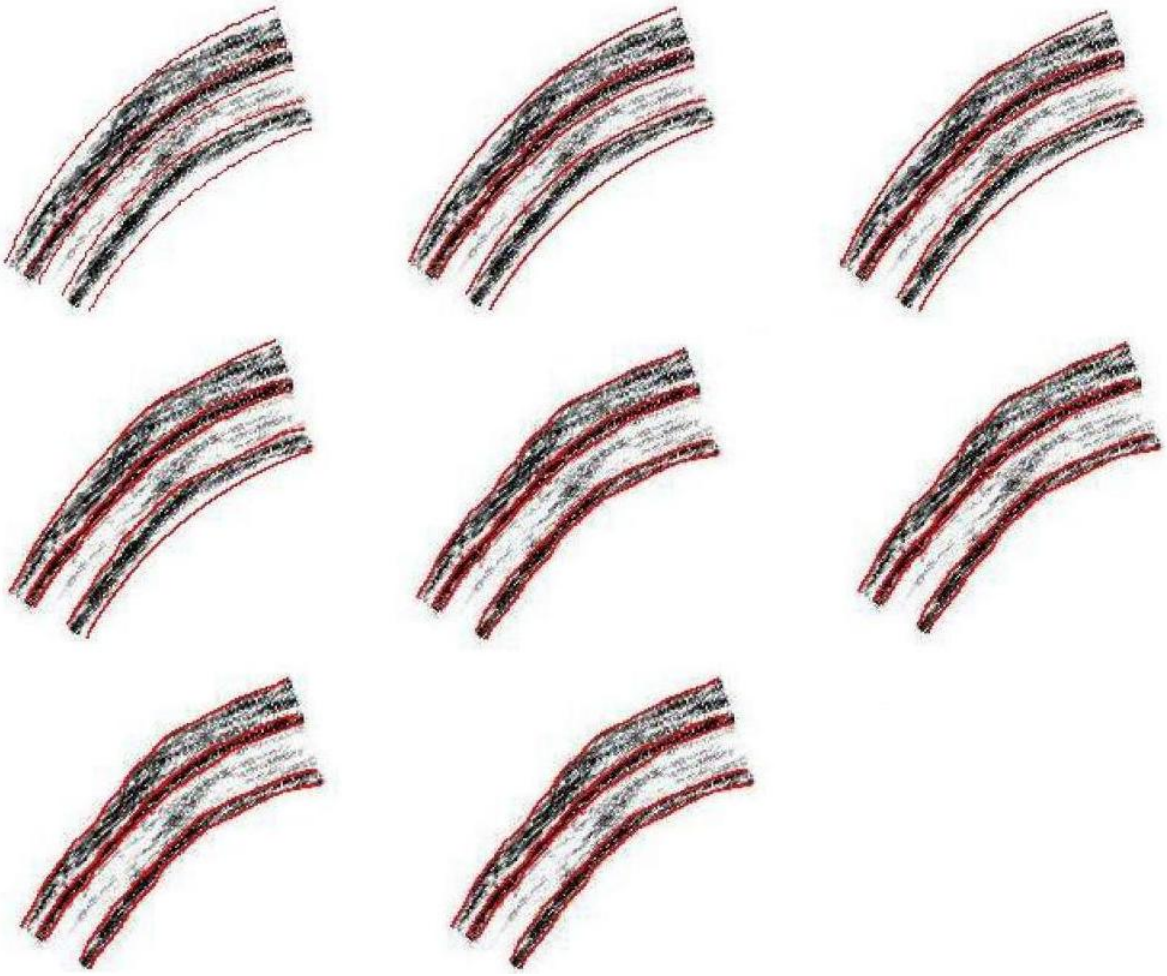

Figure 41: Segmentation of the coronary artery vessel wall for 90 mmHg

4.3 Segmentation Based on Elliptical Deformable Template

The main motivation behind this chapter has been to develop the "best" segmentation algorithm to detect the coronary vessel wall boundaries. In Section 4.1, the local phase information was added to the classical geodesic active contour framework to make the segmentation robust to noise which is present in the acquired high-resolution coronary vessel wall ultrasound images. In Section 4.2, the region-based information was also incorporated into the algorithm to further increase the robustness. Although all of these efforts seem to work out, there are even further improvements that can be applied on the proposed model.

Specifically, to improve the stability of the deformable contour algorithm it is better to include in the model as much a priori information as possible. Using a prior model to constrain the segmentation would provide more accurate segmentation results [7]. On the other hand, it is known that coronary vessels are circular/elliptical tissue structures. Therefore, it is reasonable to impose an elliptical model on the evolving contours[8]. In the following subsections, first a novel elliptical deformable template is presented, and then how to make refinements to this elliptical model is shown.

4.3.1 Global Optimization

In all of the deformable contour techniques, the aim is to optimize the contour so that it fits image edges as closely as possible. In this subsection, the contour optimization is constrained by the use of an elliptical model. Specifically, an ellipse center is fixed at a point (x_0, y_0), leaving the three parameters to be used to describe the ellipses: the length of the two axes a and b, and the angle φ. Since there are five boundaries to be detected, five ellipse segments are drawn with the same center (x_0, y_0), and initial

[8]Because circle is indeed a special kind of ellipse, elliptical template is used to make the curves better fit the edges.

parameters (a_1, b_1, φ_1), (a_2, b_2, φ_2), (a_3, b_3, φ_3), (a_4, b_4, φ_4) and (a_5, b_5, φ_5).

To draw the ellipse, first, x and y coordinates are computed in terms of the ellipse parameters. As an example, for the first ellipse segment the x and y coordinates would be:

$$x = -a_1 \cos(2\pi\rho)\sin(\varphi_1) + b_1 \sin(2\pi\rho)\cos(\varphi_1) + x_0 \tag{14}$$

$$y = a_1 \cos(2\pi\rho)\cos(\varphi_1) + b_1 \sin(2\pi\rho)\sin(\varphi_1) + y_0 \tag{15}$$

where the curve is sampled on the variable ρ: $\rho_i = \frac{2i\pi}{N}$. Here, N represents the number of sample points taken on the ellipse segment, which is selected to be 250.

The objective then is by minimizing the energy functional given in Eq. 16 to optimize the ellipse parameters a_1, b_1 and φ_1 so that the deformable contour fits the image boundary (in this case inner intima) as closely as possible.

$$E_1 = (1-\alpha)\int_{\overrightarrow{C_1}} \phi \, ds - \alpha \, \frac{1}{2}(w_1 - w_2)^2 \tag{16}$$

Because in reality when the artery is pressurized from inside first the innermost boundary is deformed, and then the deformation waves are conveyed to outer boundaries, in the implementation of the proposed elliptical model the curves are similarly deformed one at a time beginning from the innermost ellipse segment to the outer ones. This way, the implementation becomes also relatively less complex since the optimal parameters of a particular ellipse segment can be determined by minimizing only its corresponding energy. If for the first ellipse segment the three parameters are put together in the vector $\overrightarrow{e_1} = (a_1, b_1, \varphi_1)$, the update equation can then be written using gradient-descent as follows:

$$\frac{\partial \overrightarrow{e_1}}{\partial t} + h \, \frac{\partial E_1}{\partial \overrightarrow{e_1}} = 0 \tag{17}$$

where energy minimization is accomplished directly in the space of ellipse parameters; h and t corresponds to a step size and time, respectively.

Having obtained the energy functionals E_2, E_3, E_4 & E_5 as well as the parameter vectors $\overrightarrow{e_2}$, $\overrightarrow{e_3}$, $\overrightarrow{e_4}$ & $\overrightarrow{e_5}$ in a similar way, gradient-descent equations are also written for other ellipse segments.

In the following, for the sake of demonstration, only the first ellipse segment is taken into consideration, but similar computations are also done for other ellipse segments, as well.

Energy functional in Eq. 16 actually consists of two terms, namely, edge-based and region-based terms (e.g., $E_1 = E_1^{edge} + E_1^{region}$). The edge-based energy term can be approximated as follows [78]:

$$E_1^{edge} = (1-\alpha) \int_{\overrightarrow{C_1}} \phi \, ds \simeq (1-\alpha) \sum_{i=1}^{N} \phi(x_i, y_i) \tag{18}$$

where x_i and y_i are the coordinates of the sample point i on the ellipse segment. Taking its gradient with respect to ellipse parameters and using chain rule result in the following:

$$\frac{\partial E_1^{edge}}{\partial \overrightarrow{e_1}} = (1-\alpha) \sum_{i=1}^{N} \frac{\partial \phi(x_i, y_i)}{\partial \overrightarrow{e_1}} \tag{19}$$

$$= (1-\alpha) \sum_{i=1}^{N} \frac{\partial \phi(x_i, y_i)}{\partial x} \frac{\partial x}{\partial \overrightarrow{e_1}} + \frac{\partial \phi(x_i, y_i)}{\partial y} \frac{\partial y}{\partial \overrightarrow{e_1}} \tag{20}$$

In Eq. 20, for the computation of $\frac{\partial \phi(x_i, y_i)}{\partial x}$ and $\frac{\partial \phi(x_i, y_i)}{\partial y}$, the following central difference approximations are used:

$$\frac{\partial \phi(x_i, y_i)}{\partial x} = \frac{\phi(x_i + 1, y_i) - \phi(x_i - 1, y_i)}{2}$$
$$\frac{\partial \phi(x_i, y_i)}{\partial y} = \frac{\phi(x_i, y_i + 1) - \phi(x_i, y_i - 1)}{2}$$

. On the other hand, to compute the gradient of x and y coordinates taken with respect to $\overrightarrow{e_1} = (a_1, b_1, \varphi_1)$, the Eqs. 14 and 15 are used. The computed gradients

are then given by

$$\begin{aligned}
\frac{\partial x}{\partial a_1} &= -\cos(2\pi\rho)\sin\varphi_1, \quad \frac{\partial y}{\partial a_1} = \cos(2\pi\rho)\cos\varphi_1, \\
\frac{\partial x}{\partial b_1} &= \sin(2\pi\rho)\cos\varphi_1, \qquad \frac{\partial y}{\partial b_1} = \sin(2\pi\rho)\sin\varphi_1, \\
\frac{\partial x}{\partial \varphi_1} &= -a_1\cos(2\pi\rho)\cos\varphi_1 - b_1\sin(2\pi\rho)\sin(\varphi_1), \\
\frac{\partial y}{\partial \varphi_1} &= -a_1\cos(2\pi\rho)\sin\varphi_1 + b_1\sin(2\pi\rho)\cos(\varphi_1).
\end{aligned} \tag{21}$$

On the other hand, the region-based energy term is given in Eq. 22.

$$E_1^{region} = -\alpha\,\frac{1}{2}(w_1 - w_2)^2 \tag{22}$$

Recalling that w_1 and w_2 are the average intensities inside and outside the curve bounded by the adjacent curves, the region-based energy term can also be written as follows:

$$E_1^{region} = -\alpha\,\frac{1}{2}(w_1 - w_2)^2 = -\alpha\,\frac{1}{2}(\frac{S_1}{A_1} - \frac{S_2}{A_2})^2 \tag{23}$$

where $w_1 = S_1/A_1$, $S_1 = \int\int_{R_1^{in}} I dA$, $A_1 = \int\int_{R_1^{in}} dA$, $w_2 = S_2/A_2$, $S_2 = \int\int_{R_1^{out}} I dA$, $A_2 = \int\int_{R_1^{out}} dA$, and R_1^{in} & R_1^{out} are the regions inside and outside the curve (bounded by the adjacent curves).

Then, the gradient of Eq. 23 with respect to ellipse parameters will be written as follows [88]:

$$\frac{\partial E_1^{region}}{\partial \overrightarrow{e_1}} = \alpha(w_2 - w_1)(\frac{\frac{\partial S_1}{\partial \overrightarrow{e_1}} - w_1\frac{\partial A_1}{\partial \overrightarrow{e_1}}}{A_1} - \frac{\frac{\partial S_2}{\partial \overrightarrow{e_1}} - w_2\frac{\partial A_2}{\partial \overrightarrow{e_1}}}{A_2}) \tag{24}$$

To compute the gradients of S_1, A_1, S_2 and A_2, the level sets are used. Basically, the ellipse segment, i.e., $\overrightarrow{C_1}$, is represented by the zero level set of ψ_1:

$$\overrightarrow{C_1} = \{(x, y) \in \Re^2 : \psi_1(x, y) = 0\}$$

As for the regions R_1^{in} and R_1^{out}, the following level set representations are used[9]:

$$R_1^{in} = \{(x, y) \in \Re^2 : \psi_1(x, y) > 0\}$$

$$R_1^{out} = \{(x, y) \in \Re^2 : \psi_1(x, y) < 0\}$$

[9]Since here the first ellipse segment which is to move outwards to detect the inner intima is

Then, the next step is to write S_1, A_1, S_2 and A_2 in terms of the level set function ψ_1 as given in the following:

$$S_1 = \int\int_{R_1^{in}\&R_1^{out}} IH(\psi_1)dA$$
$$A_1 = \int\int_{R_1^{in}\&R_1^{out}} H(\psi_1)dA$$
$$S_2 = \int\int_{R_1^{in}\&R_1^{out}} IH(-\psi_1)dA$$
$$A_2 = \int\int_{R_1^{in}\&R_1^{out}} H(-\psi_1)dA$$

where the Heaviside function H is given by

$$H(\psi_1) = \begin{cases} 1 & \text{if } \psi_1 \geq 0; \\ 0 & \text{if } \psi_1 < 0. \end{cases}$$

As shown in Eq. 24, to find the gradient of the region-based energy term taken with respect to the ellipse parameters, there is a need to compute the gradients of S_1, A_1, S_2 and A_2 with respect to the ellipse parameters. Defining the one-dimensional Dirac measure δ concentrated at zero by

$$\delta(z) = \frac{d}{dz}H(z)$$

the gradient terms in Eq. 24 can now be expressed as line integrals along $\overrightarrow{C_1}$ as shown in the following:

$$\frac{\partial S_1}{\partial \overrightarrow{e_1}} = \int_{\overrightarrow{C_1}} I \frac{\partial \psi_1}{\partial \overrightarrow{e_1}} ds$$
$$\frac{\partial A_1}{\partial \overrightarrow{e_1}} = \int_{\overrightarrow{C_1}} \frac{\partial \psi_1}{\partial \overrightarrow{e_1}} ds$$
$$\frac{\partial S_2}{\partial \overrightarrow{e_1}} = -\int_{\overrightarrow{C_1}} I \frac{\partial \psi_1}{\partial \overrightarrow{e_1}} ds$$
$$\frac{\partial A_2}{\partial \overrightarrow{e_1}} = -\int_{\overrightarrow{C_1}} \frac{\partial \psi_1}{\partial \overrightarrow{e_1}} ds$$

being considered, for the region inside the curve the level set function is selected to have a positive value and for the region outside the curve to have negative value. This is also the case for the third ellipse segment which is moved to detect the inner adventitia. However, for the second, fourth and fifth ellipse segments which are to move inwards to detect their corresponding boundaries, this sign selection is inverted.

Using chain rule, $\frac{\partial \psi_1}{\partial \overrightarrow{e_1}}$ can actually be written as follows:

$$\frac{\partial \psi_1}{\partial \overrightarrow{e_1}} = \frac{\partial \psi_1}{\partial x} \frac{\partial x}{\partial \overrightarrow{e_1}} + \frac{\partial \psi_1}{\partial y} \frac{\partial y}{\partial \overrightarrow{e_1}}$$

For the computation of $\frac{\partial \psi_1}{\partial x}$ and $\frac{\partial \psi_1}{\partial y}$ along the curve, the following central difference approximations are used .

$$\frac{\partial \psi_1(x_i, y_i)}{\partial x} = \frac{\psi_1(x_i + 1, y_i) - \psi_1(x_i - 1, y_i)}{2}$$
$$\frac{\partial \psi_1(x_i, y_i)}{\partial y} = \frac{\psi_1(x_i, y_i + 1) - \psi_1(x_i, y_i - 1)}{2}$$

. As for $\frac{\partial x}{\partial \overrightarrow{e_1}}$ and $\frac{\partial y}{\partial \overrightarrow{e_1}}$, however, the equalities given in Eq. 21 are used..

As a result of all the above computations, which were done in MATLAB, $\frac{\partial E_1^{edge}}{\partial \overrightarrow{e_1}}$ and $\frac{\partial E_1^{region}}{\partial \overrightarrow{e_1}}$ were obtained, and then the update equation given in Eq. 17 was run to get the updated ellipse parameters that determine the final/optimal location of the segmenting curve. This same procedure was exactly applied for the other curves to find their optimal ellipse parameters.

The results of this "global optimization" are shown in Figures 42-48. In the implementation, the iterations were stopped when an energy minimum was reached. To avoid early stop due to energy local minimum, however, the algorithm was allowed to go ahead even though the energy was not decreasing. If a lower value of the energy was not found in a certain amount of steps, iterations were certainly stopped. Step sizes were determined by trial and error. Basically, too big of a step size would overshoot the function minimum, and too small of a step size result in a long convergence time.

As can be visually seen from the segmentation results of image 30 and 60 mmHg, the use of elliptical deformable template has provided the evolving curves to detect the image boundaries very closely. This result has already been expected. On the other hand, the elliptical template hasn't worked for 90 mmHg image especially for the adventitia. This implies that there is a need to use a higher degree polynomial

template for the coronary vessel wall images at very high pressures such as 90 mmHg or more. Since the main idea behind either elliptical or higher degree polynomial template is indeed same, for the rest of the work still elliptical deformable template will be used, leaving the implementation of the higher degree polynomial template as a future work. Therefore, in the next section and chapter where the boundary refinement and strain estimation is discussed, respectively, 30 and 60 mmHg images will be of the main interest.

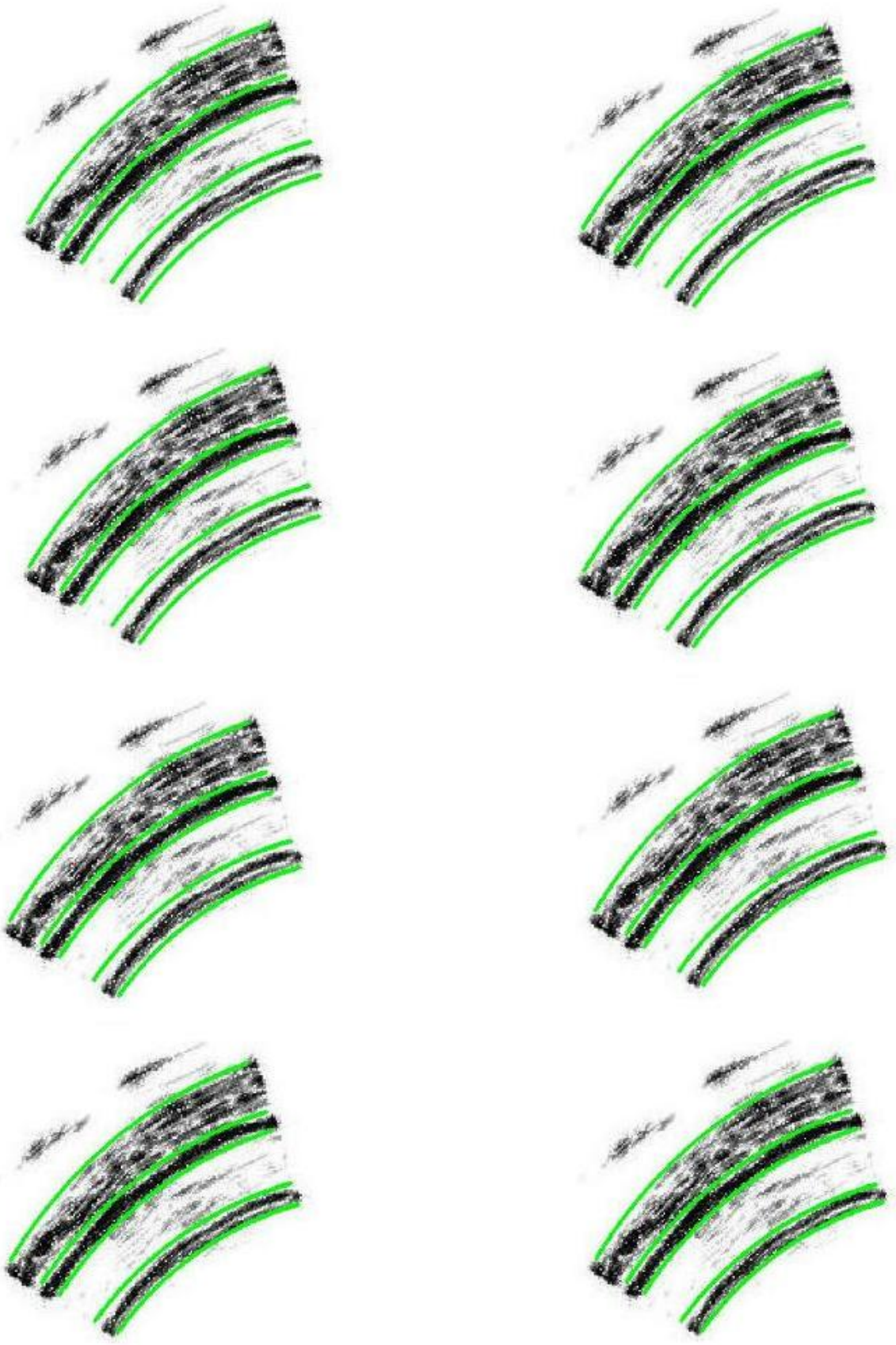

Figure 42: Global optimization for the image at 30mmHg

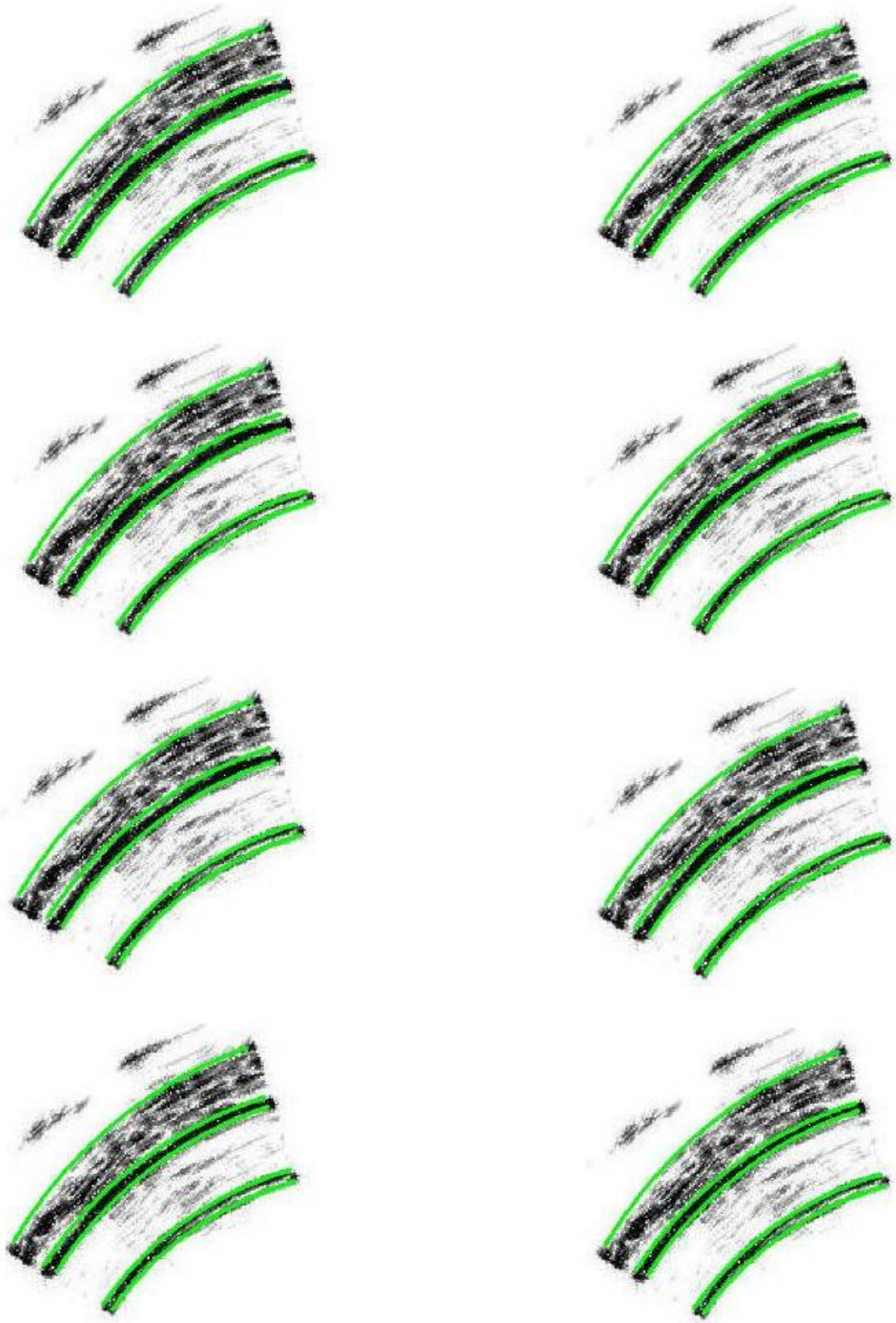

Figure 43: Global optimization for the image at 30mmHg (cont)

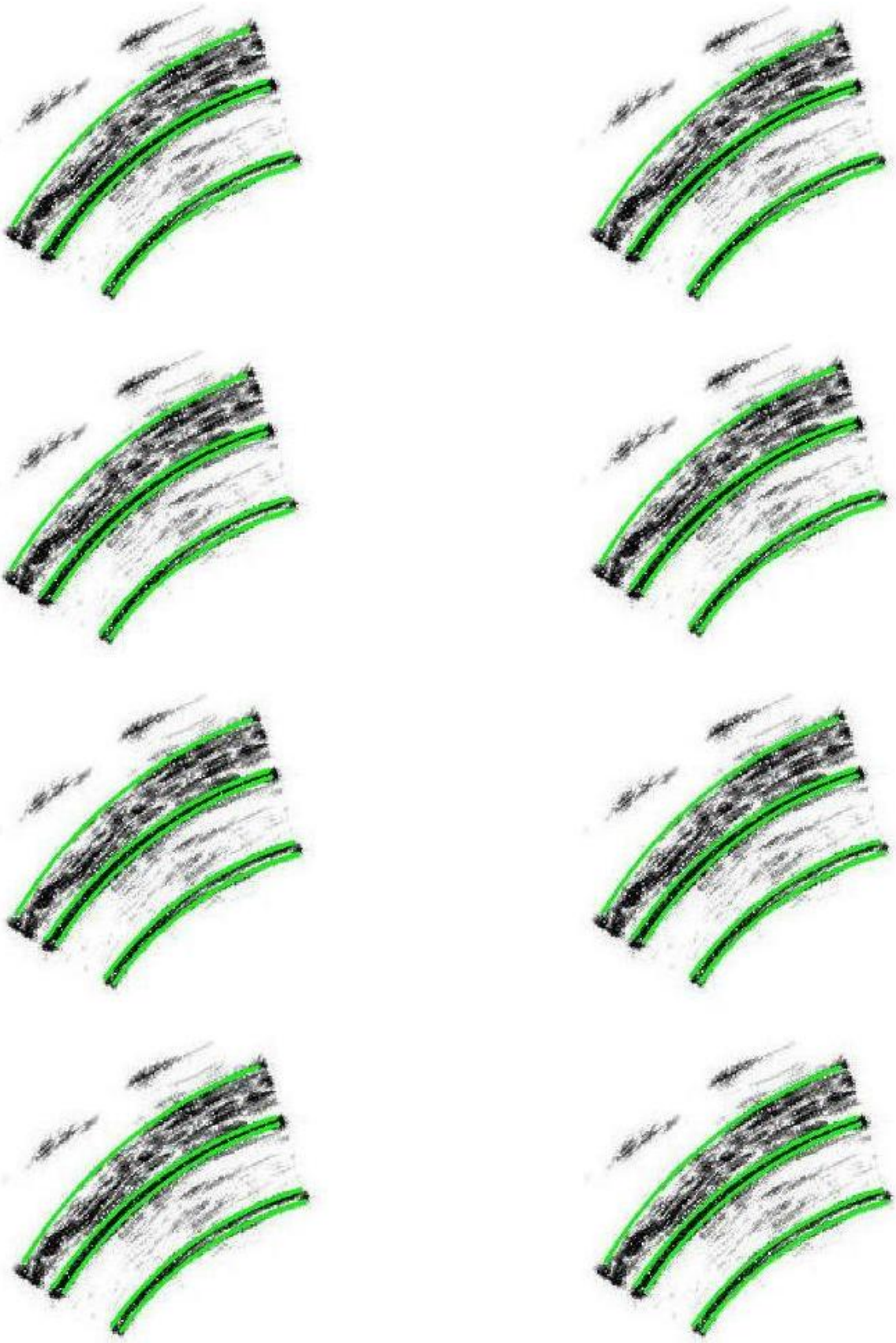

Figure 44: Global optimization for the image at 30mmHg (cont)

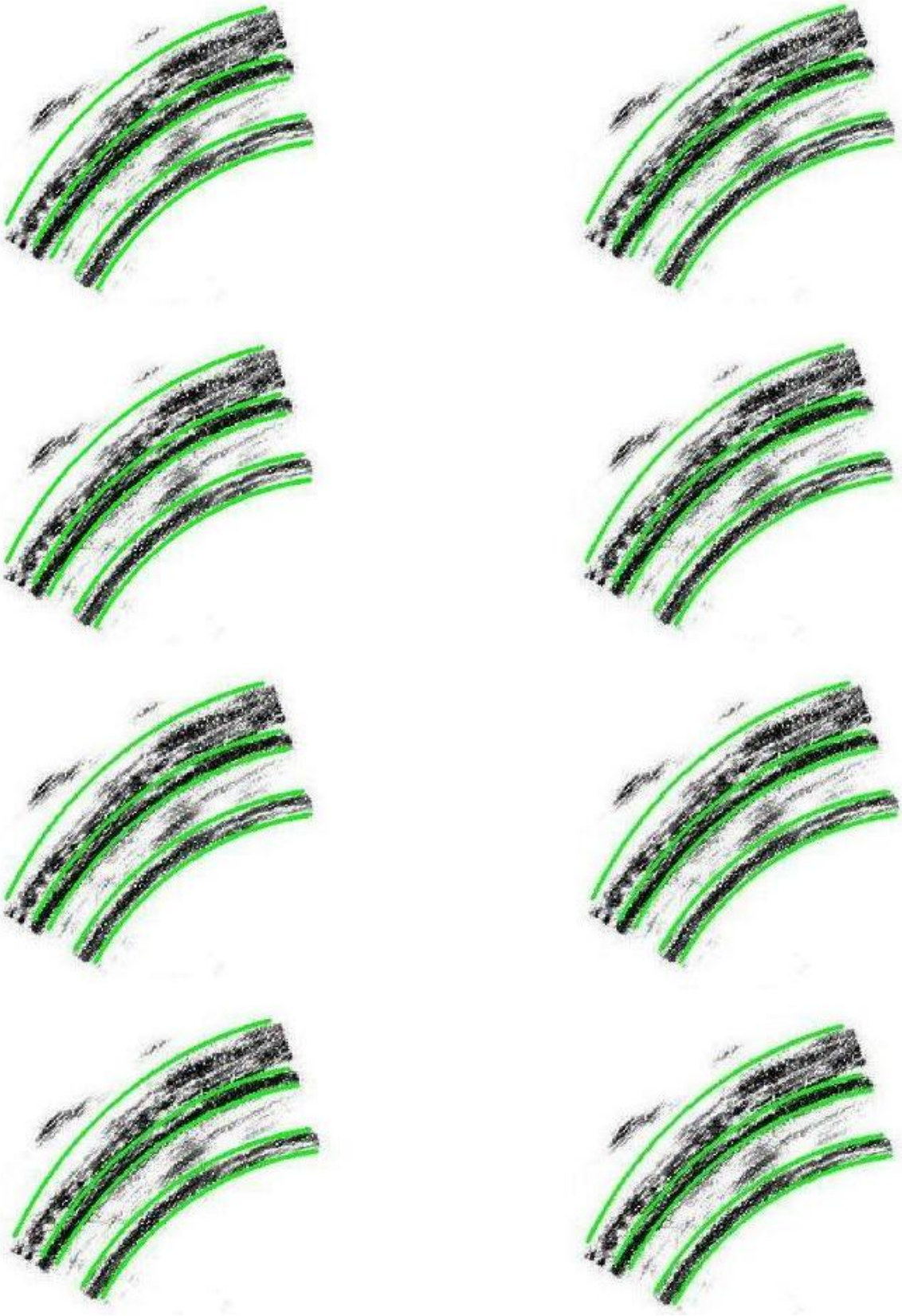

Figure 45: Global optimization for the image at 60mmHg

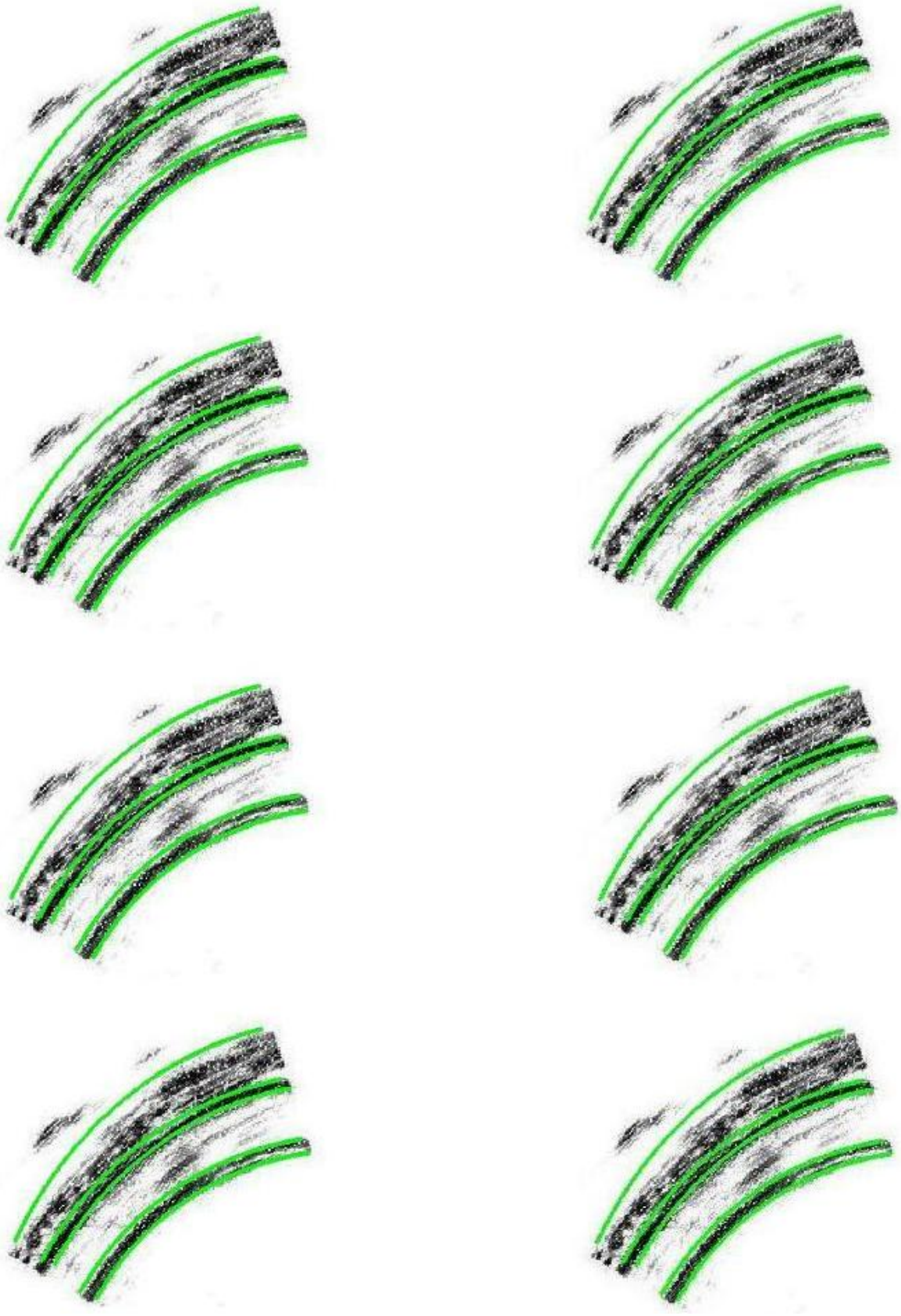

Figure 46: Global optimization for the image at 60mmHg (cont)

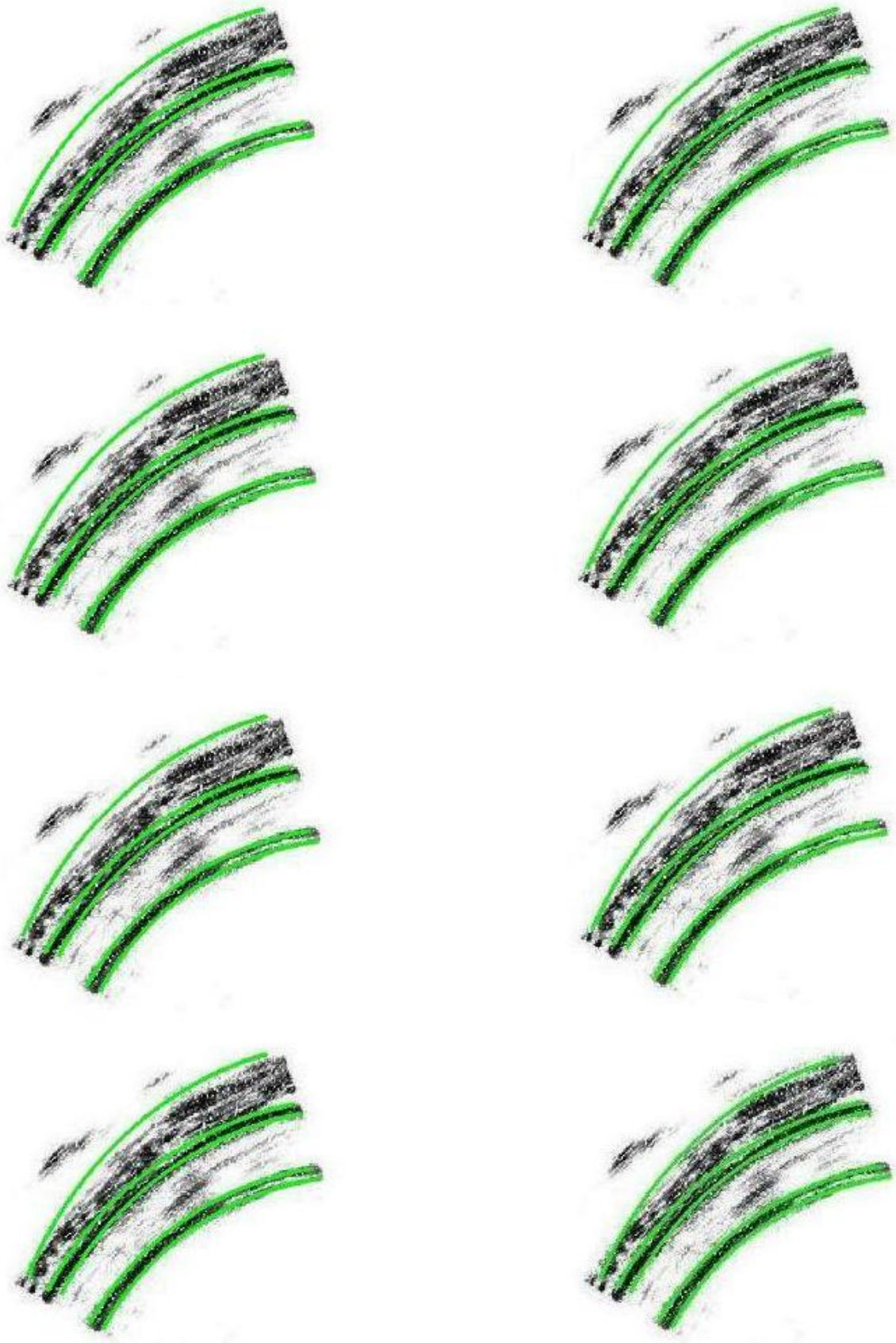

Figure 47: Global optimization for the image at 60mmHg (cont)

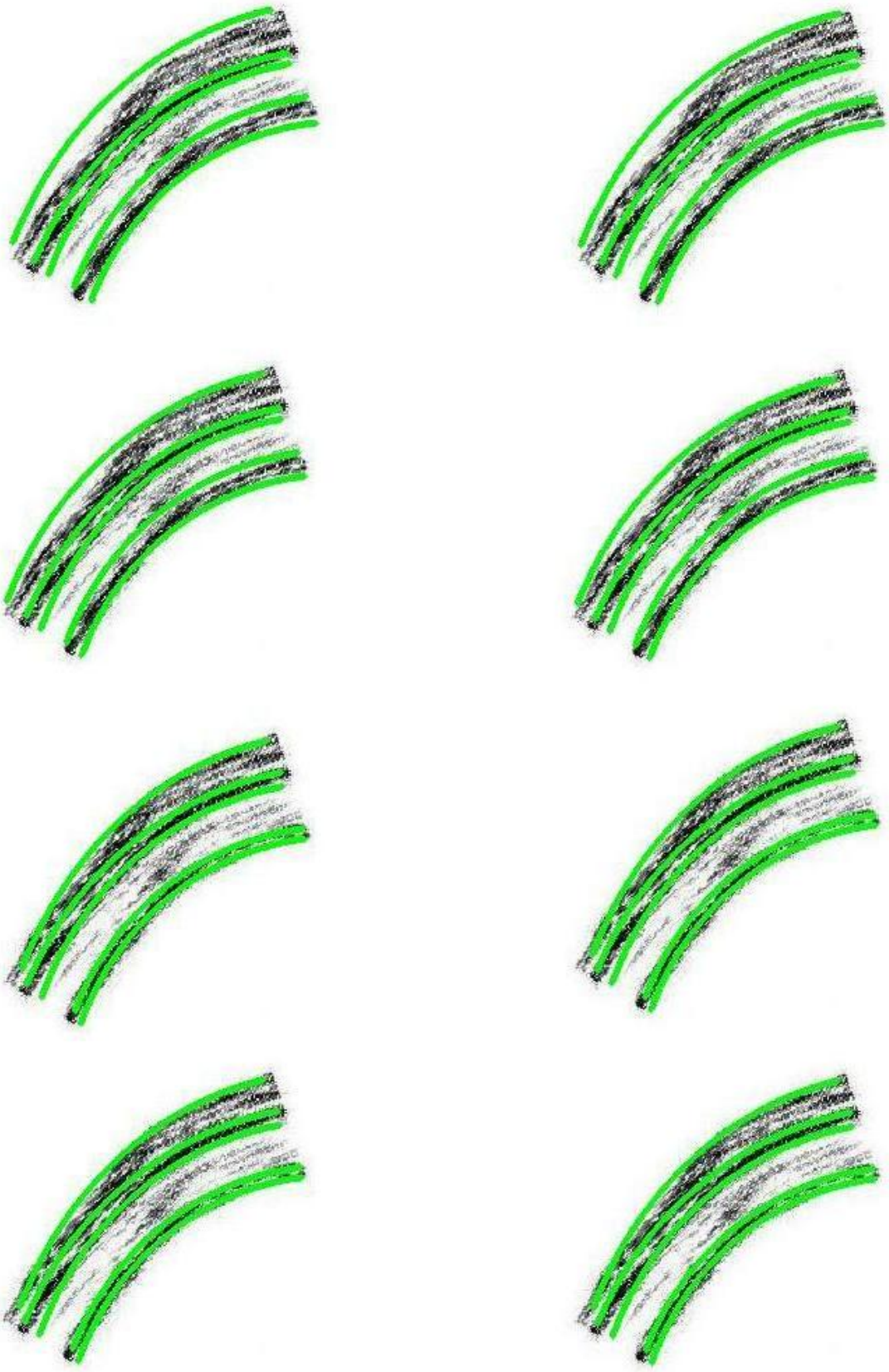

Figure 48: Global optimization for the image at 90mmHg

4.3.2 Boundary Refinement

Although the elliptical deformable template presented in Subsection 4.3.1 fits well with the nature of the arteries and provides the evolving contours to more or less detect the boundaries, there is a need for refinement step so that the contours better fit the image boundaries. Specifically, in this refinement step the elliptical shape constraint is relaxed to treat deformations that do not obey to the elliptical model (e.g., non-rigid deformations).

If the energy functionals obtained in Subsection 4.3.1 are considered together, the new energy functional in this "boundary refinement" step is given by

$$E_{new} = E_1+E_2+E_3+E_4+E_5+\int\int_{image}\{\beta\ (u^2+v^2)+\ \gamma\ (u_x^2+u_y^2+v_x^2+v_y^2)\}\ dxdy \quad (25)$$

where u and v are the components of a 2D vector field such that, as an example, a point located at (x_i, y_i) moves to $(x_i+u(x_i, y_i), y_i+v(x_i, y_i))$. In Eq. 25, the objective is to minimize E_{new} with respect to u and v. While the energy functionals, E_1, E_2, E_3, E_4 and E_5 are directly taken from the Subsection 4.3.1, the last part penalizes the magnitude and roughness (derivative) of the 2D vector field. The coefficients β and γ are the weighting factors between those magnitude and derivative terms.

Using gradient-descent on Eq. 25, the following equations are obtained:

$$\frac{\partial u}{\partial t} + h\ \frac{\partial E}{\partial u} = 0 \quad (26)$$

$$\frac{\partial v}{\partial t} + h\ \frac{\partial E}{\partial v} = 0 \quad (27)$$

.

In the above gradient-descent equations, the particular interest is to compute the u and v for the contour points. To do this, the Eqs. 20 and 24 are used; however, the gradients are now taken with respect to u and v instead of the ellipse parameters. Also, the equations for the gradients of the x and y coordinates taken with respect

to u and v need to be computed. Basically, those gradient equations are given by

$$\frac{\partial x}{\partial u} = 1 \;\; \& \;\; \frac{\partial x}{\partial v} = 0,$$
$$\frac{\partial y}{\partial u} = 0 \;\; \& \;\; \frac{\partial y}{\partial v} = 1.$$

If, for the sake of display, a point (x_i, y_i) located on the first contour is taken into consideration, then the gradient-descent equations given in Eqs. 26 and 27 can be written as follows:

$$\frac{\partial u(x_i,y_i)}{\partial t} + h\{(1-\alpha)\frac{\partial \phi(x_i,y_i)}{\partial x} - \alpha(w_1 - w_2)(\frac{I(x_i,y_i)\frac{\partial \psi_1(x_i,y_i)}{\partial x} - w_1\frac{\partial \psi_1(x_i,y_i)}{\partial x}}{R_1^{in}} + \frac{I(x_i,y_i)\frac{\partial \psi_1(x_i,y_i)}{\partial x} - w_2\frac{\partial \psi_1(x_i,y_i)}{\partial x}}{R_1^{out}}) + \beta u(x_i,y_i) - \gamma\nabla^2 u(x_i,y_i)\} = 0 \quad (28)$$

$$\frac{\partial v(x_i,y_i)}{\partial t} + h\{(1-\alpha)\frac{\partial \phi(x_i,y_i)}{\partial y} - \alpha(w_1 - w_2)(\frac{I(x_i,y_i)\frac{\partial \psi_1(x_i,y_i)}{\partial y} - w_1\frac{\partial \psi_1(x_i,y_i)}{\partial y}}{R_1^{in}} + \frac{I(x_i,y_i)\frac{\partial \psi_1(x_i,y_i)}{\partial y} - w_2\frac{\partial \psi_1(x_i,y_i)}{\partial y}}{R_1^{out}}) + \beta v(x_i,y_i) - \gamma\nabla^2 v(x_i,y_i)\} = 0 \quad (29)$$

In Eqs. 28 and 29, the first two terms inside the bracket are the gradients of $E_1 = E_1^{edge} + E_1^{region}$ taken at (x_i, y_i) with respect to u and v. On the other hand, the last two terms are found using calculus of variations on the integral in Eq. 25 where the magnitude and roughness of the 2D vector field is penalized. In Eqs. 28 and 29, ∇^2 is the Laplacian operator, and the following hold for $\nabla^2 u(x_i, y_i)$ and $\nabla^2 v(x_i, y_i)$:

$$\nabla^2 u(x_i,y_i) = K\ (u(x_i+1,y_i) + u(x_i-1,y_i) + u(x_i,y_i+1) + u(x_i,y_i-1) - 4u(x_i,y_i))$$
$$\nabla^2 v(x_i,y_i) = K\ (v(x_i+1,y_i) + v(x_i-1,y_i) + v(x_i,y_i+1) + v(x_i,y_i-1) - 4v(x_i,y_i))$$

where K is the constant. If K is too small, then the convergence of the algorithm would be slow, while for a very large K the system would be unstable and oscillate. A value of 0.3 seemed to work quite well in the implementation.

As for the implementation, the displacement field whose gradient-descent is given in Eqs. 26 and 27 was iteratively computed. The beginning coordinates of the sample

points were taken as the ones obtained at the end of the global optimization step. Then, as u and v were being updated, they were added to the last coordinate values of the corresponding sample points. As in the implementation of "global optimization" step, iterations were stopped when an energy minimum was reached, and then the final location of each sample point would be obtained. By putting together those final coordinate values, the results of the "boundary refinement" step shown in Figures 49-52 were acquired. The coefficients β and γ were both selected to be 1.5. As can be visually seen from the segmentation results, due to this refinement step contours now better fit edges, resulting in more accurate boundary detection.

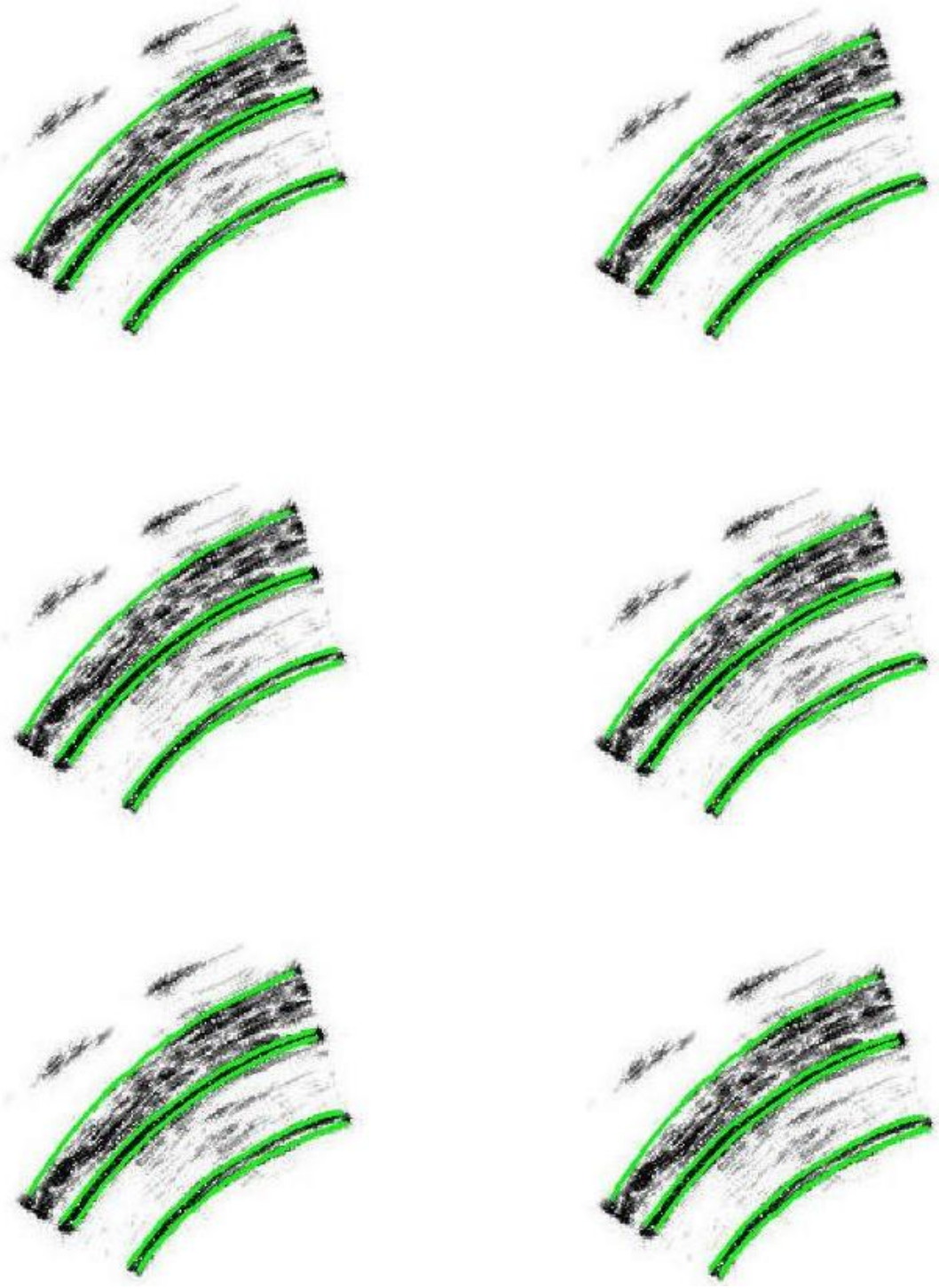

Figure 49: Boundary refinement for the image at 30mmHg

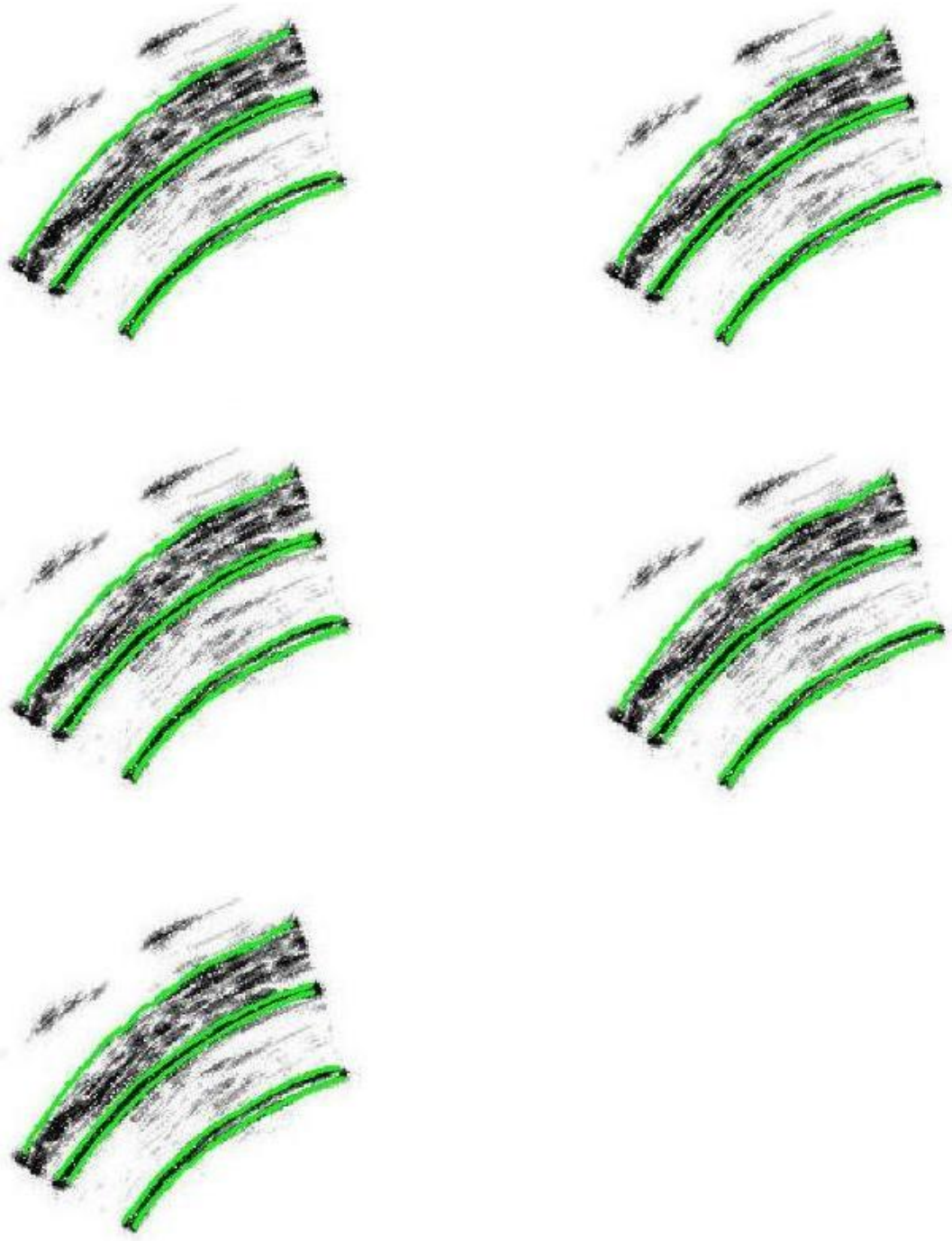

Figure 50: Boundary refinement for the image at 30mmHg (cont)

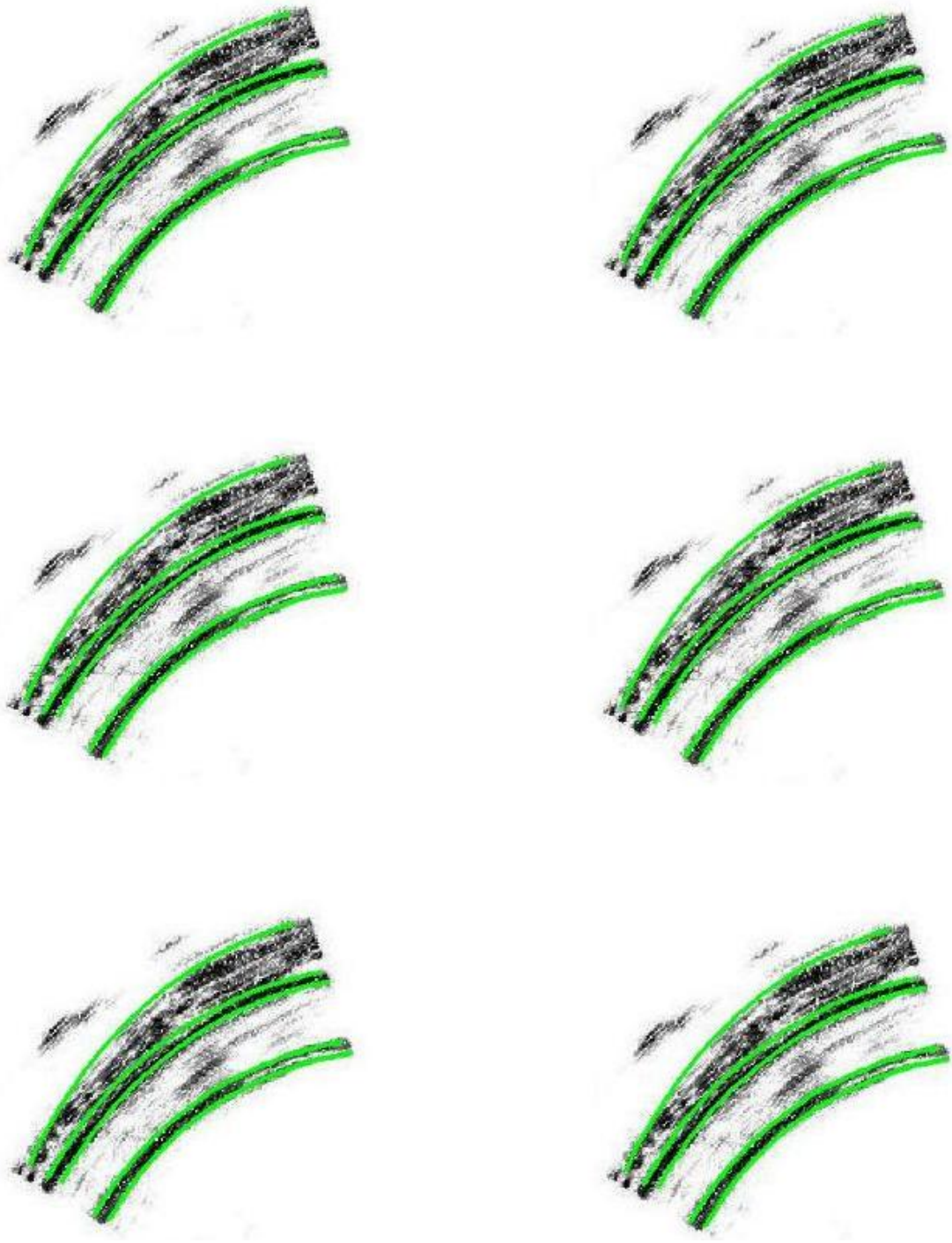

Figure 51: Boundary refinement for the image at 60mmHg

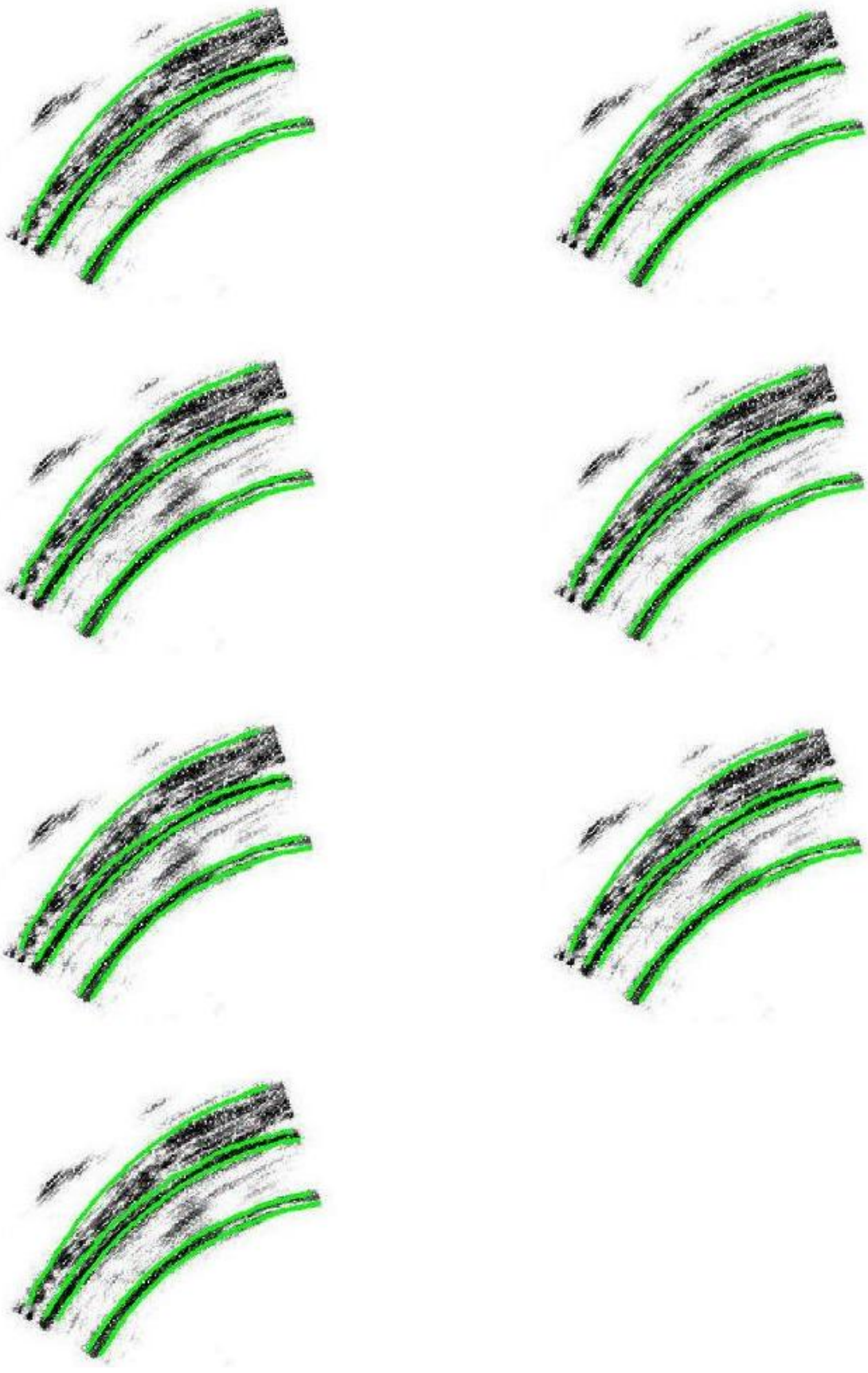

Figure 52: Boundary refinement for the image at 60mmHg (cont)

CHAPTER V

DEFORMATION ESTIMATION

The segmented images obtained by the use of elliptical deformable template (i.e., global optimization and boundary refinement) are shown in Figures 53 and 54. As explained in Section 4.3, in the segmentation of 30 and 60 mmHg coronary vessel wall images the same ellipse center has been used. Moreover, the number of sample points (i.e., N) taken has been set to 250 on each ellipse. Therefore, the segmentation results given in Figures 53 and 54 indeed implicitly provides boundary point correspondences.

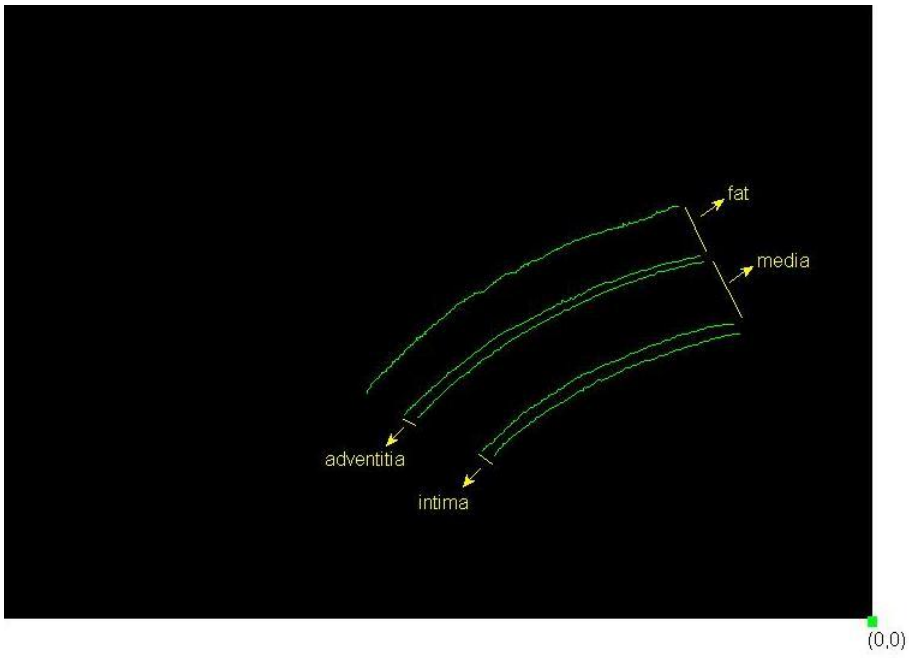

Figure 53: Segmented 30 mmHg coronary vessel wall image

The issue of boundary point correspondence can further be explained as a specific example. Let's assume that the optimal ellipse parameters of the inner intima at 30 mmHg have been found to be a_1, b_1 and φ_1 at the end of the global optimization step

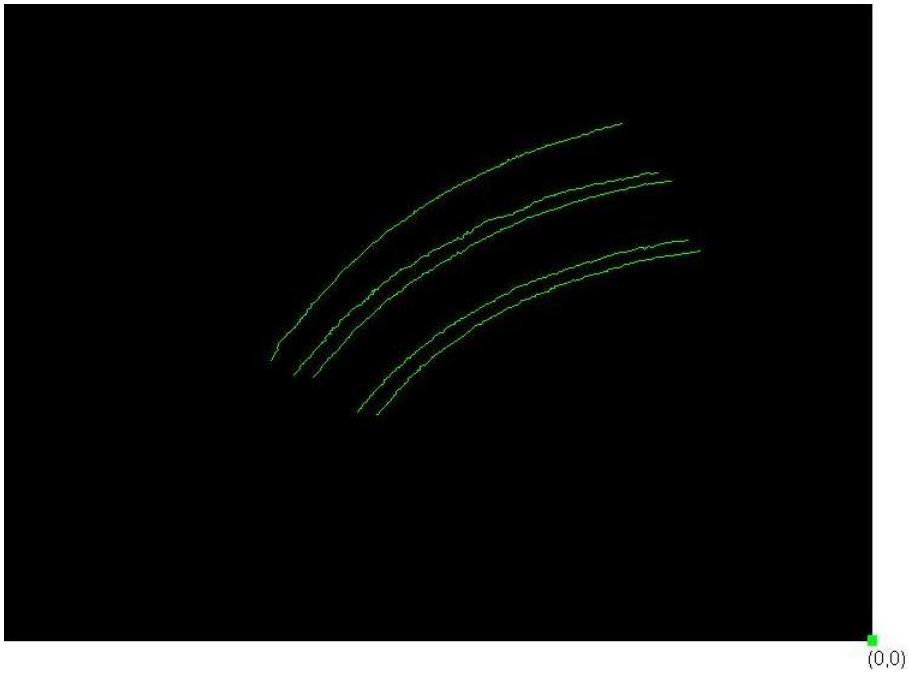

Figure 54: Segmented 60 mmHg coronary vessel wall image

in Subsection 4.3.1. Similarly, the optimal ellipse parameters of its corresponding boundary at 60 mmHg (i.e., inner intima of the 60 mmHg image) have been found to be $\hat{a}_1$, $\hat{b}_1$ and $\hat{\varphi}_1$. The center has already been fixed to (x_0, y_0). Then, x_i, y_i and $\hat{x}_i$, $\hat{y}_i$, which are the x and y components of the i^{th} sample point on the ellipses at 30 and 60 mmHg, respectively, would be as follows:

$$x_i = -a_1 \cos(2\pi\rho_i)\sin(\varphi_1) + b_1 \sin(2\pi\rho_i)\cos(\varphi_1) + x_0 \tag{30}$$
$$y_i = a_1 \cos(2\pi\rho_i)\cos(\varphi_1) + b_1 \sin(2\pi\rho_i)\sin(\varphi_1) + y_0$$

$$\hat{x}_i = -\hat{a}_1 \cos(2\pi\rho_i)\sin(\hat{\varphi}_1) + \hat{b}_1 \sin(2\pi\rho_i)\cos(\hat{\varphi}_1) + x_0 \tag{31}$$
$$\hat{y}_i = \hat{a}_1 \cos(2\pi\rho_i)\cos(\hat{\varphi}_1) + \hat{b}_1 \sin(2\pi\rho_i)\sin(\hat{\varphi}_1) + y_0$$

Since it has been known that intima at 30 and 60 mmHg are the matches for each other, and also been found that a_1, b_1 and φ_1 and $\hat{a}_1$, $\hat{b}_1$ and $\hat{\varphi}_1$ are the optimal parameters that define the corresponding ellipses/intimas, and also the center (x_0,y_0) are same for both ellipse, from Eqs. 30 and 31 it can be concluded that for the same

ρ_i a point that has been located at $(x_i,\ y_i)$ in 30 mmHg image now has a location of $(\hat{x}_i,\ \hat{y}_i)$. In other words, as far as global optimization step is concerned, the i^{th} sample point on the ellipse/intima at 30 mmHg corresponds to the i^{th} sample point on the ellipse/intima at 60 mmHg, $\forall i = 1, \cdots, N$.

Then, in the boundary refinement step, the sample points on the ellipses are just allowed to move locally. As an example, the i^{th} sample point in 30 mmHg image would move from (x_i, y_i) to $(x_i + u(x_i, y_i), y_i + v(x_i, y_i))$ while i^{th} sample point in 60 mmHg image move from $(\hat{x}_i, \hat{y}_i)$ to $(\hat{x}_i + \hat{u}(\hat{x}_i, \hat{y}_i), \hat{y}_i + \hat{v}(\hat{x}_i, \hat{y}_i))$, where u, v and $\hat{u}$, $\hat{v}$ are the components of the 2D displacement field, respectively. Referring to Figure 55 where the inner intima at 30 mmHg and 60 mmHg are drawn in the same diagram, these new and final locations would be, for example, k_i and $\hat{k}_i$, which are nothing but the correspondences of each other. In a similar way, the point correspondences between other boundaries of 30 and 60 mmHg images have also been obtained.

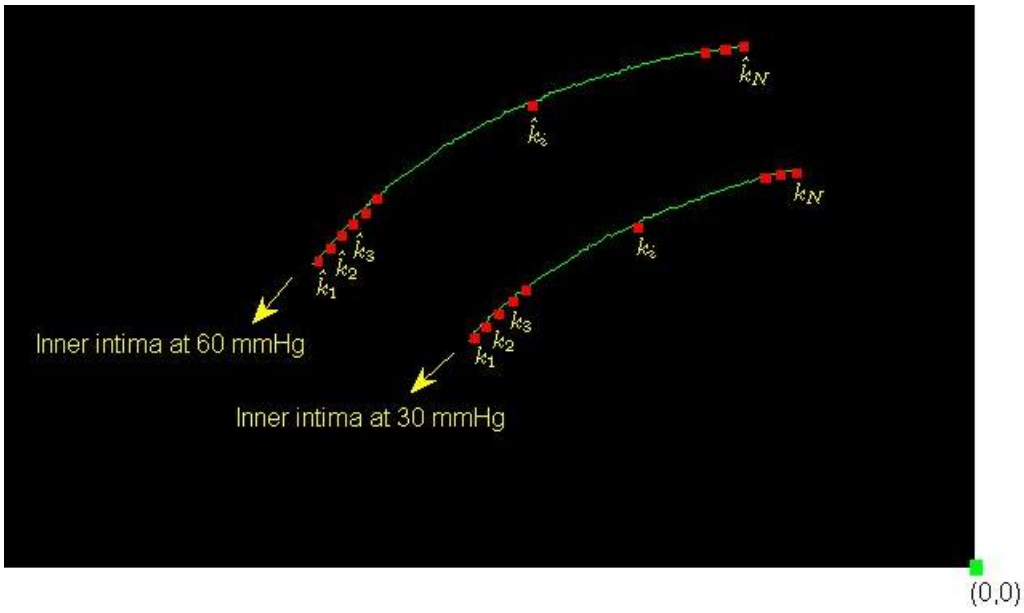

Figure 55: Inner boundary of intima at 30 and 60 mmHg with n pair of corresponding points

Having obtained boundary point correspondences between 30 & 60 mmHg images, the final step is by using the matched points between boundaries to estimate strain fields within the vessel wall. Due to the fact that the base pressure used in estimating those strain fields is 30 mmHg rather 0 mmHg[1], for the sake of clarity, instead of *strain*, the term *incremental strain* will be used from now on.

Because the force captured in the developed segmentation algorithm is the radial pressure, the incremental radial strain is actually of particular interest here. Although circumferential strain can also be obtained, it may not be as accurate and reliable as the radial strain is. Therefore, in the following how to compute a radial strain given the boundary point correspondences is explained. As an example, the inner and outer intima at 30 and 60 mmHg are considered. Referring to Figure 56, the points k_i and $\hat{k}_i$ are the matched points on the inner intima so are the points l_i and $\hat{l}_i$ on the outer intima, $\forall i = 1, \cdots, N$. Having connected k_i to l_i as well as their correspondences $\hat{k}_i$ to $\hat{l}_i$ as shown in Figure 56, now the estimation of incremental radial strain requires to determine how much the radial distance between k_i and l_i differs from the radial distance between $\hat{k}_i$ to $\hat{l}_i$. It is assumed that the x and y coordinates of k_i, l_i, $\hat{k}_i$ and $\hat{l}_i$ are given as follows: $k_i = (k_{ix}, k_{iy})$, $l_i = (l_{ix}, l_{iy})$, $\hat{k}_i = (\hat{k}_{ix}, \hat{k}_{iy})$, $\hat{l}_i = (\hat{l}_{ix}, \hat{l}_{iy})$. Also, $\Delta R_{k_i,l_i}$ and $\Delta \hat{R}_{\hat{k}_i,\hat{l}_i}$ represents the radial distances between i^{th} sample points of inner and outer intima before and after deformation, respectively (i.e., radial distance between k_i and l_i, and radial distance between $\hat{k}_i$ and $\hat{l}_i$, respectively).

Then, the incremental radial strain for the line segment between the i^{th} sample point of inner and outer intima can be computed as follows:

[1]As mentioned in Section 3.2, RF signals weren't collected at 0 mmHg, because that data would be unreliable due to the shrinkage of the artery harvested from the heart.

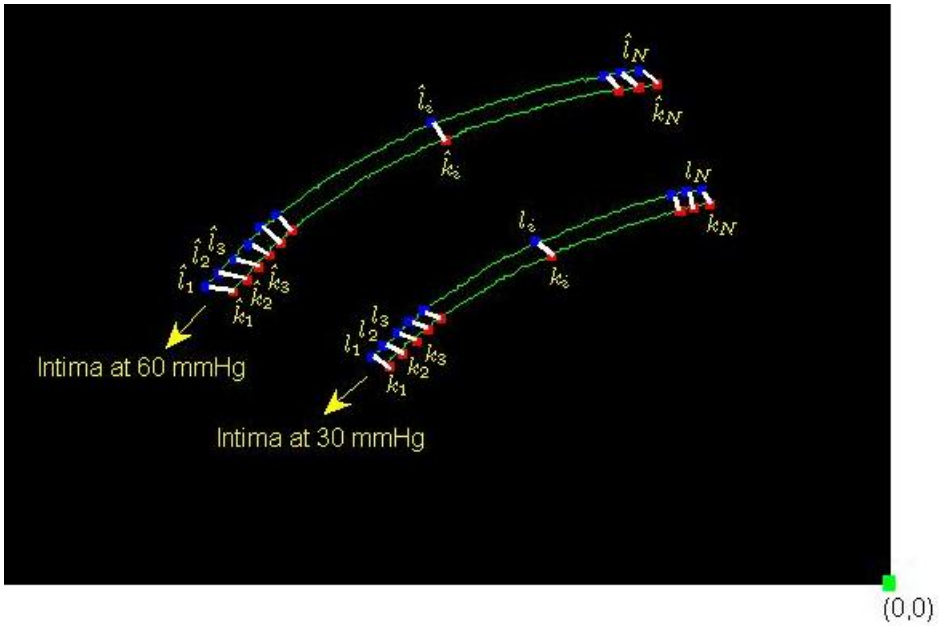

Figure 56: Intima at 30 and 60 mmHg with n pair of corresponding points on both inner and outer boundaries

$$\Delta\varepsilon_{rad}^{k_i,l_i} = \frac{\Delta\hat{R}_{\hat{k}_i,\hat{l}_i} - \Delta R_{k_i,l_i}}{\Delta R_{k_i,l_i}} = \frac{(R_{\hat{l}_i} - R_{\hat{k}_i}) - (R_{l_i} - R_{k_i})}{(R_{l_i} - R_{k_i})} \tag{32}$$
$$= \frac{\sqrt{\hat{l}_{ix}^2 + \hat{l}_{iy}^2} - \sqrt{\hat{k}_{ix}^2 + \hat{k}_{iy}^2} - \sqrt{l_{ix}^2 + l_{iy}^2} + \sqrt{k_{ix}^2 + k_{iy}^2}}{\sqrt{l_{ix}^2 + l_{iy}^2} - \sqrt{k_{ix}^2 + k_{iy}^2}}$$

where $R_{\hat{l}_i}$, $R_{\hat{k}_i}$, R_{l_i} and R_{k_i} are the radial distances of points $\hat{l}_i$, $\hat{k}_i$, l_i and k_i to the center, respectively. The numerator of Eq. 32 is equal to the difference between the radial displacements of l_i and k_i, showing how much the radial distance between those two points has changed from 30 to 60 mmHg. Dividing the radial distance change between l_i and k_i by the initial radial distance between them provides the incremental radial strain value.

After all of the line segments of intima shown in Figure 56 as well as all of the line segments of media, adventitia and fat that would be created in a similar way are assigned incremental radial strain values using Eqs. 32, incremental strain map can be created. In doing so, basically incremental radial strain fields of intima, media,

adventitia and fat are put together. The strain map of the coronary artery vessel wall corresponding to a pressure increase from 30 mmHg to 60 mmHg is given in Figure 57.

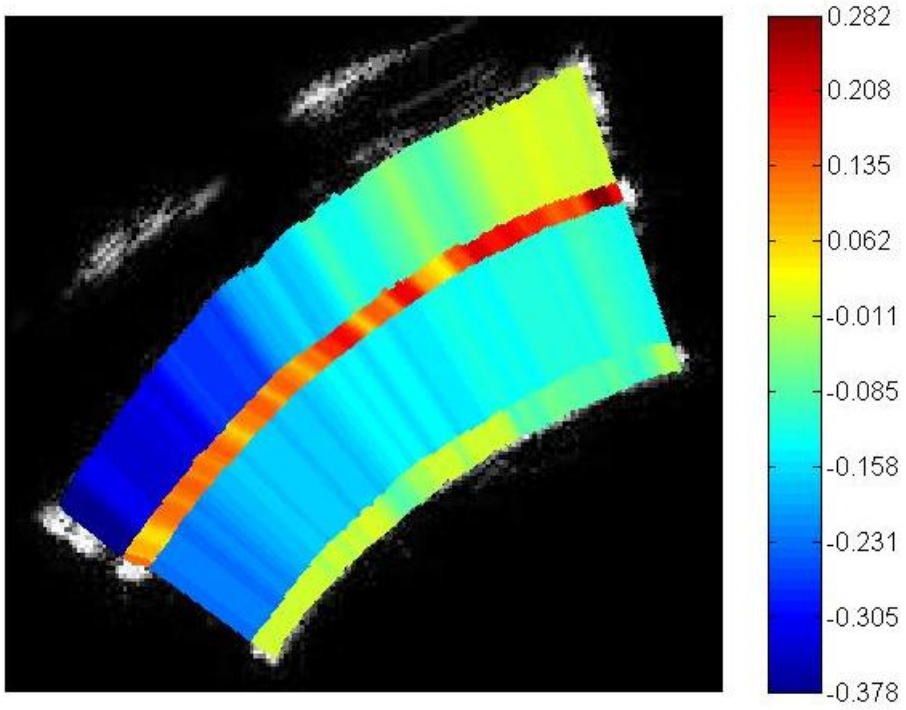

Figure 57: Incremental radial strain map of the coronary artery vessel wall for a pressure increase from 30 to 60 mmHg

As can be seen in Figure 57, the deformation field inside intima, media, adventitia and fat can be said to be smooth, that is, strain values are similar within along each boundary. However, strain values of one boundary differ from those of another one. While the incremental radial strain within the intima, media and fat is negative, the incremental radial strain within the adventitia turned out to be positive. Specifically, the strain values of the intima range approximately from 0 to -8%; strain values of the media range approximately from -8% to -20%; strain values of the adventitia range approximately from 0 to 28.2%; strain values of the fat range approximately from 0 to -37.8%.

The negative values obtained for the intima and media are indeed compatible with the results of the elastography studies done in the literature. As stated in Section 3.3, artery is compressed in the radial direction with increasing intraluminal pressure, resulting in negative radial strain field. However, the superiority of the above obtained results is that differences between the radial strain patterns of intima and media could be captured. Because in the other studies, as stated in Chapter 3, only lumen-intima and media-adventitia boundaries have been able to be detected, that is, intima-media boundary could not be detected, the differences between the strain patterns of intima and media are hardly captured. Also, again because of both the high resolution level of the images used and the effectiveness of the techniques developed, this work has been able to estimate radial strain values also within the adventitia. The above results show that for the case studied in this work the radial strain values within the adventitia turned out to be positive as opposed to those of intima and media.

Because the total thickness of the media and intima is much larger than that of adventitia, the negative strain values of media and intima outweigh the positive strain values of adventitia, resulting in a decrease in the total thickness of the artery vessel wall when pressurized. This result is indeed consistent with the general deformation behavior of an artery vessel wall that has been discussed in Section 3.3.

The obtained strain map that includes strain values as high as 28.2% and as low as -37.8% show that the developed technique provides size-independent deformation fields. Also since the length, angle or parallelism of the line segments (shown in Figure 56) for which strain values are estimated is not necessarily preserved as well as the deformations of neighbor line segments do not need to be similar implying that local stretching/compression is allowed, the obtained strain fields correspond to local rigid and non-rigid deformations. Finally, as mentioned above the resolution level of the strain map is very high due to the high resolution of the ultrasound images used, large

number of sample points taken (i.e., $N = 250$) as well as the effective segmentation techniques developed.

CHAPTER VI

CONCLUSIONS AND FUTURE WORK

In this thesis, high-resolution coronary artery vessel wall ultrasound images at different intraluminal pressures are formed, and a technique that provides robust segmentation and deformation estimation of the vessel wall is developed. The ultimate objective of this work is to encourage research efforts to provide the inverse problem community with more complete and accurate strain fields of the coronary vessel wall.

This thesis involves both experimental (i.e., RF data acquisition) and theoretical (i.e., image formation & processing) work. Due to the significant drawbacks of coherent and incoherent techniques (e.g., ability to capture only small and rigid strain patterns) discussed in Chapter 2, an image-based elastography technique is developed to estimate the strain fields within the vessel wall. In the image-based techniques, B-mode images are used; they can be either directly acquired from commercial ultrasound scanners or formed from RF signals after some image formation and processing techniques have been applied. While the former way is less time-consuming, due to the lack of commercial ultrasound machines with high sampling rate and frequency, the resolution of the acquired images will be low if this former way is followed. On the other hand, in the latter way the resolution depends on the frequency of the ultrasound transducer and sampling rate of the oscilloscope used as well as the way images are formed from RF signals (i.e., which image formation and processing techniques are used). In either way, however, the resolution values obtained in the literature are not good enough to clearly see all of the five boundaries of the vessel wall, namely, lumen-intima (i.e., inner intima), intima-media (i.e., outer intima), media-adventitia (i.e., inner adventitia), adventitia-fat (i.e., outer adventitia) and the very outer fat

boundary.

Therefore, the first step in this work is to design an experimental setup for RF data acquisition that involves a transducer with high-frequency, an oscilloscope with high sampling rate, a pulser-receiver, a computer and an in-vitro artery culture. The second step is then to develop an image formation algorithm to obtain high-resolution ultrasound images from the collected RF signals. Chapter 3 provides the details about experimental setup, data acquisition and image formation.

Having formed high-resolution ultrasound images at different pressures, a segmentation algorithm is developed step-by-step to formally detect all five boundaries of the ultrasound images. The main motivations behind this "boundary-based" approach are as follows. First, it provides much more reliable strain estimations than any other approach could as long as the boundaries are accurately detected. Second, it exploits the high resolution level of the formed images in which both inner and outer boundaries of the intima, media and adventitia can be detected. For example, comparing the displacements of two boundary points, one of them on the inner and the other one on the outer boundary of a layer, provides information about how much the radial distance between those two points changes during deformation, resulting in a local radial strain estimate across the corresponding layer. Without either high-resolution images or "boundary-based" approach, it would be difficult to determine the strain distribution across each layer.

Chapter 4 involves step-by-step development of the segmentation algorithm tailored for the high-resolution noisy coronary vessel wall ultrasound images formed. Specifically, the developed segmentation algorithm is based on *geodesic active contours* that are very powerful in extracting features from images and eliminate the limitations of snakes. To make the segmentation robust to noise present in the images, phase information is added to the classical geodesic active contour model and then to even further increase the robustness region-based information is incorporated

as well. Finally, to increase the stability and accuracy of the segmentation, a priori information, that is, elliptical shape of the arteries, is utilized and elliptical deformable template-based geodesic active contour algorithm is implemented. Then, the boundary refinement step that follows even makes the deformable contours better fit the edges. Unlike the previously developed segmentation-based methods, this developed technique uses neither optical flow nor mechanical constitutive assumptions. Also, it implicitly provides boundary point correspondences between boundaries. Using those matched points on the corresponding boundaries of the images, Chapter 5 shows how to estimate radial strain fields within the vessel wall.

6.1 Thesis Contributions

The main contributions of this thesis are as follows:

- High-resolution coronary vessel wall ultrasound images are acquired, where both radial and circumferential resolutions are around 10 μm. To date, the best values reported in the literature have been around 50 μm.

- For the first time, all of the five boundaries of a coronary artery vessel wall, namely, lumen-intima, intima-media, media-adventitia, adventitia-fat and outer fat, are able to be detected. In the literature, to date, only lumen-intima and media-adventitia boundaries have been detected.

- A new image segmentation-based elastography approach is presented. A segmentation algorithm tailored for the coronary vessel wall ultrasound images is developed.

- Phase knowledge is incorporated into the geodesic active contour model. Specifically, a novel stopping function involving phase-based and amplitude-based terms is designed. It is shown that when only amplitude-based term (as in the classical geodesic active contour model) is used, the curve couldn't completely

reach the target boundary unless the area where the curve evolves has fairly low amount of noise. Although using only phase-based term makes the segmentation much more robust to noise and provides the curve to reach the target boundary, with only phase-based term (due to its weakened stopping power) the curve couldn't stop at the target boundary unless the distance between the target and next farther boundary is fairly large. It is shown that in the cases where neither phase-based nor amplitude-based term works by itself accurate boundary detection can be achieved by adjusting the relative weight between two terms.

- Region-based information is added into the geodesic active contour model having new stopping function. It is shown that the incorporation of the region information has increased the robustness of the model and made it much easier to deal with the weighting coefficients.

- For the first time in the elastography literature, a shape information of the coronary vessel wall is utilized by being added as a constraint into the geodesic active contour model, resulting in a segmentation algorithm specifically designed for coronary arteries. It is shown that this algorithm, which is based on the optimization of the elliptical deformable template, not only allows accurately detecting the boundaries but also implicitly provides the boundary point correspondences.

- The way radial strains are calculated from the matched boundary points is explicitly outlined, and for the first time the differences between the radial strain patterns of intima, media and adventitia are captured.

- The formation of the high-resolution images as well as the effective segmentation, boundary point matching and deformation estimation processes for the

first time provide the inverse problem community with high-resolution, size-independent, non-rigid and local radial strain distributions within the coronary artery vessel wall.

6.2 Future Research Directions

The future research directions are as follows:

- As shown in Section 4.3, although elliptical deformable template provides the evolving curves to fit the boundaries very closely for 30 and 60 mmHg images, it doesn't work well for 90 mmHg image especially in the detection of the adventitia. Therefore, to be able to accurately segment coronary vessel wall images at high pressures (i.e., 90 mmHg or more), there is a need to use higher degree polynomial as a shape constraint of the template.

- Since porcine coronary arteries have been used for all of the computations presented in this thesis, there is also a need to work on human coronary arteries to show the applicability of this work. Also, porcine coronary arteries generally do not include any plaque composition while human arteries usually do. In other words, using human coronary arteries would provide an opportunity for the developed technique to be tested with the diseased arteries. In the presence of plaque, the curve to be evolved for the detection of lumen-intima boundary would be able to detect the plaque, which is located on the inner intima. Strain values estimated across the intima help determine the location and composition of the plaque. However, it should be noted that in the presence of plaque higher order polynomial would most likely be required as a shape constraint in the deformable template because of the possible irregular shape of the plaque.

- Although this work provides high-resolution, non-rigid, size-independent and local incremental radial strain fields, to estimate complete deformation pattern

of the coronary artery vessel wall the developed technique needs to be improved so that circumferential strains can also be captured. Also, its extension into 3-D would result in much more realistic deformation estimations.

- Having solved the forward problem, the next step is to deal with the inverse problem and construct the elastic distributions consistent with obtained strain field. As mentioned in Chapter 1, it requires the estimation of the local stress throughout the vessel wall by using non-linear optimization methods, regularization techniques and/or finite element model.

APPENDIX A

FACILITIES AND EQUIPMENT USED

The specifications of the equipments (whose schematic diagram is shown in Figure 2) used in this research are given as follows:

- **Transducer:** Valpey Fisher 50 MHz transducer (VF 412), which has a spherical focus produced with aid of concave lens, is used to transmit and collect Radio Frequency (RF) data (see Figure 58). Although spherical focus improves sensitivity to small flaws, such a concave structure results in air-bubble formation when the transducer is placed in an organ culture system. Manual intervention with a significant care is required to remove the bubble formation. Also, a microdot connector seen in Figure 58 connects the transducer to the pulser/receiver. Specifications of the transducer are given in Table 3.

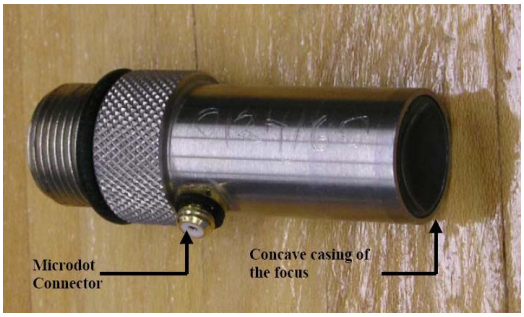

Figure 58: Transducer

- **Pulser-Receiver:** Panametrics 5900 computer-controlled pulser-receiver that is designed for high frequency ultrasonic testing is chosen basically due to its high bandwidth of 200 MHz and RS-232 interface. Some of the specifications of this pulser-receiver are given in Table 4.

Table 3: Specifications of the transducer used to transmit and receive ultrasound waves

VF 412 Transducer	
Frequency	50 MHz
Focal Length	12.7 mm
Element Diameter	6.35 mm
f#	2

Table 4: Specifications of the pulser-receiver used to provide high-voltage pulse and signal conditioning

Panametrics 5900 Pulser-Receiver	
Mode	Pulse Echo
Pulse Repetition Frequency	200 Hz
Gain	54 dB
Maximum Bandwidth	200 MHz
Damping	50 ohms
Available Pulse Energy	32 μJ

- **Oscilloscope:** Agilent 54642A model oscilloscope is used to digitize and display received RF signals. Some of its specifications are given in Table 5. This oscilloscope is chosen especially due to its high-sampling rate and bandwidth, which allow seeing the details of RF signals and subsequently forming the high-resolution images. Another factor in using Agilent 54642A is its RS-232 and GPIB (IEEE 488) interfaces, which provide the oscilloscope to be connected to the Pentium IV computer.

Table 5: Specifications of the oscilloscope used to sample and display RF signals

Agilent 54642A Oscilloscope	
Bandwidth	500 MHz
Maximum Sampling Rate	2 Gsa/s
Maximum Memory	8 MB
Channels	2

- **Minilab 1008:** To control the movements of the artery, Minilab 1008, a USB-based data acquisition device, is used.

- **Peristaltic Pump:** The output of a Master flex 7520 peristaltic pump is used to develop pressure in the closed system containing the coronary artery.

- **Porcine Coronary Artery**: Porcine hearts are obtained from a local farm, namely, Hollifield Farms in Covington, GA and carried to Georgia Tech within 2 hours of drive time. The hearts are preserved on ice, and the right coronary arteries are excised from intact hearts approximately after 3-4 hours of sacrifice.

APPENDIX B

RF DATA ACQUISITION SYSTEM

The schematic showing how RF signals are acquired is given in Figure 59.

While transducer is fixed, the artery is rotated about its axis to scan a sector of the proximal wall of the artery (for the configuration given in Figure 59 the blue cross-sections are parts of the proximal wall, which is closer to the transducer than the distal wall on the other side of the lumen). Here, to determine the rotation angle, first, the beam diameter shown in the figure needs to be computed using Eq. 33 [66]:

$$BD = \frac{1.02 \times F \times c}{f \times D} \tag{33}$$

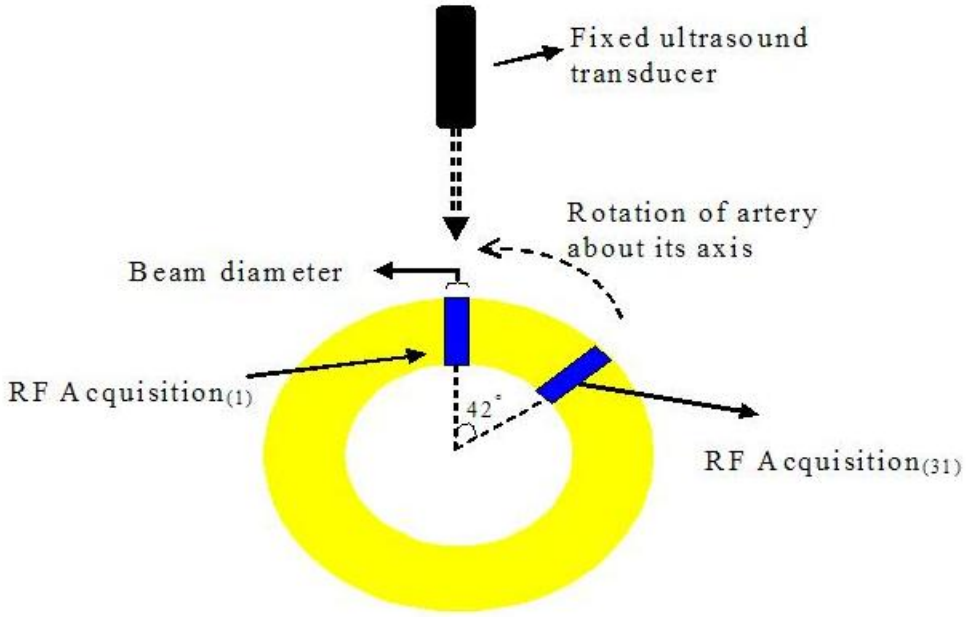

Figure 59: RF data acquisition

where BD is the -6 dB beam diameter, c is the sound velocity in soft tissue (i.e., 1540 m/s), and F is the focal length, f is the frequency and D is the element diameter of the transducer. When the values given in Appendix A are used in Eq. 33, the beam diameter is calculated to be 0.063 mm.

In this experiment, the outer radius of the artery (i.e., the distance between the very outer boundary and center of the artery) harvested from the heart is 1.3 mm. Dividing the perimeter of the artery by the beam diameter gives the number of turns required to totally scan the artery, that is, $\frac{2\pi 1.3}{0.063} \times 2 = 256$ (multiplication by 2 results from the fact that consecutive scans are 50% overlapped). Then, the rotation angle (i.e., the angle between the consecutive RF data acquisitions) is calculated to be $\frac{360}{256} = 1.4°$. Since, as mentioned before, for the purposes of this research, there is no need to scan the whole artery, 31 RF data acquisitions are taken by rotating the artery 1.4° at every step. At the end of the experiment, as shown in Figure 59, 42° sector of the artery is scanned. However, here, as mentioned in Subsection 3.2, before each rotation, the whole set of RF data (i.e., signals at 30, 60 and 90 mmHg) are acquired for the corresponding 1-D cross-section of the artery[1]. For example, assuming that Figure 59 corresponds to 30 mmHg case, when $RFAcquisition_{(1)}$ is taken, instead of rotating the artery and taking $RFAcquisition_{(2)}$, the artery is pressurized to 60 and 90 mmHg to take $RFAcquisition_{(1)}$ also at those pressures. Then, the artery is rotated and $RFAcquisition_{(2)}$ is taken. As explained in detail in Section 3.2, this way of data acquisition provides the collected RF signals at different pressures to be much more correlated with each other.

[1]In Figure 59, the blue cross-sections each of which represents a single RF line are considered to be 1-D for the sake of explanation. When all collected blue cross-sections are put together, 2-D cross-section of the artery is obtained.

APPENDIX C

ATTENUATION CORRECTION & INTERPOLATION OF RF SIGNALS

In soft tissues, sound is attenuated at the rate of 0.5 decibel (dB) per centimeter (cm) per million hertz (MHz) [24]. To compute the attenuation coefficient for each of 2000 sampled points in the recorded RF signals, there is a need to find the corresponding distance between two consecutive points. Using Eq. 1 and the time difference between consecutive points, which is 1 ns, the distance can be computed as follows: $d = \frac{c \times t}{2} = \frac{(1540m/s) \times (1 \times 10^{-}9s)}{2} = 0.77\ \mu m$. In other words, the wave travels 0.77 μm distance (one-way) between adjacent points. However, as far as the attenuation (0.5 dB per cm per MHz) is concerned, two-way distance, that is, $0.77 \times 2 = 1.54\ \mu m$ needs to be used. Then, using 0.5 $dB/(cm \cdot MHz)$, the attenuation between adjacent points in terms of dB is: $0.5 \times 1.54 \times 10^{-4} \times 50 = 3.85 \times 10^{-3}$. In other words, if the amplitude of the wave reflected from a point inside the tissue is 1 V when it reaches the transducer, the amplitude of the same wave reflected from the next point would be approximately 0.9992 V (dB can be converted to real amplitude decay using $10 \log (V_1/V_2) = 3.85 \times 10^{-3}$). Thus, the amplitude of the latter point needs to be multiplied by 1.0008 to compensate the attenuation loss ($0.9992 \times 1.0008 = 1$). As a result, to correct the attenuation losses and make the amplitudes of 2000 points (in an RF line) comparable to each other, if the point is i^{th} point within its corresponding RF line, its amplitude value needs to be multiplied by $1.0008^{(i-1)}$.

After the attenuation losses are compensated and scan conversion is performed as explained in Section 3.3, for the sake of display and resolution interpolation is performed among 31 RF acquisitions collected. As discussed in Appendix B, the angle

between two consecutive RF acquisitions is 1.4°. Interpolating these RF acquisitions would make this angle smaller, resulting in better circumferential resolution. For this purpose, 2-D linear interpolation is performed so that the angle between adjacent lines would end up being 0.28°. This means, between two consecutive RF acquisitions are generated 4 additional RF acquisitions, resulting in 151 RF acquisitions instead of 31.

APPENDIX D

DETAILS OF THE IMAGE FORMATION

To get high resolution values, in the digitization of RF signals the sampling rate of 1 Gsa/s, which corresponds to the time scale of 0.2 μs per division, was used. This implies that each RF acquisition corresponds to a signal with duration 2 μs (since there are 10 divisions on the oscilloscope screen). However, the drawback of working with very small signal duration is that the useful part of the RF signal (coming from the vessel wall) might leave the screen when the artery is rotated or pressurized. In those cases, there would be a need to adjust the X-shift of the oscilloscope. Indeed, in the experiment it turned out that the first 10 RF acquisitions corresponded to the time period of 15.5-17.5 μs, the next 10 acquisitions to 15.4-17.4 μs, and the last 11 RF acquisitions to 15.2-17.2 μs[1]. As a result, three group of RF signals were collected (the X-shift was not needed to be adjusted while pressurizing the artery). In the image formation process, these time period differences resulting from the changes in the X-shift were corrected. From Eq. 1 ($t = \frac{2d}{c}$), the time shift of $t = 0.1$ μs between the first and second group would correspond to the distance of 77 μm, or equivalently 10 pixels since the distance between adjacent pixels in the radial direction is 7.7 μm.

Each of those 31 RF acquisitions involves 2000 data points, or equivalently 200 pixels, and is aligned in the radial direction. Those 200 pixels within each RF acquisition can be given a radial value that indicates the distance between the pixels and the center of the artery. Those values would be used to convert the polar coordinate system, in which all RF acquisitions have initially been collected, to cartesian

[1]As for the interpolation, the new lines that would be interpolated between the first 10 RF acquisitions also corresponded to the time period of 15.5-17.5 μs, between the next 10 RF acquisitions to 15.4-17.4 μs, and between the last 11 RF acquisitions to 15.2-17.2 μs.

coordinate system. Then, if radial values from r to $r + 199$ are given to the first 10 RF acquisitions collected, the next 10 acquisitions would have values from $r + 10$ to $r + 209$, and the last 11 from $r + 30$ to $r + 229$.

Here, the question is what the value of r is. To answer this, there is a need to estimate where the origin (i.e., estimation of the center of the artery or middle point of the lumen) is located. Since no interface exists at the origin, it is not possible to differentiate the part of the signal that corresponds to the origin on the oscilloscope screen. However, the beginning of the distal wall and the ending of the proximal wall are able to be detected on the oscilloscope screen. Indeed, in the experiment, during the acquisition of first 10 signals, the former one was seen at 20.4 μs, while the latter one at 17 μs. Thus, assuming that the center of the artery is located at the middle of the proximal and distal walls (i.e., lumen radius is same within a 2-D cross-section), the origin would have been seen at 18.7 μs. After a simple computation, it can be found that the sampled data point at 17.5 μs (the very right sampled point of the first 10 acquired signals whose pixels have radial values from r to $r + 199$) would be 924 μm away from the center of the artery. That point whose radial value was assigned r is the closest to the center among all data points collected. Then, using the distance between adjacent pixels, i.e., 7.7 μm, r would be equal to $924/7.7 = 120$.

APPENDIX E

IMPLEMENTATION DETAILS OF THE EDGE-BASED SEGMENTATION ALGORITHM

The implementation steps of the edge-based segmentation algorithm are as follows:

- An initial curve C is selected
- The level set function $\psi(i, j, t)$ is created by using signed distance function. The value of ψ at (i, j) is selected as the minimum distance of (i, j) from C. The sign of the level set value depends on the evolution direction of the curve. If the curve is to be evolved inwards (i.e., the curve shrinks), the sign should be selected as positive if (i, j) is outside the curve and selected as negative if the point is inside the curve. On the other hand, if the curve is going to evolve toward the outside (i.e., the curve expands), the sign should be selected as positive if (i, j) is inside the curve and negative if the point is outside the curve. The logic behind this selection is as follows. In the beginning, for both case, some pixels in the image have positive level set values, some have negative and some zero. While the partial differential equation in Eq. 7 is run, there is a trend such that level set values of each pixel increases. In other words, zero level set contour moves toward the region where previously the negative level set values were located. Thus, if the curve (involving pixels with zero level set value) is to be evolved inwards, the level set values should be initialized so that if the point is outside the curve, its sign is positive, and if it is inside the curve, its sign is negative. The opposite of this is true if the curve is to be evolved outwards.

- The Hilbert transform of the columns and rows of the image is taken, and the phase angles θ_x and θ_y are computed for each pixel.
- The magnitude of the gradient of the image ($\|\nabla I\|$) is computed by using central difference approximations.
- λ is set with a value between 0 and 1.
- The stopping function given in Eq. 9 and its gradient are computed.
- The ψ function is updated with the following equation:

$$\psi(t + \Delta t) = \psi(t) + \Delta t(\phi\|\nabla\psi\|\kappa + \nabla\phi\cdot\nabla\psi) \tag{34}$$

- To make the scheme stable, Δt is set (for Δx =1) so that $\Delta t < 0.5$ and $\Delta t < 1/max(\|\nabla\phi\|)$
- The points of the evolving contour are determined by finding the points for which $\psi = 0$
- The zero crossings of the level set function are determined by analyzing a small neighborhood of each point within the image. For each point 2×2 neighborhood is defined. If there are at least one negative and one positive point among four neighbors, a zero-crossing occurs within the neighborhood (2×2 square). A linear interpolation of the four points helps determine the exact location of the zero crossing.
- A binary matrix M which has a value of 1 at the pixels whose neighborhood includes zero crossing of the level set function is constructed.
- The amount of change in the shape of the contour is tracked by comparing the matrix M among iterations.

- Along with the zero level function, other level set functions also evolve. In order to make each level set evolve with the same speed, at each iteration after determining the points on the curve (i.e., zero crossings of the level set function), for each of the other pixels the point which is on the curve and closest to that pixel among all points on the curve is determined. Then, the values of ϕ, $\nabla\phi_x$ (gradient of the stopping function in the x direction) and $\nabla\phi_y$ (gradient of the stopping function in the y direction) at the point on the curve are copied to the pixel closest to that point.

- To make the implementation faster, the grid area is made smaller during the iteration as long as it is guaranteed that its size is enough for the curve to evolve.

- In every 300 iterations, the corresponding situation of the curve is displayed.

To solve Eq. 34, the term inside the parenthesis needs to be computed whenever ψ is updated. As mentioned before, the first part, $\phi\|\nabla\psi\|\kappa$, is called the diffusion term, while the second part, $\nabla\phi\cdot\nabla\psi$, is called the transport term. For the diffusion term, the central difference approximations are used. Curvature (κ) in the diffusion term is defined as follows:

$$\kappa = div(\frac{\nabla\psi}{\|\nabla\psi\|}) = \frac{\psi_x^2\psi_{yy} - 2\psi_x\psi_y\psi_{xy} + \psi_y^2\psi_{xx}}{(\psi_x^2 + \psi_y^2)^{3/2}}) \tag{35}$$

where (for the pixel (i, j))

$$\psi_x^{i,j} = (\psi^{i+1,j} - \psi^{i-1,j})/2,$$
$$\psi_y^{i,j} = (\psi^{i,j+1} - \psi^{i,j-1})/2,$$
$$\psi_{xx}^{i,j} = \psi^{i+1,j} - 2\psi^{i,j} + \psi^{i-1,j},$$
$$\psi_{yy}^{i,j} = \psi^{i,j+1} - 2\psi^{i,j} + \psi^{i,j-1},$$
$$\psi_{xy}^{i,j} = (\psi^{i+1,j+1} - \psi^{i+1,j-1} - \psi^{i-1,j+1} + \psi^{i-1,j-1})/4.$$

Thus, using the above central difference approximations and Eq. 9, the diffusion term in Eq. 34 is implemented as follows:

$$\phi\|\nabla\psi\|\kappa = \phi\frac{\psi_x^2\psi_{yy} - 2\psi_x\psi_y\psi_{xy} + \psi_y^2\psi_{xx}}{(\psi_x^2 + \psi_y^2)}$$

On the other hand, the transport term in Eq. 34 is computed as follows:

$$\nabla\phi\cdot\nabla\psi = max(\phi_x, 0)\psi_{+x} + min(\phi_x, 0)\psi_{-x} + max(\phi_y, 0)\psi_{+y} + min(\phi_y, 0)\psi_{-y}$$

where (for the pixel (i, j))

$$\psi_{+x}^{i,j} = \psi^{i+1,j} - \psi^{i,j},$$
$$\psi_{-x}^{i,j} = \psi^{i,j} - \psi^{i-1,j},$$
$$\psi_{+y}^{i,j} = \psi^{i,j+1} - \psi^{i,j},$$
$$\psi_{-y}^{i,j} = \psi^{i,j} - \psi^{i,j-1},$$

as well as ϕ_x and ϕ_y are the gradients of ϕ in x and y directions, respectively. Combining the diffusion and transport terms, the level set equation given in Eq. 34 is solved.

REFERENCES

[1] Alam, K. and Ophir, J., "Reduction of signal decorrelation from mechanical compression of tissues by temporal stretching: Applications to elastography," *Ultrasound in Medicine and Biology*, vol. 23, no. 1, pp. 95–105, 1997.

[2] Alam, K., Ophir, J., and Konofagou, E., "An adaptive strain estimator for elastography," *IEEE Transactions on Ultrasonics, Ferroelectrics, and Frequency control*, vol. 45, no. 2, pp. 461–472, 1998.

[3] Alam, S., Lizzi, F., Varghese, T., Feleppa, E., and Ramachandran, S., "Adaptive spectral strain estimators for elastography," *Ultrasonic Imaging*, vol. 26, no. 3, pp. 131–149, 2004.

[4] Amini, A., Weymouth, T., and Jain, R., "Using dynamic programming for solving variational problems in vision," *IEEE Transactions on Pattern Analysis and Machine Intelligence*, vol. 12, no. 9, pp. 855–867, 1990.

[5] Baldewsing, R., de Korte, C., Schaar, J., Mastik, F., and Van der Steen, A., "A finite element model for performing intravascular ultrasound elastography of human atherosclerotic coronary arteries," *Ultrasound in Medicine and Biology*, vol. 30, no. 6, pp. 803–813, 2004.

[6] Baldewsing, R., Mastik, F., Schaar, J., Serruys, P., and Van der Steen, A., "A finite element model for performing intravascular ultrasound elastography of human atherosclerotic coronary arteries," *Ultrasound in Medicine and Biology*, vol. 31, no. 12, pp. 1631–1645, 2005.

[7] Bascle, B. and Deriche, R., "Region tracking through image sequences," in *IEEE International Conference in Computer Vision*, pp. 302–307, 1995.

[8] Berger, M., "Snake growing," in *First European Conference on Computer Vision*, pp. 570–572, 1990.

[9] Bogen, D. and McMahon, T., "Do cardiac anuerysms blow out?," *Biophysical Journal*, vol. 27, no. 2, pp. 301–316, 1979.

[10] Bohs, L., Friemel, B., and Trahey, G., "Experimental velocity profiles and volumetric flow via two-dimensional speckle tracking," *Ultrasound in Medicine and Biology*, vol. 21, no. 7, pp. 885–898, 1995.

[11] Bridal, S., Correas, J., Saied, A., and Laugier, P., "Milestones on the road to higher resolution, quantitative, and functional ultrasonic imaging," *Proceedings of the IEEE*, vol. 91, no. 10, pp. 1543–1561, 2003.

[12] Brusseau, E., Fromageau, J., Finet, G., Delachartre, P., and Vray, D., "Axial strain imaging of intravascular data: Results on polyvinyl alcohol cryogel phantoms and carotid artery," *Ultrasound in Medicine and Biology*, vol. 27, no. 12, pp. 1631–1642, 2001.

[13] Brusseau, E., Korte, C., Mastik, F., Schaar, J., and Van der Steen, A., "Fully automatic luminal contour segmentation in intracoronary ultrasound imaging-a statiscal approach," *IEEE Transactions on Medical Imaging*, vol. 23, no. 5, pp. 554–566, 2004.

[14] Burton, A., "Relation of structure to function of the tissues of the walls of blood vessels," *Physiological Reviews*, vol. 34, no. 4, pp. 619–642, 1954.

[15] Burton, A., *Physical principles of circulatory phenomena: The physical equilibria of the heart and blood vessels*. Handbook of Physiology, American Physiological Society and Oxford University Press, 1962.

[16] Caselles, V., Kimmel, R., and Sapiro, G., "Geodesic active contours," *International Journal of Computer Vision*, vol. 22, no. 1, pp. 61–79, 1997.

[17] Chan, R., Kaufhold, J., Karl, W., Lees, R., and Castañon, D., "A variational energy approach for estimating vascular structure and deformation from b-mode ultrasound imagery," in *The IEEE International Conference on Image Processing*, pp. 160–163, 2000.

[18] Cheng, G., Loree, H., Kamm, R., Fishbein, M., and Lee, R., "Distribution of circumferential stress in ruptured and stable atherosclerotic lesions: A structural analysis with histopathological correlation," *Circulation*, vol. 87, no. 4, pp. 1179–1187, 1993.

[19] Choi, C., Skovoroda, A., Emelianov, S., and O'Donnell, M., "Strain imaging of vascular pathologies using a compliant balloon catheter," in *Proceedings of the IEEE Ultrasonics Symposium*, pp. 1771–1774, 2000.

[20] Christensen, D., *Ultrasonic Bioinstrumentation*. John Wiley & Sons, 1988.

[21] Cohen, B. and Dinstein, I., "New maximum likelihood motion estimation schemes for noisy ultrasound images," *Pattern Recognition*, vol. 35, no. 2, pp. 455–463, 2002.

[22] Cohn, N., Emelianov, S., Lubinski, M., and O'Donnell, M., "An elasticity microscope. part 1: Methods," *IEEE Transactions on Ultrasonics, Ferroelectrics, and Frequency control*, vol. 44, no. 6, pp. 1304–1319, 1997.

[23] Cohn, N., Emelianov, S., Lubinski, M., and O'Donnell, M., "An elasticity microscope. part 2: Experimental results," *IEEE Transactions on Ultrasonics, Ferroelectrics, and Frequency control*, vol. 44, no. 6, pp. 1320–1331, 1997.

[24] Curry, R. and Tempkin, B., *Ultrasonography: An introduction to normal structure and functional anatomy*. W.B. Saunders Company, 1995.

[25] Das, B. and Banerjee, S., "Inertial snake for contour detection in ultrasonography images," *IEE Proceedings Vision, Image and Signal Processing*, vol. 151, no. 3, pp. 235–240, 2004.

[26] de Korte, C., Cèspedes, E., Van der Steen, A., and Lancèe, C., "Intravascular elasticity imaging using ultrasound-feasibility studies in phantoms," *Ultrasound in Medicine and Biology*, vol. 23, no. 5, pp. 735–746, 1997.

[27] de Korte, C., Pasterkamp, G., Van der Steen, A., Woutman, H., and Bom, N., "Characterization of plaque components with intravascular ultrasound elastography in human femoral and coronary arteries in vitro," *Circulation*, vol. 102, no. 6, pp. 617–623, 2000.

[28] de Korte, C. and Van der Steen, A., "Intravascular ultrasound elastography: An overview," *Ultrasonics*, vol. 40, no. 1, pp. 859–865, 2002.

[29] de Korte, C., Van der Steen, A., Cèspedes, E., G., P., Carlier, S., Mastik, F., Schoneveld, A., Serruys, P., and Bom, N., "Characterization of plaque components and vulnerability with intravascular ultrasound elastography," *Physics in Medicine and Biology*, vol. 45, no. 6, pp. 1465–1475, 2000.

[30] de Korte, C., Van der Steen, A., Cèspedes, E., and Pasterkamp, G., "Intravascular ultrasound elastography in human arteries: Initial experience in vitro," *Ultrasound in Medicine and Biology*, vol. 24, no. 3, pp. 401–408, 1998.

[31] Doyley, M., Meaney, P., and Bamber, J., "Evaluation of an iterative reconstruction method for quantitative elastography," *Physics in Medicine and Biology*, vol. 45, no. 6, pp. 1521–1540, 2000.

[32] Golemati, S., Sassano, A., Lever, M., Bharath, A., Dhanjil, S., and Nicolaides, A., "Carotid artery wall motion estimated from b-mode ultrasound using region tracking and block matching," *Ultrasound in Medicine and Biology*, vol. 29, no. 3, pp. 387–399, 2003.

[33] Gosline, J., "The elastic properties of rubber-like proteins and highly extensible tissues," in *The Mechanical Properties of Biological Materials*, pp. 331–357, Symposium of the Society for the Experimental Biology, Cambridge University Press, 1980.

[34] Gunn, S. and Nixon, M., "A robust snake implementation: A dual active contour," *IEEE Transactions on Pattern Analysis and Machine Intelligence*, vol. 19, no. 1, pp. 63–68, 1997.

[35] Hamilton, J. and O'Donnell, M., "High frequency ultrasound imaging with optical arrays," *IEEE Transactions on Ultrasonics, Ferroelectrics, and Frequency control*, vol. 45, no. 1, pp. 216–235, 1998.

[36] Han, L., Noble, A., and Burcher, M., "The elastic reconstruction of soft tissues," in *Proceedings of the IEEE International Symposium on Biomedical Imaging*, pp. 1035–1038, 2002.

[37] Horn, B. and Schunck, B., "Determining optical flow," *Artificial Intelligence*, vol. 17, no. 1, pp. 185–203, 1981.

[38] Hoyt, K., Forsberg, F., and Ophir, J., "Analysis of a hybrid spectral strain estimation technique in elastography," *Physics in Medicine and Biology*, vol. 51, no. 2, pp. 197–209, 2006.

[39] Kallel, F. and Bertrand, M., "Tissue elasticity reconstruction using linear perturbation method," *IEEE Transactions on Medical Imaging*, vol. 15, no. 3, pp. 299–313, 1996.

[40] Kantor, B., Ashai, K., Holmes, D., and Schwartz, R., "The experimental animal models for assessing treatment of restenosis," *Cardiovascular Radiation Medicine*, vol. 1, no. 1, pp. 48–54, 1999.

[41] Kass, M., Witkin, A., and Terzopoulos, D., "Snakes: Active contour models," *International Journal of Computer Vision*, vol. 1, no. 4, pp. 321–331, 1988.

[42] Kichenassamy, S., Kumar, A., Olver, P., Tannenbaum, A., and Yezzi, A., "Gradient flows and geometric active contour models," in *IEEE International Conference in Computer Vision*, pp. 810–815, 1995.

[43] Konofagou, E. and Ophir, J., "A new elastographic method for estimation and imaging of lateral displacements, lateral strains, corrected axial strains and poisson's ratios in tissues," *Ultrasound in Medicine and Biology*, vol. 24, no. 8, pp. 1183–1199, 1998.

[44] Konofagou, E., Varghese, T., Ophir, J., and Alam, S., "Power spectral strain estimators in elastography," *Ultrasound in Medicine and Biology*, vol. 25, no. 7, pp. 1115–1129, 1999.

[45] Kovalski, G., Beyar, R., Shofti, R., and Azhari, H., "Three-dimensional automatic quantitative analysis of intravascular ultrasound images," *Ultrasound in Medicine and Biology*, vol. 26, no. 4, pp. 527–537, 2000.

[46] Lacaze, E., Michau, S., and Mauchamp, P., "20 mhz ultrasound array for medical imaging: From design to image evaluation," in *Proceedings of the IEEE Ultrasonics Symposium*, pp. 1139–1142, 2001.

[47] Lockwood, G., Turnbull, D., Christopher, D., and Foster, F., "Beyond 30 mhz: Applications of high-frequency ultrasound imaging," *IEEE Engineering in medicine and Biology*, vol. 15, no. 6, pp. 60–71, 1996.

[48] Loree, H., Kamm, R., Stringfellow, R., and Lee, R., "Effects of fibrous cap thickness on peak circumferential stress in model atherosclerotic vessels," *Circulation Research*, vol. 71, no. 4, pp. 850–858, 1992.

[49] Lorigo, L., Faugeras, O., Grimson, W., Keriven, R., Kikinis, R., Nabavi, A., and Westin, C., "Curves: Curve evolution for vessel segmentation," *Medical Image Analysis*, vol. 5, no. 3, pp. 195–206, 2001.

[50] Lubinski, M., Emelianov, S., Raghavan, K., Yagle, A., Skovoroda, A., and O'Donnell, M., "Lateral displacement estimation using tissue incompressibility," *IEEE Transactions on Ultrasonics, Ferroelectrics, and Frequency control*, vol. 43, no. 2, pp. 247–256, 1996.

[51] Mahajan, V., "Ultrasonic elastography measurements of the mechanical properties of porcine coronary vessel walls," Master's thesis, Georgia Institute of Technology, 2005.

[52] Malladi, R., Sethian, J., and Vemuri, B., "Shape modeling with front propagation: A level set approach," *IEEE Transactions on Pattern Analysis and Machine Intelligence*, vol. 17, no. 2, pp. 158–175, 1995.

[53] Maurice, R., Ohayon, J., Finet, G., and Cloutier, G., "Adapting the lagrangian speckle model estimator for endovascular elastography: Theory and validation with simulated radio-frequency data," *The Journal of the Acoustical Society of America*, vol. 116, no. 2, pp. 1276–1286, 2004.

[54] McInerney, T. and Terzopoulos, D., "Deformable models in medical image analysis: a survey," *Medical Image Analysis*, vol. 1, no. 2, pp. 91–108, 1996.

[55] Menet, S., Saint-Marc, P., and Medioni, G., "B-snakes: Implementation and application to stereo," in *Image Understanding Workshop*, pp. 720–726, 1990.

[56] Morton, C. and Lockwood, G., "Design of a 40 mhz annular array," in *Proceedings of the IEEE Ultrasonics Symposium*, pp. 1135–1138, 2001.

[57] Nave, R., *Hyperphysics*. Department of Physics and Astronomy, Georgia State University, http://hyperphysics.phy-astr.gsu.edu/hbase/hph.html, 24 October 2007.

[58] Oakeson, K., Zhu, H., and Friedman, M., "Quantification of cross-sectional artery wall motion with ivus image registration," in *Medical Imaging 2004: Ultrasonic Imaging and Signal Processing. Proceedings of the SPIE.*, pp. 119–130, 2004.

[59] O'Donnell, L., "Semi-automatic medical image segmentation," Master's thesis, Massachusetts Institute of Technology, 2001.

[60] O'Donnell, L., Westin, C., Grimson, W., Ruiz-Alzola, J., Shenton, M., and Kikinis, R., "Phase-based user-steered image segmentation," in *Fourth International Conference on Medical Image Computing and Computer-Assisted Intervention*, 2001.

[61] O'Donnell, M., Skovoroda, A., and Shapo, B., "Measurement of arterial wall motion using fourier based speckle tracking algorithms," in *Proceedings of the IEEE Ultrasonics Symposium*, pp. 1101–1104, 1991.

[62] Ophir, J., Cèspedes, E., Garra, B., Ponnekanti, H., Huang, Y., and Maklad, N., "Elastography: Ultrasonic imaging of tissue strain and elastic modulus in vivo," *European Journal of Ultrasound*, vol. 3, no. 1, pp. 49–70, 1996.

[63] Ophir, J., Cèspedes, E., Ponnekanti, H., Yazdi, Y., and Li, X., "Elastography: A quantitative method for imaging the elasticity of biological tissues," *Ultrasonic Imaging*, vol. 13, no. 2, pp. 111–134, 1991.

[64] Ophir, J., Kallel, F., Varghese, T., Bertrand, M., Cèspedes, E., and Ponnekanti, H., "Elastography: a systems approach," *International Journal of Imaging Systems and Technology*, vol. 8, no. 1, pp. 89–103, 1997.

[65] Osher, S. and Sethian, J., "Fronts propagation with curvature-dependent speed: Algorithms based on hamilton-jacobi formulations," *Journal of Computational Physics*, vol. 79, no. 1, pp. 12–49, 1988.

[66] Panametrics, Inc., *Ultrasonics Transducers*.

[67] Paragios, N. and Deriche, R., "A pde-based level-set approach for detection and tracking of moving objects," in *Proceedings of the Sixth International Conference on Computer Vision*, pp. 1139–1145, 1998.

[68] Paragios, N. and Deriche, R., "Geodesic active contours and level sets for the detection and tracking of moving objects," *IEEE Transactions on Pattern Analysis and Machine Intelligence*, vol. 22, no. 3, pp. 266–280, 2000.

[69] Pham, D., Xu, C., and Prince, J., "Current methods in medical image segmentation," *Annual Review of Biomedical Engineering*, vol. 2, pp. 315–337, 2000.

[70] Plissiti, M., Fotiadis, D., Michalis, L., and Bozios, G., "An automated method for lumen and media-adventitia border detection in a sequence of ivus frames," *IEEE Transactions on Information Technology in Biomedicine*, vol. 8, no. 2, pp. 131–141, 2004.

[71] Rashid, S., Salacinski, H., Hamilton, G., and Seifalian, A., "The use of animal models in developing the discipline of cardiovascular tissue engineering: a review," *Biomaterials*, vol. 25, no. 9, pp. 1627–1637, 2004.

[72] Revell, J., *Computer vision elastography*. PhD thesis, University of Bristol, 2004.

[73] Revell, J., Mirmehdi, M., and McNally, D., "Computer vision elastography: Speckle adaptive motion estimation for elastography using ultrasound sequences," *IEEE Transactions on Medical Imaging*, vol. 24, no. 6, pp. 755–766, 2005.

[74] Richardson, P., Davies, M., and Born, G., "Influence of plaque configuration and stress distribution on fissuring of coronary atherosclerotic plaques," *Lancet*, vol. 2, no. 8669, pp. 941–944, 1989.

[75] Righetti, R., Ophir, J., and Ktonas, P., "Axial resolution in elastography," *Ultrasound in Medicine and Biology*, vol. 28, no. 1, pp. 101–113, 2002.

[76] Ritter, T., Shrout, T., and Shung, K., "Development of high frequency medical ultrasound arrays," in *Proceedings of the IEEE Ultrasonics Symposium*, pp. 1127–1133, 2001.

[77] Ryan, L. and Foster, F., "Ultrasonic measurement of differential displacement and strain in a vascular model," *Ultrasonic Imaging*, vol. 19, no. 1, pp. 19–38, 1997.

[78] Scaggiante, A., Frezza, R., and Zampato, M., "Identifying and tracking ellipses: a technique based on elliptical deformable templates," in *Proceedings of the IEEE International Conference on Image Analysis and Processing*, pp. 582–587, 1999.

[79] Schaar, J., de Korte, C., Mastik, F., Strijder, C., Pasterkamp, G., Boersma, E., Serruys, P., and Van der Steen, A., "Characterizing vulnerable plaque features with intravascular elastography," *Circulation*, vol. 108, no. 21, pp. 2636–2641, 2003.

[80] Schulze-Clewing, J., Eberle, M., and Stephens, D., "Miniaturized circular array," in *Proceedings of the IEEE Ultrasonics Symposium*, pp. 1253–1254, 2000.

[81] Shadwick, R., "Mechanical design in arteries," *The Journal of Experimental Biology*, vol. 202, no. 23, pp. 3305–3313, 1999.

[82] Shah, J., "A common framework for curve evolution, segmentation and anisotropic diffusion," in *Proceedings of the IEEE Conference on Computer Vision and Pattern Recognition*, pp. 136–142, 1996.

[83] Shapo, B., Crowe, J., Skovoroda, A., Eberle, M., Cohn, N., and O'Donnell, M., "Displacement and strain imaging of coronary arteries with intraluminal ultrasound," *IEEE Transactions on Ultrasonics, Ferroelectrics, and Frequency control*, vol. 43, no. 2, pp. 234–246, 1996.

[84] Srinivasan, S., Kallel, F., Souchon, R., and Ophir, J., "Analysis of an adaptive strain estimation technique for elastography," *Ultrasonic Imaging*, vol. 24, no. 2, pp. 109–118, 2002.

[85] Szeliski, R. and Coughlin, J., "Spline-based image registration," *International Journal of Computer Vision*, vol. 22, no. 3, pp. 199–218, 1997.

[86] Talhami, H., Wilson, L., and Neale, M., "Spectral tissue strain: a new technique for imaging tissue strain using intravascular ultrasound," *Ultrasound in Medicine and Biology*, vol. 20, no. 8, pp. 759–772, 1994.

[87] Tikhonov, A. and Arsenin, V., *Solution of ill-posed problems*. New York: Wiley, 1977.

[88] Tsai, A., Yezzi, A., Wells, W., Tempany, C., Tucker, D., Fan, A., Grimson, W. E., and Willsky, A., "A shape-based approach to the segmentation of medical imagery using level sets," *IEEE Transactions on Medical Imaging*, vol. 22, no. 2, pp. 137–154, 2003.

[89] Varghese, T., Konofagou, E., Ophir, J., Alam, S., and Bilgen, M., "Direct strain estimation in elastography using spectral cross-correlation," *Ultrasound in Medicine and Biology*, vol. 26, no. 9, pp. 1525–1537, 2000.

[90] Varghese, T. and Ophir, J., "Characterization of elastographic noise using the envelope of echo signals," *Ultrasound in Medicine and Biology*, vol. 24, no. 4, pp. 543–555, 1998.

[91] Verdouw, P., Wolffenbuttel, B., and Van der Giessen, W., "Domestic pigs in the study of myocardial ischemia," *European Heart Journal*, vol. 4 (Suppl C), pp. 61–67, 1983.

[92] Veress, A., Weiss, J., Gullberg, G., Vince, D., and Rabbitt, R., "Strain measurement in coronary arteries using intravascular ultrasound and deformable images," *Journal of Biomechanical Engineering*, vol. 124, no. 6, pp. 734–741, 2002.

[93] Wan, M., Li, Y., Li, J., Cui, Y., and Zhou, X., "Strain imaging and elasticity reconstruction of arteries based on intravascular ultrasound video images," *IEEE Transactions on Biomedical Engineering*, vol. 48, no. 1, pp. 116–120, 2001.

[94] Williams, D. and Shah, M., "A fast algorithm for active contours and curvature estimation," *Computer Vision, Graphics, and Image Processing (CVGIP): Image Understanding*, vol. 55, no. 1, pp. 14–26, 1992.

[95] Williams, M., Stewart, R., Low, C., and Wilkins, G., "Assessment of the mechanical properties of coronary arteries using intravascular ultrasound: An in vivo study," *International Journal of Cardiac Imaging*, vol. 15, no. 4, pp. 287–294, 1999.

[96] Yezzi, A., Kichenassamy, S., Kumar, A., Olver, P., and Tannenbaum, A., "A geometric snake model for segmentation of medical imagery," *IEEE Transactions on Medical Imaging*, vol. 16, no. 2, pp. 199–209, 1997.

[97] Yezzi, A., Tsai, A., and Willsky, A., "A statistical approach to curve evolution for image segmentation," tech. rep., MIT LIDS Technical Report, 1999.

[98] Yuen, P., Wong, Y., and Tong, C., "Contour detection using enhanced snakes algorithm," *Electronics Letters*, vol. 32, no. 3, pp. 202–204, 1996.

[99] Zhu, H., Liang, Y., and Friedman, M., "Ivus image segmentation based on contrast," in *Medical Imaging 2002: Image Processing. Proceedings of the SPIE.*, pp. 1727–1733, 2002.

[100] Zhu, Y. and Yan, H., "Computerized tumor boundary detection using a hopfield neural network," *IEEE Transactions on Medical Imaging*, vol. 16, no. 1, pp. 55–67, 1997.